Universidad Carlos III de Madrid

Degree in Biomedical Engineering
2017-2018

Bachelor Thesis

“NEW REGULARIZATION TECHNIQUE FOR MRI SENSE RECONSTRUCTION IN STUDIES OF CORONARY ANGIOGRAPHY”

ANDRÉS MARTÍNEZ MORA

DIRECTOR: BORJA IBÁÑEZ CABEZA

TUTOR: MÓNICA ABELLA GARCÍA

LEGANÉS, 5TH JULY 2018

This work is licensed under Creative Commons **Attribution – Non Commercial – Non Derivatives**

NEW REGULARIZATION TECHNIQUE FOR MRI SENSE RECONSTRUCTION IN STUDIES OF CORONARY ANGIOGRAPHY

Centro Nacional de Investigaciones
Cardiovasculares (CNIC)

Departamento de Bioingeniería e Ingeniería
Aeroespacial

Universidad Carlos III de Madrid

Título: New Regularization Technique for MRI SENSE reconstruction in Studies of Coronary Angiography
Autor: Andrés Martínez Mora
Director: Borja Ibáñez Cabeza
Tutora Académica: Mónica Abella García

EL TRIBUNAL

Presidente: Luis Hernández Corporales
Vocal: Lorena Cussó Mula
Secretario: Claudia de Molina Gómez

Realizado el acto de defensa y lectura del Trabajo Fin de Grado el día 5 de julio de 2018, en la Escuela Politécnica Superior de la Universidad Carlos III de Madrid, acuerda otorgarle la CALIFICACIÓN de:

VOCAL

SECRETARIO PRESIDENTE

ABSTRACT

Coronary Magnetic Resonance Angiography (coronary MRA) is an imaging modality based on Magnetic Resonance Imaging that extracts information from the coronary vessels. Unlike X-ray angiography, it does not make use of ionizing radiation and it has the option of not making use of contrast agents, allowing for non-invasive studies free of contraindications from these contrast agents. However, the acquisition time for a coronary MRA is much longer than for an X-ray angiography. For that reason, many approaches have been proposed to reduce its acquisition time.

One of these approaches is Sensitivity Encoding or SENSE reconstruction, a method that reduces by a tunable factor the data to be acquired from the patient by making use of the sensitivity maps from several surface coils that receive all the information from the patient in parallel (at the same time). It is an effective method for reducing acquisition time, but it also introduces noise in the final image, especially as the reduction of data is stronger. For that purpose, algorithms known as regularization algorithms have been proposed to reduce this noise together with the introduction of prior information from the coil that excites the patient tissues, known as body coil.

Although the proposed regularization algorithms are quite good in denoising SENSE-reconstructed images, alternative prior information that has not been used until now may reduce even more the noise in the image. This thesis proposes a new algorithm based on regularized SENSE reconstruction that uses a low-pass filtered image pre-reconstructed with SENSE as alternative prior information. Until now, the only prior information that regularized SENSE reconstruction has received has been the one provided by the body coil, which is very crude and homogenous, so it is expected that if an image with an alternative and detailed prior information is introduced in SENSE reconstruction, noise may be reduced and image quality may increase.

The algorithm was implemented in IDL™ and tested with data from a volunteer. The results provided were compared to state-of-the-art methods that used either no prior information or only used body coil information as prior information. These methods were evaluated in terms of noise, Signal-to-Noise Ratio (SNR), Contrast-to-Noise Ratio (CNR) and with a visual inspection.

However, the compared results showed that even by introducing alternative prior information, the images could not be denoised more than the current method that uses body coil *a priori* information. Nevertheless, even if the algorithm failed to denoise SENSE reconstructed images more than the current methods did, this thesis can help to look for alternative paths for SENSE reconstruction denoising in the future.

Keywords: **Magnetic Resonance Imaging, SENSE reconstruction regularization, non- contrast coronary MRA**

ACKNOWLEDGEMENTS

First of all, I would like to say thanks to my thesis Director, Borja Ibáñez, for letting me do my thesis in his laboratory group in CNIC, full of highly prepared professional people and one of the best groups for Cardiovascular Research, not only from Spain, but from the whole world.

I am also very pleased to my academic tutor and professor from the University, Mónica Abella, who thanks to her experience she has given me many guidelines to perform this thesis in the best way as possible.

Apart from them, I have to especially mention the person that has been with me most of the time and that has devoted a lot of time and effort that he could have perfectly devoted to other things in helping me and that, unfortunately, for bureaucratic reasons could not be included as tutor of the thesis and it is a real pity that his name is not in the thesis cover: Javier Sánchez González. I will always be in doubt with you. I have been very lucky to do my thesis with you.

I have also to give thanks to all the people with whom I have shared different moments in CNIC and that have also helped me: Eduardo, Paula, Raquel, Daniel, Austin, Andrés, Carlos, Lilian, Chema…

I would like also to say thanks to all the professors at University, whom, without their work and support in their different subjects, it would have been impossible for me to develop this thesis: Mónica (again), Javier, Manolo, Claudia, Lorena, Jorge, Saúl, Pablo, Telmo, José Luis, Lucía, Sara… and many others more.

And I must not forget and thank all the contribution and support that friends and family have given to me. They have made the path until exposing my thesis less difficult and easier to cope with. From here, I say a thousand times thank you to my parents, my brother, Sofía, Penélope, Gabriel, Miguel, Raquel and the rest of my classmates from University.

Thank you. We all made it happen.

CONTENT INDEX

1. INTRODUCTION 1

  1.1 Magnetic Resonance Imaging (MRI) 1

    1.1.1 Fundamentals 1

    1.1.2 Resonance 2

    1.1.3 Relaxation 3

    1.1.4 Sequences 5

    1.1.5 Information localization 6

  1.2 MR coronary angiography (coronary MRA) 7

  1.3 MRI SENSE reconstruction 8

    1.3.1 Feed forward regularization 13

    1.3.2 Tikhonov regularization 15

    1.3.3 Feedback regularization 17

    1.3.4 Alternative regularization methods 19

2. MOTIVATION & OBJECTIVES 23

3. MATERIALS & METHODS 25

  3.1 Proposed algorithm 25

  3.2 Raw data acquisition 27

  3.3 Phantom simulation 27

  3.4 Algorithm implementation in IDL™ 29

  3.5 Phantom evaluation 37

  3.6 Algorithm evaluation 38

4. RESULTS 43

  4.1 Phantom simulation 43

  4.2 Graphs & tables for the evaluation of the algorithm with real data 46

    4.2.1 Blood in cut +7 47

    4.2.2 Myocardial muscle in cut -2 51

    4.2.3 Skeletal muscle (pectoralis) in cut +3 for noise and SNR and in cut +7 for CNR 57

  4.3 Visualization of real case images for the evaluation of the algorithm 63

5. DISCUSSION & FINAL CONCLUSIONS 71

  5.1 Phantom results 71

  5.2 Algorithm evaluation results 72

  5.3 Final conclusions 76
6. FUTURE WORK 79
7. SOCIOECONOMIC ANALYSIS 81
  7.1 Costs of the project 82
8. REGULATORY FRAMEWORK 87
9. GLOSSARY 90
10. REFERENCES 93

FIGURE INDEX

Fig 1. Alignment of non-zero spin set of nuclei under an intense external magnetic field.[7]..1

Fig 2. Precession movement experienced by a nucleus under an intense external magnetic field.[7]..1

Fig 3. Longitudinal magnetization change with time, after a 90º RF pulse.[16].................4

Fig 4. Transversal magnetization change with time, after a 90º RF pulse.[17]....................4

Fig 5. FID signal generated after a RF pulse has been shot to a certain nucleus.[19].........4

Fig 6. SE sequence[22] Pulse 2 is a 180º pulse..5

Fig 7. GRE sequence[23]..5

Fig 8. Slice selection through bandwidth selection of the RF pulse for nuclei with the same gyromagnetic ratio.[7]..7

Fig 9. Information localization through frequency encoding (horizontal direction) and phase encoding (vertical direction) in a 2D slice.[30]..7

Fig 10. Coronary MRA image obtained from a SSFP sequence.[37].................................8

Fig 11. Sensitivity maps for both coils.[42]..9

Fig 12. "Folded" images for two surface coils obtained with a SENSE factor of 2 just in the phase encoding direction[42]..9

Fig 13. Final reconstructed sample image with SENSE reconstruction.[42]......................12

Fig 14. Schematics of SENSE reconstruction.[42]...12

Fig 15. Scheme describing feed forward regularization applied to SENSE reconstruction...15

Fig 16. Scheme describing Tikhonov regularization applied to SENSE reconstruction...17

Fig 17. Scheme describing feedback regularization...19

Fig 18. Workflow to be followed during the work..26

Fig 19. Numerical phantom used in the SENSE reconstruction simulation.....................27

Fig 20. Scheme for the obtention of the coils' data...31

Fig 21. Scheme for the obtention of the protocol data..32

Fig 22. Scheme for the obtention of the raw data..33

Fig 23. Scheme for the obtention of the sensitivity maps..34

Fig 24. Schematics of the overall code designed in IDL™.......................................36, 37

Fig 25. ROI in blood in slice -7...39

Fig 26. ROI in myocardial muscle in slice +7...39

Fig 27. ROI in pectoral skeletal muscle in slice -7..39

Fig 28. Folded image obtained by IFT after reducing the samples to be acquired in the k-space. The size of the image is represented at scale with respect to those images in figures 29 and 30...43

Fig 29. Image used as Q-body coil for the simulation...43

Fig 30. Final unfolded and reconstructed image without regularization and without the help of the Q-body coil, with some level of Gaussian noise introduced.........................43

Fig 31. Final image reconstructed with λ=0 with feed forward regularization. In this case, no regularization was applied...44

Fig 32. Final image reconstructed with λ=10 with feed forward regularization............44

Fig 33. Final image reconstructed with λ=100 with feed forward regularization...........44

Fig 34. Highlight of folding artifacts in images regularized with feed forward regularization..44

Fig 35. Image reconstructed with Tikhonov regularization with λ=10^{-8}.........................45

Fig 36. Image reconstructed with Tikhonov regularization with λ=10^{-3}.........................45

Fig 37. Image reconstructed with Tikhonov regularization with λ=1.............................45

Fig 38. Highlight of folding artifacts in images regularized with Tikhonov regularization..45

Fig 39. Noise in blood for cut +7 and $\lambda_1=10^{-3}$..47

Fig 40. Noise in blood for cut +7 and $\lambda_1=10^{-2}$..47

Fig 41. Noise in blood for cut +7 and $\lambda_1=10^{-1}$..47

Fig 42. SNR in blood for cut +7 and $\lambda_1=10^{-3}$..49

Fig 43. SNR in blood for cut +7 and $\lambda_1=10^{-2}$..49

Fig 44. SNR in blood for cut +7 and $\lambda_1=10^{-1}$..49

Fig 45. Noise in myocardial muscle for cut -2 and $\lambda_1=10^{-3}$..51

Fig 46. Noise in myocardial muscle for cut -2 and $\lambda_1=10^{-2}$..51

Fig 47. Noise in myocardial muscle for cut -2 and $\lambda_1=10^{-1}$..51

Fig 48. SNR in myocardial muscle for cut -2 and $\lambda_1=10^{-3}$...53

Fig 49. SNR in myocardial muscle for cut -2 and $\lambda_1=10^{-2}$...53

Fig 50. SNR in myocardial muscle for cut -2 and $\lambda_1=10^{-1}$...53

Fig 51. CNR between blood and myocardial muscle for cut -2 and $\lambda_1=10^{-3}$..................55

Fig 52. CNR between blood and myocardial muscle for cut -2 and $\lambda_1=10^{-2}$..................55

Fig 53. CNR between blood and myocardial muscle for cut -2 and $\lambda_1=10^{-1}$..................55

Fig 54. Noise in skeletal muscle for cut +3 and $\lambda_1=10^{-3}$...57

Fig 55. Noise in skeletal muscle for cut +3 and $\lambda_1=10^{-2}$...57

Fig 56. Noise in skeletal muscle for cut +3 and $\lambda_1=10^{-1}$...57

Fig 57. SNR in skeletal muscle for cut +7 and $\lambda_1=10^{-3}$..59

Fig 58. SNR in skeletal muscle for cut +7 and $\lambda_1=10^{-2}$..59

Fig 59. SNR in skeletal muscle for cut +7 and $\lambda_1=10^{-1}$..59

Fig 60. CNR between blood and skeletal muscle for cut +7 and $\lambda_1=10^{-3}$......................61

Fig 61. CNR between blood and skeletal muscle for cut +7 and $\lambda_1=10^{-2}$.......................61

Fig 62. CNR between blood and skeletal muscle for cut +7 and $\lambda_1=10^{-1}$.......................61

Fig 63. Middle axial slice reconstructed without the help of the Q-body coil images for $\lambda_1=10^{-1}$...64

Fig 64. Middle axial slice reconstructed with the help of the Q-body coil images (first reconstruction) for $\lambda_1=10^{-1}$..64

Fig 65. Middle axial slice reconstructed with the help of the median filtered first reconstruction (second reconstruction) for $\lambda_1=10^{-1}$ and $\lambda_2=10^{-2}$.....................................64

Fig 66. Middle axial slice reconstructed with the help of the mean filtered first reconstruction (second reconstruction) for $\lambda_1=10^{-1}$ and $\lambda_2=10^{-2}$.....................................64

Fig 67. Middle coronal slice reconstructed without the help of the Q-body coil images for $\lambda_1=10^{-1}$...64

Fig 68. Middle coronal slice reconstructed with the help of the Q-body coil images (first reconstruction) for $\lambda_1=10^{-1}$..64

Fig 69. Middle coronal slice reconstructed with the help of the median filtered first reconstruction (second reconstruction) for $\lambda_1=10^{-1}$ and $\lambda_2=10^{-2}$......................................64

Fig 70. Middle coronal slice reconstructed with the help of the mean filtered first reconstruction (second reconstruction) for $\lambda_1=10^{-1}$ and $\lambda_2=10^{-2}$......................................64

Fig 71. Middle sagittal slice reconstructed without the help of the Q-body coil images for $\lambda_1=10^{-1}$..65

Fig 72. Middle sagittal slice reconstructed with the help of the Q-body coil images (first reconstruction) for $\lambda_1=10^{-1}$..65

Fig 73. Middle sagittal slice reconstructed with the help of the median filtered first reconstruction (second reconstruction) for $\lambda_1=10^{-1}$ and $\lambda_2=10^{-2}$.....................................65

Fig 74. Middle sagittal slice reconstructed with the help of the mean filtered first reconstruction (second reconstruction) for $\lambda_1=10^{-1}$ and $\lambda_2=10^{-2}$.....................................65

Fig 75. Middle axial slice of the Q-body coil images..67

Fig 76. Middle axial slice of the median filtered first reconstruction for $\lambda_1=10^{-1}$............67

Fig 77. Middle axial slice of the mean filtered first reconstruction for $\lambda_1=10^{-1}$................67

Fig 78. Middle coronal slice of the Q-body coil images..67

Fig 79. Middle coronal slice of the median filtered first reconstruction for $\lambda_1=10^{-1}$........67

Fig 80. Middle coronal slice of the mean filtered first reconstruction for $\lambda_1=10^{-1}$...........67

Fig 81. Middle sagittal slice of the Q-body coil images..68

Fig 82. Middle sagittal slice of the median filtered first reconstruction for $\lambda_1=10^{-1}$........68

Fig 83. Middle sagittal slice of the mean filtered first reconstruction for $\lambda_1=10^{-1}$...........68

TABLE INDEX

Table 1. Standard deviations for noise measurements in blood for cut +7 and $\lambda_1=10^{-3}$........47

Table 2. Standard deviations for noise measurements in blood for cut +7 and $\lambda_1=10^{-2}$........47

Table 3. Standard deviations for noise measurements in blood for cut +7 and $\lambda_1=10^{-1}$........47

Table 4. Standard deviations for SNR measurements in blood for cut +7 and $\lambda_1=10^{-3}$........49

Table 5. Standard deviations for SNR measurements in blood for cut +7 and $\lambda_1=10^{-2}$........49

Table 6. Standard deviations for SNR measurements in blood for cut +7 and $\lambda_1=10^{-1}$........49

Table 7. Standard deviations for noise measurements in myocardial muscle for cut -2 and $\lambda_1=10^{-3}$........51

Table 8. Standard deviations for noise measurements in myocardial muscle for cut -2 and $\lambda_1=10^{-2}$........51

Table 9. Standard deviations for noise measurements in myocardial muscle for cut -2 and $\lambda_1=10^{-1}$........51

Table 10. Standard deviations for SNR measurements in myocardial muscle for cut -2 and $\lambda_1=10^{-3}$........53

Table 11. Standard deviations for SNR measurements in myocardial muscle for cut -2 and $\lambda_1=10^{-2}$........53

Table 12. Standard deviations for SNR measurements in myocardial muscle for cut -2 and $\lambda_1=10^{-1}$........53

Table 13. Standard deviations for CNR measurements between blood and myocardial muscle for cut -2 and $\lambda_1=10^{-3}$........55

Table 14. Standard deviations for CNR measurements between blood and myocardial muscle for cut -2 and $\lambda_1=10^{-2}$........55

Table 15. Standard deviations for CNR measurements between blood and myocardial muscle for cut -2 and $\lambda_1=10^{-1}$........55

Table 16. Standard deviations for noise measurements in skeletal muscle for cut +3 and $\lambda_1=10^{-3}$....................57

Table 17. Standard deviations for noise measurements in skeletal muscle for cut +3 and $\lambda_1=10^{-2}$....................57

Table 18. Standard deviations for noise measurements in skeletal muscle for cut +3 and $\lambda_1=10^{-1}$....................57

Table 19. Standard deviations for noise measurements in skeletal muscle for cut +3 and $\lambda_1=10^{-3}$....................59

Table 20. Standard deviations for SNR measurements in skeletal muscle for cut +3 and $\lambda_1=10^{-2}$....................59

Table 21. Standard deviations for SNR measurements in skeletal muscle for cut +3 and $\lambda_1=10^{-1}$....................59

Table 22. Standard deviations for CNR measurements between blood and skeletal muscle for cut +7 and $\lambda_1=10^{-3}$....................61

Table 23. Standard deviations for CNR measurements between blood and skeletal muscle for cut +7 and $\lambda_1=10^{-2}$....................61

Table 24. Standard deviations for CNR measurements between blood and skeletal muscle for cut +7 and $\lambda_1=10^{-1}$....................61

Table 25. CTA vs MRA....................81

Table 26. Hours dedicated to the project....................83

Table 27. Table of perishable costs....................83

Table 28. Table of inventorial costs....................84

Table 29. Table of total material costs....................84

Table 30. Service costs dedicated to the project....................84

Table 31. Personnel costs dedicated to the project....................85

Table 32. Direct costs dedicated to the project....................85

Table 33. Total costs dedicated to the project (without taxes)....................85

1. INTRODUCTION

1.1 Magnetic Resonance Imaging (MRI)

Magnetic Resonance Imaging or MRI is one of the most widespread medical imaging modalities, being developed from NMR spectroscopy [1] in the 1970s, thanks to the contribution of authors as Lauterbur or Mansfield [2] . Among the advantages over other imaging techniques it can be found that it offers a really good spatial resolution for many tissues (many anatomical details can be easily distinguished), it has no penetration limits and it does not make use of ionizing radiation. However, it is an expensive modality and its acquisition time can be sometimes too long, although the most recent advances have dramatically speeded up image acquisition. [3]

1.1.1 Fundamentals

The fundamentals of MRI are complex and it is not the objective of the thesis to enter into too much detail.

Some protons and neutrons inside the nuclei, known as nucleons when referred to them indistinctively, have a non-zero spin [4] as happens in H-1, C-13 or O-15, being H-1 the most abundant nucleus with non-zero spin in the body. This spin has a *magnetic moment* (μ) [4] that enables non-zero spin nuclei interact with external static magnetic fields (B_o), in such a way that a certain torque is generated perpendicularly to the external magnetic field direction, so that by the gyroscopic effect [5] , the nuclei instead of moving in the parallel direction imposed by the magnetic field, move towards the perpendicular direction imposed by the torque and as this torque is the same for all the points in space, these nuclei start to precess in the direction of the external static magnetic field [2] . This happens with very strong magnetic fields, of around 1.5 T in clinical cases and even more intense fields in preclinical research, generating them with superconducting magnets refrigerated with liquid helium below 4K.

All these precession effects cannot be quantified with just a nucleus, but with a set of nuclei with the same magnetic behavior or *isochromat*. [6], [7]

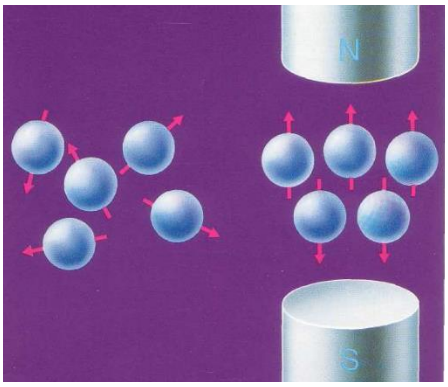

Fig 1. Alignment of non-zero spin set of nuclei under an intense external magnetic field [7]

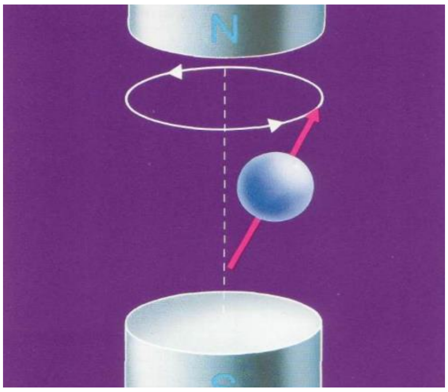

Fig 2. Precession movement experienced by a non-zero spin set of nuclei under an intense external magnetic field,. [7]

The isochromats precess always at the same frequency under the same field intensity, as they have a constant and specific *gyromagnetic ratio* (γ) [2], [8] per chemical species, with typical values of dozens of MHz/T. Then, the frequency of precession around the external magnetic field or *Larmor frequency* can be calculated with the equation below, being known as *Larmor equation*: [9]

$$\omega = \gamma B_o \qquad (1.1.1.1)$$

Nuclear spins can precess parallely (*spin up*) or antiparallely (*spin down*) around the external magnetic field. The parallel state will be less energetic than the antiparallel one, so the isochromats will tend to precess parallely, although this sense of precession can change if energy is absorbed. This effect is known as *Zeeman splitting* [10] . The energies for the antiparallel and parallel states and the energy gap between them for this Zeeman splitting are:

$$\left.\begin{array}{ll} E_{antiparallel} = -\frac{1}{2}\gamma h B_o & (1.1.1.2) \\ E_{parallel} = +\frac{1}{2}\gamma h B_o & (1.1.1.3) \end{array}\right\} \quad \Delta E = E_{parallel} - E_{antiparallel} = \gamma h B_o \qquad (1.1.1.4)$$

Where h is the Planck's constant.

The total sum of the effect of all the spins of an isochromat in an intense magnetic field yields a small magnetic field known as *magnetization vector* [11] , which, if the system is undisturbed, will be in the same direction as the external magnetic field and will be constant. The magnetization vector is made of two components: the *longitudinal magnetization*, which is the parallel component to the external magnetic field, and the *transversal magnetization*, which is perpendicular to the external magnetic field and will be the one that when varies in time provides a measurable electric signal by the Faraday-Lenz's law [12]. If no more magnetic fields interact with the system, all the magnetization is longitudinal and no electric signal will be measured, as there is no transversal magnetization.

1.1.2 Resonance

The magnetization vector needs to be somehow disturbed to provide a transversal magnetization that changes in time and generates a measurable electric signal. If equations 1.1.1.1 and 1.1.1.4 are combined, the energy gap between the parallel and antiparallel states can be filled with a magnetic field of energy **E=h·** $\boldsymbol{\omega}$ being ω the Larmor frequency of the system. Therefore, if a magnetic field that oscillates with the same frequency as the Larmor frequency is applied to the body of the patient, the spins will gain the enough energy so to change from the parallel to the antiparallel state, in such a way that the magnetization vector changes a certain angle known as Flip Angle (FA) and yields a transversal magnetization variable in time that produces an electric measurable signal. The maximum signal will be obtained when the transversal magnetization is maximum, using normally in MRI RF pulses with FAs of 90º (known as 90º pulses).

Taking into account the typical values of the gyromagnetic constant for H-1, C-13... and the modulus of the external magnetic field used in equation 1.1.1.1, Larmor frequencies take values in the range of dozens of MHz. Consequently, the oscillating magnetic field needs to be a RadioFrequency (RF) pulse, as it is needed to oscillate at the same frequency as the Larmor frequencies, and ElectroMagnetic (EM) radiations of frequencies of dozens of MHz belong to the RF spectrum. This excitation effect caused by these RF pulses is known as *resonance* [2] .

Therefore, for reaching a resonance state, an RF pulse should be emitted by a coil known as *body coil*, which can also be used for obtaining information from the patient before the MR scan takes place, producing crude and homogenous information known as *prior* or *a priori information*. This prior information can be used to remove noise in some reconstruction algorithms, which will be explained later. If the body coil is made of more than one element for measuring frequency and phase, the body coil is called *quadrature body coil*, *quad-body coil* or *Q-body coil*. [13]

Furthermore, RF coils are needed for receiving the electric signals from the patient as well, using certain coils close to the surface of the patient known as *surface coils* or *receiver coils*. These coils have a changing sensitivity in space, which can be represented in *sensitivity maps*. These maps are used in some reconstruction algorithms that will be described later.

1.1.3 Relaxation

After some time, the RF pulse is disconnected, and the system will go back to the initial situation in point 1.1.1, carrying out a process known as *relaxation* [2] , where the longitudinal magnetization will increase again by releasing energy to the surrounding or *lattice* in a process known as *spin-lattice relaxation* [14] , and the transversal magnetization will decrease due to spin dephasing because of magnet and local inhomogeneities (factors turning the external magnetic field not constant in space), in a phenomenon known as *spin-spin relaxation* [14] . The differential equations governing both relaxation types are called *Bloch equations* [15] . The results of those equations are shown below:

$$M_{longitudinal}(t) = M_{longitudinal_o} \cdot \left(1 - e^{-\frac{t}{T_1}}\right) \qquad (1.1.3.1)$$

$$M_{transversal}(t) = M_{transversal_o} \cdot e^{-\frac{t}{T_2}} \qquad (1.1.3.2)$$

Where T_1 [2] is the 63% of the total time spent for recovering the initial longitudinal magnetization, being short in tissues that absorb energy easily, like fat, and long in tissues that do not absorb energy so easily, as are moving tissues like blood and solid tissues like bone. Then, T_2 [2] is the 37% of the time spent in losing the transversal magnetization, being short in non-uniform tissues with many local inhomogeneities like fat or bone and being long in uniform tissues with not so many local inhomogeneities like blood. The curves for a *spin-lattice* and a *spin-spin* relaxation process with a FA of 90º are depicted below [16], [17]:

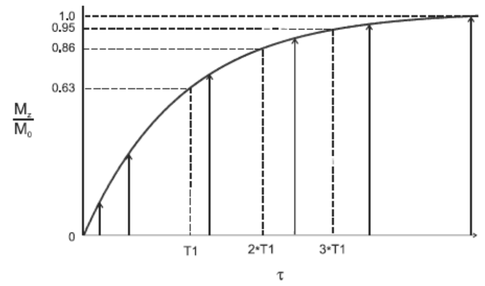

Fig 3. Longitudinal magnetization change with time, after a 90º RF pulse .[16]

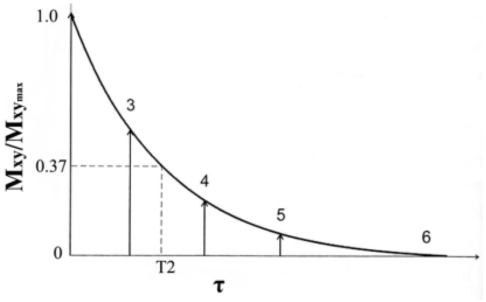

Fig 4. Transversal magnetization change with time, after a 90º RF pulse .[17]

As during relaxation, magnetization is changing with time, the signal that will be provided from this process is called Free Induction Decay signal or FID [18] and will have the shape of a sinusoid with an exponential decrease, since the transversal magnetization decays exponentially while oscillating. Its shape is depicted below [19]:

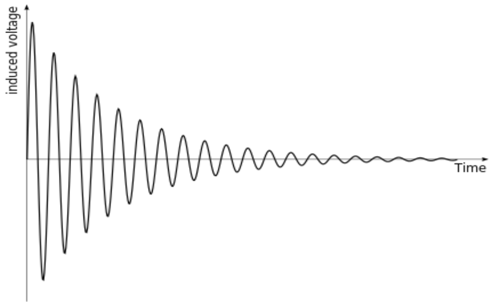

Fig 5. FID signal generated after a RF pulse has been shot to a certain nucleus .[19]

The FID signal should decay to 37% of its value after a time T_2 (see equation 1.1.3.2), but in reality it decays much faster due to field inhomogeneities, with a shorter time than T_2 known as T_2* (T_2 star) [20] . To reduce field inhomogeneities and bring T_2 and T_2* closer, special coils called *shimming coils* have to be used. The relationship between T_2 and T_2* is shown below: [20]

$$\frac{1}{T_2^*} = \frac{1}{T_2} + \frac{1}{T_2(inhomogeneities)} \qquad (1.1.3.3)$$

1.1.4 Sequences

Using different kinds of RF pulses together with field gradients (which are explained two paragraphs later), you can obtain different sequences that provide different contrast levels [21] . There exist two main types of sequences: Spin Echo or SE sequences [22] , which after shooting a 90º pulse that provides a FID, shoot a 180º pulse to recover part of the signal yielding a new signal called *echo* or *spin echo*. The time that has passed between shooting the 90º pulse and obtaining the echo is known as Time-to-Echo or TE, while the time between repetitions of this sequence is known as Time-to-Repeat or TR [2] . The combinations of different TRs and TEs provide different contrasts.

The other main type of sequences is Gradient Echo or GRE sequences [23] , which are a faster alternative to SE sequences, using gradient fields (again, see the paragraph below) that induce strong inhomogeneities to spoil the initial FID produced and using then the same gradient fields with the same strength but opposite direction to realign spins and yield an echo, typically a much weaker echo than the one from SE sequences. As many inhomogeneities have been induced very good shimming coils are needed. To reduce even more the acquisition time, RF pulses with FAs lower than 90º are used. To sum up, GRE sequences are faster but weaker, noisier and more prone to generate artifacts.

Gradient fields [24] are low intensity magnetic fields caused by resistive magnets known as *gradient coils* able to change linearly the outer static field in a certain direction. By equation 1.1.1.1, also the Larmor frequencies are changed linearly [9] . In GRE sequences, these fields are able to induce more field inhomogeneities and spoil the FID to acquire echoes faster, while in the process of image formation they are able to make the scanner differentiate among slices precessing at different frequencies. [22]–[24]

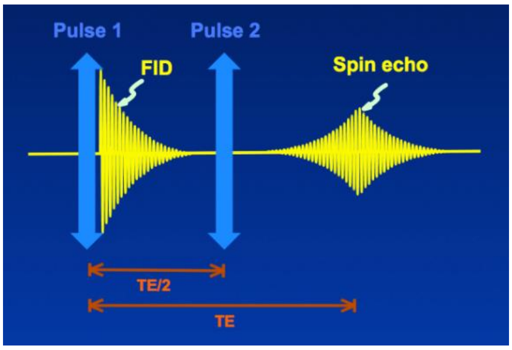

Fig 6. SE sequence[22]*Pulse 2 is a 180º pulse*

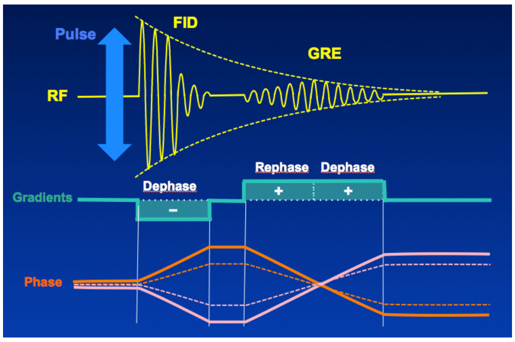

Fig 7. GRE sequence[23]

The exact sequence applied in this thesis was Steady State Free Precession (SSFP) [25] , a sequence for Magnetic Resonance Angiography (MRA) [26] able to provide a very large signal from blood while obtaining a minimum signal from the surroundings, obtaining a very good contrast between tissues without the need of contrast media. The mechanisms with which MRA works will be explained in point 1.2. Furthermore, to obtain a further increase of contrast, the fat signal in SSFP can be suppressed [27] with inversion pulses [28] , so that no fat is acquired in the area of interest, although as the tissue is further from that area.

1.1.5 Information localization

MR images are normally 3D, being made up of slices, and each slice is sampled into rows and columns.

In order to be able to collect information from different slices, the scanner has to recognize the location of these slices. For doing so, the external magnetic field and the Larmor frequencies can be modified linearly with a gradient field called *Slice Selection Gradient* along the direction through which the slices have to be obtained, so that when a certain RF pulse is emitted, only those points of space with the frequencies included in the bandwidth of the pulse will be excited and produce signal. Depending on the bandwidth of the radio pulse and on the slope of the gradient field that is generated, the slice thickness will change. Wide bandwidths and a smooth gradients yield thick slices while narrow bandwidths and steep gradients will yield thin slices. [2], [29]

The MR scanner has also to identify nuclei in different positions of the same slice (rows and columns). For that purpose, another gradient perpendicular to the Slice Selection Gradient is applied to make the external field and the Larmor frequencies vary linearly, saving in the columns of the final image the information coming from isochromats precessing at the same frequency, so that isochromats from the same column precess at the same frequency but isochromats from different columns precess at different frequencies. This gradient is called *frequency encoding (FE) gradient* and only needs one echo from the sample to fill all the columns of the slice, with a certain sampling rate. [29]

To sort the nuclei into different rows of the same slice, a gradient keeping the phase of the isochromats when they are dephasing during relaxation is applied, making that isochromats saved in the same row precess in phase while isochromats from different rows precess with different phase. This gradient is known as *phase encoding (PE) gradient*, but unlike FE gradients, it can only fill one row of information with an echo, so the sequence has to be repeated as many times as rows are desired to be obtained from the slice. If an acquisition needs to fill hundreds of rows, it has to be repeated hundreds of times, lengthening MR acquisition time.

Finally, each slice of the patient is acquired as a matrix of frequencies and phases which is no more than the 2D Fourier Transform (FT) of the spatial information of each slice, being also known as *k-space* in MRI jargon. Consequently, the Inverse Fourier Transform (IFT) has to be calculated for the raw image obtained by the scanner to get the spatial information, in a process known as *reconstruction*. Reconstruction algorithms will be presented in more detail in section 1.3. [7], [30]

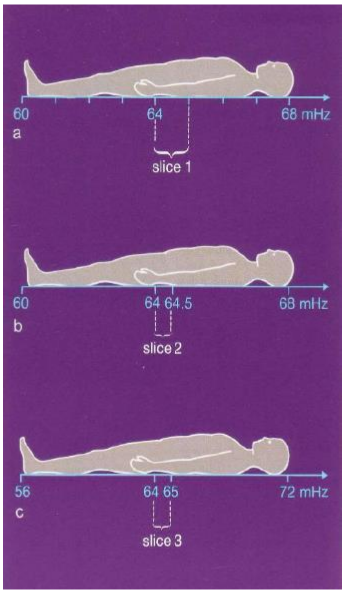

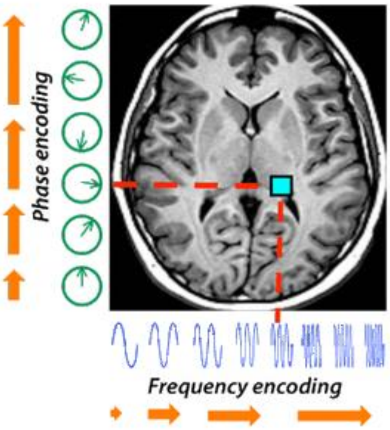

Fig 9. Information localization through frequency encoding (horizontal direction) and phase encoding (vertical direction) in a 2D slice. [30]

Fig 8. Slice selection through bandwidth selection of the RF pulse for nuclei with the Larmor frequencies included in the RF bandwidth .[7]

1.2 MR coronary angiography (coronary MRA) [26]

MRA is a modality where the clinicians want to obtain a high contrast of blood with respect to surrounding tissues, in order to detect any abnormality in blood. It offers a high contrast-to-noise ratio (from now on, CNR) between the vessels and surrounding tissues [31] . It makes use either of general sequences that use contrast agents to enhance differences between tissues [32] or of specific sequences that are able to extract very different signals between the blood and the surroundings without the need of a contrast medium. MRA modalities can be divided into techniques darkening blood and techniques brightening blood.

Darkening blood techniques (i.e. Fast Spin Echo (FSE) [33] or susceptibility-weighted (SW) [34] black blood MRA) suppress blood signal and enhance surrounding tissues signal, while brightening blood techniques do the opposite; they attenuate signals from the surrounding tissues while enhance signals emitted by blood (i.e. Time-of-Flight (TOF) [35] MRA, phase-contrast MRA [36] or steady-state free precession MRA (SSFP MRA) [25]).

In the thesis, coronary MRA will be applied without any contrast and with a bright-blood sequence, SSFP, that also suppresses fat signal [27] to increase contrast as most as possible, as explained at the end of point 1.1.4. [37]

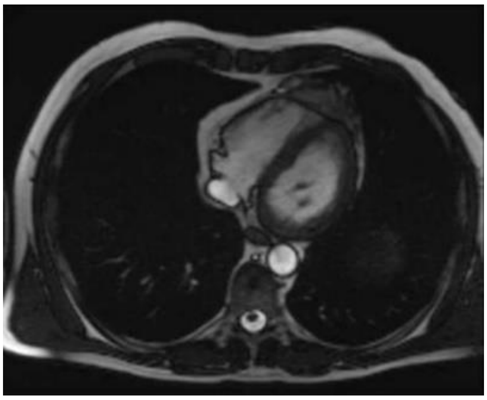

Fig 10. Coronary MRA image obtained from a SSFP sequence [37]

1.3 MRI SENSE reconstruction [38]

As explained in 1.1.5, once the frequencies corresponding to nuclei from different points in space are obtained and arranged into slices and these slices are arranged into rows and columns in the k-space [29], it is time to obtain the final image in the spatial domain, by performing a method called *reconstruction*. Due to the long acquisition time present in MRI, different reconstruction algorithms have been designed to reduce the information to acquire and decrease acquisition time, trying to produce similar results to the gold standard reconstruction that would be done by performing the IFT of all the k-space data.

The method that is going to be applied in the thesis for MR reconstruction is called Sensitivity Encoding reconstruction, also known as SENSE [38] reconstruction. It is a parallel imaging method, in the sense that it makes use of several surface coils at the same time to obtain the final reconstructed image while reducing acquisition time [39].

SENSE reconstruction reduces the samples to read in the k-space both in the frequency encoding direction and in the phase encoding direction (which are the rows and columns of the k-space). The samples are reduced by factor of reduction called SENSE factor (**SENSE factor= Total samples/ Actually read samples**). This reduction of samples will produce aliasing [40] when going to the image domain with the IFT and it will reduce the Field Of View (FOV) of the image (the total space seen in the image is smaller, precisely as small as the product of the SENSE factors used). This aliasing is present as folds of the different tissues of the image, so SENSE reconstruction will need an unfolding process where the tissues are unfolded and the whole FOV is recovered.

The steps carried out in the unfolding process by SENSE are the next ones:

1) Obtention of the sensitivity maps of the surface coils: the *sensitivity maps* are spatial representations of the sensitivities of each surface or receiver coil (see end of point 1.1.2) , since each coil is not uniform in space. These maps are calculated by normalizing the information from each receiver coil with the information from the Q-body coil (the Q-body coil was presented in point 1.1.2).

$$Sensitivity\ map\ for\ surface\ coil\ i = \frac{Information\ from\ surface\ coil\ i}{Q - body\ coil\ information} \quad (1.3.1)$$

During the unfolding process, SENSE reconstruction can optionally make use of prior information acquired before the MR scan to reduce noise [41] by multiplying the sensitivity maps to it. This prior information can come from the acquired image by the Q-body coil (see end of point 1.1.2), being the conventional level of prior information used right now by algorithms working with SENSE reconstruction. It is introduced in the reconstruction in the following way:

$$Sensitivity\ map_{Prior} = Sensitivity\ map \cdot Prior\ information \quad (1.3.2)$$

2) Obtention of the folded images: after decreasing the number of samples to acquire in the k-space, the folded images in the spatial domain are obtained by computing the IFT of this reduced k-space. There will be as many folded images as receiver coils used in the reconstruction. [42]

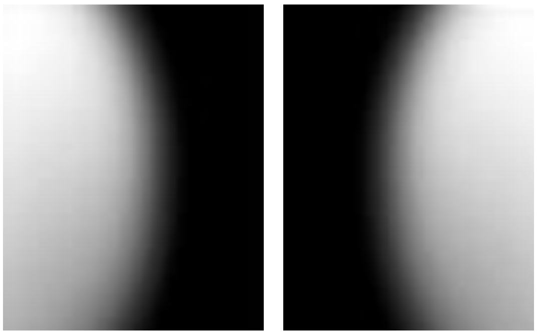

Fig 11. Sensitivity maps for two surface coils .[42]

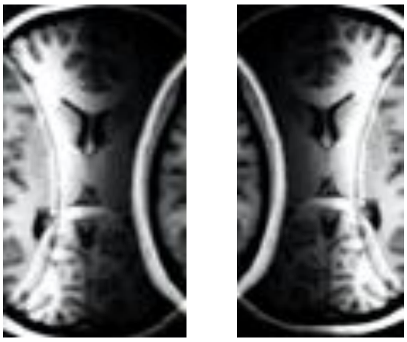

Fig 12. "Folded" images from two surface coils obtained with a SENSE factor of 2 just in the phase encoding direction, in such a way that the FOV is reduced to a half. .[42]

To guarantee that the unfolding process has a certain solution, the number of surface coils supplying each one with a sensitivity map has to be higher than the number of voxels to unfold. In other words, there must be more coils than the product of the SENSE factors used to remove k-space samples from the FE and PE directions. Consequently, the time reduction that can be obtained from SENSE will be superiorly bounded by the number of surface coils used in the unfolding process.

3) Establishment of the equation relating the folded voxels with the unfolded voxels: with the sensitivity information from each coil, SENSE establishes a linear relationship between the folded and the unfolded voxels, so that each coordinate of the folded images

will generate as many unfolded coordinates as the product of the SENSE factors used in the reconstruction. The following system of linear equations can be derived from this relationship:

$$\left.\begin{aligned}
z_{coil\ 1} &= a_1 \cdot S_{coil\ 1,1} + a_2 \cdot S_{coil\ 1,2} + \cdots + a_n \cdot S_{coil\ 1,n} \\
z_{coil\ 2} &= a_1 \cdot S_{coil\ 2,1} + a_2 \cdot S_{coil\ 2,2} + \cdots + a_n \cdot S_{coil\ 2,n} \\
&\vdots \\
z_{coil\ m} &= a_1 \cdot S_{coil\ m,1} + a_2 \cdot S_{coil\ m,2} + \cdots + a_n \cdot S_{coil\ m,n}
\end{aligned}\right\} \qquad (1.3.3)$$

n: number of voxels that have to be unfolded which equals the product of the SENSE factors

m: number of receiver coils used in the parallel acquisition

z_m: folded voxel value in the folded image coming from the m-th coil

$S_{m,n}$: sensitivity of the m-th coil for the n-th voxel to unfold

a_n: voxel value of the unfolded n-th coordinate

The system is expressed in matrix form as:

$$z = S \cdot a \qquad (1.3.4)$$

z: vector with the voxels in the folded images for the different receiver coils. Its length equals the number of coils. All the voxels are in the same coordinate for the different images.

$$z = (z_{coil\ 1}\ \ z_{coil\ 2}\ \ \ldots\ \ z_{coil\ m}) \quad (1.3.5)$$

S: sensitivity matrix. Contains the sensitivity values for all the coils in the coordinates where the unfolded voxels are computed, so its dimension is of m x n (“m” coils x “n” voxels to unfold). Sensitivities are no more than weighting factors for the unfolded voxels to obtain the folded voxels.

$$S = \begin{pmatrix} S_{coil\ 1,coordinate\ 1} & \cdots & S_{coil\ 1,coordinate\ n} \\ \vdots & \ddots & \vdots \\ S_{coil\ m,coordinate\ 1} & \cdots & S_{coil\ m,coordinate\ n} \end{pmatrix} \qquad (1.3.6)$$

a: vector with the unfolded voxels in the different coordinates to unfold. Its length equals the number of coordinates to unfold and the product of the SENSE factors in the FE and PE directions.

$$a = (a_{coordinate\ 1}\ \ a_{coordinate\ 2}\ \ \cdots\ \ a_{coordinate\ m}) \quad (1.3.7)$$

4) Inversion of the equation: equation 1.3.4 proposes the obtention of the folded voxels as a function of the unfolded ones, but what SENSE needs to perform is the opposite. Consequently, the pseudoinverse of the sensitivity matrix has to be computed by multiplying both sides of equation 1.3.4 by the conjugate transpose of the sensitivity matrix, also known as its Hermitian (S^H):

$$S^H \cdot z = S^H \cdot S \cdot a \ \rightarrow \ a = (S^H \cdot S)^{-1} \cdot S^H \cdot z \qquad (1.3.8)$$

Expression 1.3.8 can be simplified as:

$$U = (S^H \cdot S)^{-1} \cdot S^H \quad (1.3.9)$$

Where U is known as *unfolding matrix*, being the matrix that allows to unfold the image computing from the folded voxels in the different coils, the unfolded voxels. The combination of equations 1.3.8 and 1.3.9 yields:

$$a = U \cdot z \quad (1.3.10)$$

5) Repetition of steps 3 and 4: steps 3 and 4 are repeated until all the coordinates for the unfolded image have been calculated. The number of repetitions is:

$$\#\, Repetitions = \frac{Total\ voxels\ to\ unfold}{SENSE\ factor\ in\ PE \cdot\ SENSE\ factor\ in\ FE} \qquad (1.3.11)$$

Taking figures 11 and 12 as intermediate steps for SENSE reconstruction, the final unfolded image looks as:

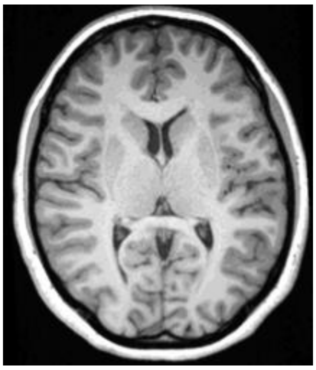

Fig 13. Final reconstructed image[42]

If it is desired to reduce the noise of the final unfolded image, this image can optionally be multiplied by an image with *a priori* information acquired before the actual MR scan takes place. This prior information can be the image generated by the Q-body coil, for instance, being the conventional level of prior information used right now in SENSE reconstruction.

$$Unfolded\ image_{prior} = Unfolded\ image \cdot Prior\ information \qquad (1.3.12)$$

A schematic representation of SENSE would be the following: [39]

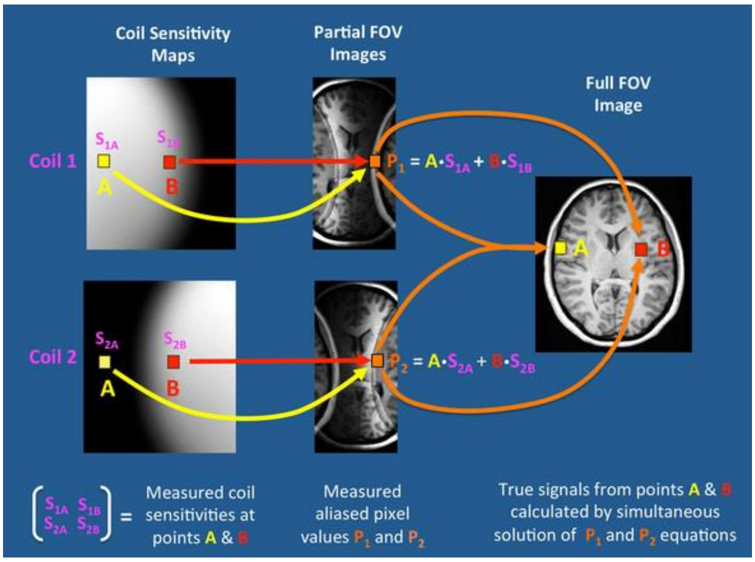
Coil Sensitivity Maps
Partial FOV Images
Full FOV Image
Coil 1
S_{1A}
S_{1B}
A
B
$P_1 = A \cdot S_{1A} + B \cdot S_{1B}$
Coil 2
S_{2A}
S_{2B}
A
B
$P_2 = A \cdot S_{2A} + B \cdot S_{2B}$
A
B
$\begin{pmatrix} S_{1A} & S_{1B} \\ S_{2A} & S_{2B} \end{pmatrix}$ = Measured coil sensitivities at points A & B
Measured aliased pixel values P_1 and P_2
True signals from points A & B calculated by simultaneous solution of P_1 and P_2 equations

Fig 14. Schematics of SENSE reconstruction.[42]

SENSE is an effective method for unfolding images affected by aliasing, but in the meanwhile introduces a lot of noise, decreasing the Signal-to-Noise Ratio (from now on, SNR [43]) of the unfolded image in comparison with an image reconstructed with all the samples from the k-space. The SNR will be reduced as the product of the SENSE factors is higher and more samples are removed and as the geometries of the coils are more complex, being represented by a *geometry factor* (g), which increases as these geometries are more complex, being ideally equal to 1:

$$SNR_{SENSE} = \frac{SNR_{full\ k-space}}{g \cdot \sqrt{\prod(SENSE\ factors\ in\ PE\ and\ FE\ directions)}} \qquad (1.3.13)$$

To reduce this noise caused by data inconsistencies in the surface coils, different methods known as *regularization methods* have been designed. These regularization methods depend on regularization factors to denoise SENSE-reconstructed images. Too low regularization factors hardly reduce any noise in comparison with a standard SENSE reconstruction while too high regularization factors are very effective in denoising but as they deviate more and more from the standard imposed by SENSE reconstruction, they are not so effective unfolding the images and some folding artifacts can appear in the images. Consequently, intermediate regularization factors have to be selected to balance the trade-off between noise and folding artifacts. In the thesis, the following ones were implemented.

1.3.1 Feed forward regularization [44]

Feed forward regularization slightly alters SENSE reconstruction by using the *a priori* information provided by the Q-body coil images before data acquisition, being for that reason classified as a forward method. In this method, equation 1.3.9 is modified by introducing a regularization matrix R:

$$U = (S^H \cdot S + R^{-1})^{-1} \cdot S^H \qquad (1.3.1.1)$$

R has to be a square matrix of dimension the number of voxels to unfold, containing values proportional to the square of the voxel values of the Q-body coil image in the coordinates of the final voxels that need to be unfolded.

$$R = \lambda \cdot diag(Q - body\ coil\ image\ values)^2 \qquad (1.3.1.2)$$

λ will be the regularization factor of this method, relating the values in the main diagonal of R with the square of the Q-body coil image values in the coordinates of the voxels to unfold. Too high λs yield folding artifacts in the image while too low λs keep the noise level introduced by SENSE reconstruction. As the Q-body coil images provide spatial information about the patient location, voxels falling out of the patient are zero, so no regularization is applied in the voxels falling out of the patient, while proportional regularization is applied as the voxel values in the Q-body coil image are higher.

To increase even more the denoising process induced by feed forward regularization, Singular Value Decomposition (from now on, SVD) [45] can be applied, factorizing the matrix to be inverted in order to know which voxels to unfold are more important in the reconstruction and which voxels to unfold are more irrelevant and maybe just introduce noise in the image. The contribution from this last type of voxels can be removed with almost no consequences for the final reconstructed image. The way in which SVD is applied is the following one:

$$S^H \cdot S + R^{-1} = X \cdot W \cdot Y^H \qquad (1.3.1.3)$$

Where X and Y are square matrices of dimension the number of voxels to unfold and W is a square diagonal matrix which tells how much each voxel to be unfolded contributes to the final reconstruction, containing values in decreasing order in the diagonal ($W_{1,1}$ is the highest and $W_{n,n}$ is the lowest). These values are known as Singular Values (from now on, SVs). Too low SVs indicate that the voxels to unfold hardly contribute to the unfolding process and maybe just introduce noise, so the SVs can be truncated to zero without almost any consequence in the unfolding, reducing noise. This process is known as *truncated SVD* [46] , which needs a truncation factor to decide which SVs are preserved and which are set to zero.

$$\begin{cases} W_{i,i} \geq Truncating\ value \rightarrow W_{i,i} \neq 0 \\ W_{i,i} < Truncating\ value \rightarrow W_{i,i} = 0 \end{cases} \qquad (1.3.1.4)$$

In the end, U will be calculated applying SVD as: [45]

$$U = (X \cdot W \cdot Y^H)^{-1} \cdot S^H = Y \cdot W' \cdot X^H \cdot S^H \qquad (1.3.1.5)$$

$$Where: \quad W' = diag(\frac{1}{W_{i,i}})$$

The inverse of a matrix decomposed by SVD will revert the multiplication order, leaving the matrix that left multiplied the non-inverted matrix with the SVs as a Hermitian matrix (X^H) that now right multiplies (as matrices have complex values, the SVD is not applied with the transpose matrices but with the Hermitian ones), turning the matrix that right multiplied into its non-Hermitian version (Y) and that now left multiplies. The new SVs are recalculated as the original SVs from matrix W in equation 1.3.1.3. These new SVs are introduced in the diagonal of a matrix called W’.

A simple scheme of the regularization method is included below:

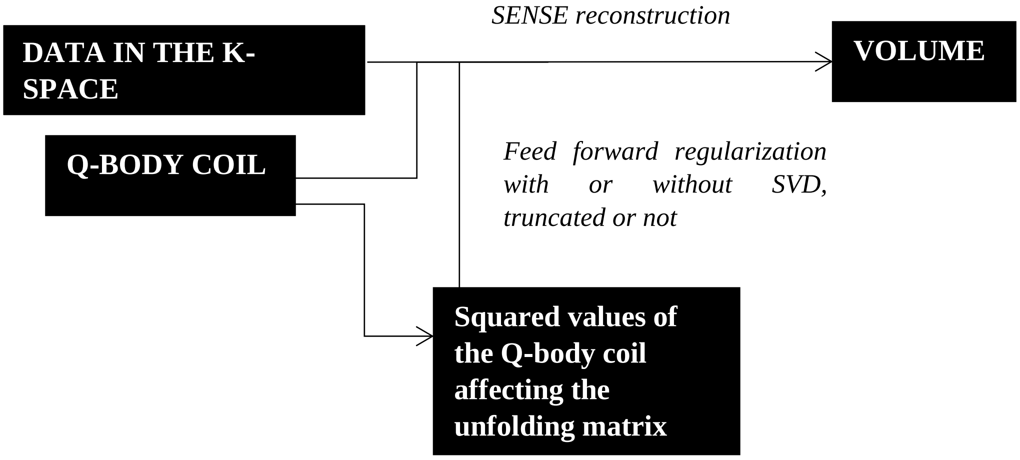
SENSE reconstruction
DATA IN THE K-SPACE
VOLUME
Q-BODY COIL
Feed forward regularization with or without SVD, truncated or not
Squared values of the Q-body coil affecting the unfolding matrix

Fig 15. Simple scheme describing feed forward regularization applied to SENSE reconstruction

1.3.2 Tikhonov regularization [47]–[49]

Other regularization approach that can be applied in SENSE reconstruction denoising is Tikhonov regularization. Tikhonov depends on a certain tunable factor introduced in the regularization that will behave as a regularization factor to reduce data inconsistencies introduced by high products of SENSE factors or intricate coil geometries. Again, SENSE reconstruction will be slightly modified when computing the unfolding matrix in equation 1.3.9. The way in which it is calculated is depicted below:

$$U = (S^H \cdot S + \lambda \cdot I)^{-1} \cdot S^H \qquad (1.3.2.1)$$

The regularization factor is λ, which is totally different from the λ in feed forward regularization, and if it is too high, it will induce folding artifacts in the image, as the reconstruction would be incomplete due to a too intense deviation; while if it is too low, it will hardly reduce any noise in comparison with the original reconstruction algorithm. “I” is the identity matrix, of dimension the number of voxels to be unfolded.

The regularization factor will be the same for all the voxels to unfold, being proportional to λ, which is another difference with feed forward regularization [44], where each voxel to unfold is regularized according to the square of the Q-body coil image values. In theory, equation 1.3.2.1 would have to work with a regularization image obtained from low frequency values of the k-space as Tikhonov regularization normally does, but for simplicity it is just set to zero.

In this method, truncated SVD [46] will also be applied to remove those voxels that hardly contribute to the unfolding process and introduce noise, but instead of factorizing the term that has to be inverted in equation 1.3.2.1, only the sensitivity matrix will be factorized, yielding:

$$S = X \cdot W \cdot Y^H \qquad (1.3.2.2)$$

As in feed forward regularization, X and Y are square matrices of dimension the number of voxels to be unfolded and W is a diagonal square matrix with the SVs ordered from higher to lower, as described in 1.3.1. If the expression in equation 1.3.2.2 is introduced in equation 1.3.2.1, after doing some operations the following equation for the unfolding matrix is obtained (for more information on this process, go to [47]):

$$U = Y \cdot W' \cdot X^H \qquad (1.3.2.3)$$

Where W' is defined as a matrix whose values in the diagonal are derived from the SVs of the sensitivity matrix as:

$$W'_{i,i} = \frac{W_{i,i}}{{W_{i,i}}^2 + \alpha^2} \qquad (1.3.2.4)$$

$$Where\ W' = diag(W'_{i,i})$$

(Again, for more information on this derivation, go to [47]).

"α" is a tunable factor, but it is dependent on the λ from equation 1.3.2.1, so indeed there is only one regularization factor, λ. The relationship between λ and α is calculated as:

$$\alpha = \sqrt{\lambda} \cdot W_{1,1} \qquad (1.3.2.5)$$

Where $W_{1,1}$ is the largest SV of the sensitivity matrix. The truncation factor with which truncated SVD is obtained is the same regularization factor used in Tikhonov regularization, λ. Unlike happens in feed forward regularization, the truncation factor does not need to be specified, as the same factor for truncation than for regularization is used. Consequently, the truncated SVD [46] in Tikhonov regularization is applied as:

$$W'_{i,i} = \begin{cases} \frac{W_{i,i}}{{W_{i,i}}^2+\lambda \cdot {W_{1,1}}^2} \;\; if \;\; W_{i,i} \geq \lambda \\ 0 \; if \; W_{i,i} < \lambda \end{cases} \qquad (1.3.2.6)$$

Then, this last expression in equation 1.3.2.6 is introduced in equation 1.3.2.3. The whole method can be visually simplified with the following diagram:

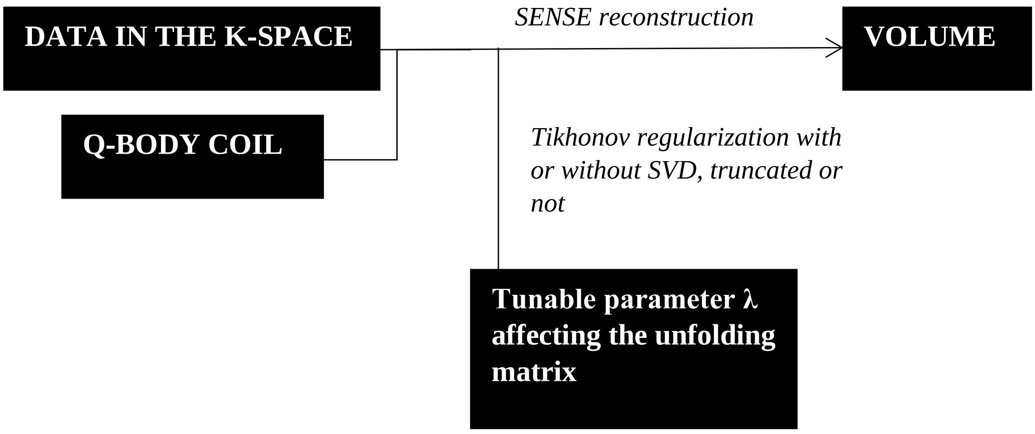
DATA IN THE K-SPACE
SENSE reconstruction
VOLUME
Q-BODY COIL
Tikhonov regularization with or without SVD, truncated or not
Tunable parameter λ affecting the unfolding matrix

Fig 16. Simple scheme describing Tikhonov regularization applied to SENSE reconstruction

1.3.3 Feedback regularization [50]

Feedback regularization works differently from the two previous methods proposed. While the two previous methods go from inputs obtained or introduced manually before the actual scan was carried out, feedback regularization will be performed with a first estimate image obtained after the MR scan to regularize SENSE reconstruction, being for that reason called *feedback*. This estimate image is obtained from a first SENSE reconstruction.

To reduce the noise amplification during the regularization process for the second and definitive reconstruction, the first estimate image is initially applied a truncated SVD during the first reconstruction and it is low-pass filtered, normally with a median filter [51] in which a certain kernel or neighborhood size is stated, substituting each voxel in the input image by the median value of the neighborhood of that voxel in the input image, allowing in that way to reduce the presence of variations in the image (in other words, reducing noise), but also smoothing the edges of the image, making it more homogeneous. However, as this image is only going to be used as estimate, it is not a serious problem if some edges are lost always that many noise is reduced.

To start the second reconstruction, standard SENSE is performed to obtain the definitive reconstructed volume [38] , but instead of using the same sensitivity matrices from the initial sensitivity maps, as in the first reconstruction, the sensitivity matrices will be multiplied by a diagonal matrix with the intensity values of the median filtered first reconstruction in the coordinates of the voxels that need to be unfolded in the second reconstruction, being its dimension the number of voxels to be unfolded, obtaining what are called *in vivo sensitivities*. These diagonal matrices are calculated as follows:

$$V = diag(vector\ with\ voxel\ values\ from\ filtered\ estimate\ image) \quad (1.3.3.1)$$

$$S_{in-vivo} = S \cdot V \quad (1.3.3.2)$$

Where S is the original matrix of sensitivities computed in the reconstruction of the first estimate image.

Then, the final expression for computing the unfolding matrix in this regularization method will depend on a regularization factor λ (different from the λ used in feed forward regularization and the λ used in Tikhonov regularization), with the sensitivity matrices affected not only by the information coming from the sensitivity maps of all the coils, but also from the information from the first filtered estimate, being computed as:

$$U = V \cdot S_{in-vivo}^{H} \cdot (S_{in-vivo} \cdot S_{in-vivo}^{H} + \lambda \cdot I)^{-1} \quad (1.3.3.3)$$

As happened in the two previous methods proposed, too high λs will induce folding artifacts in the second reconstructed image, while too low λs will have a very low noise reduction.

SVD can also be applied in this method for a further noise reduction, by identifying which voxel values to be unfolded contribute little to image reconstruction and only induce noise amplification. This SVD can be truncated or not by the factor λ. Similar equations to equations 1.3.2.2 to 1.3.2.6 can be applied here to apply truncated SVD and reduce noise, obtaining finally the second and definitive reconstructed image.

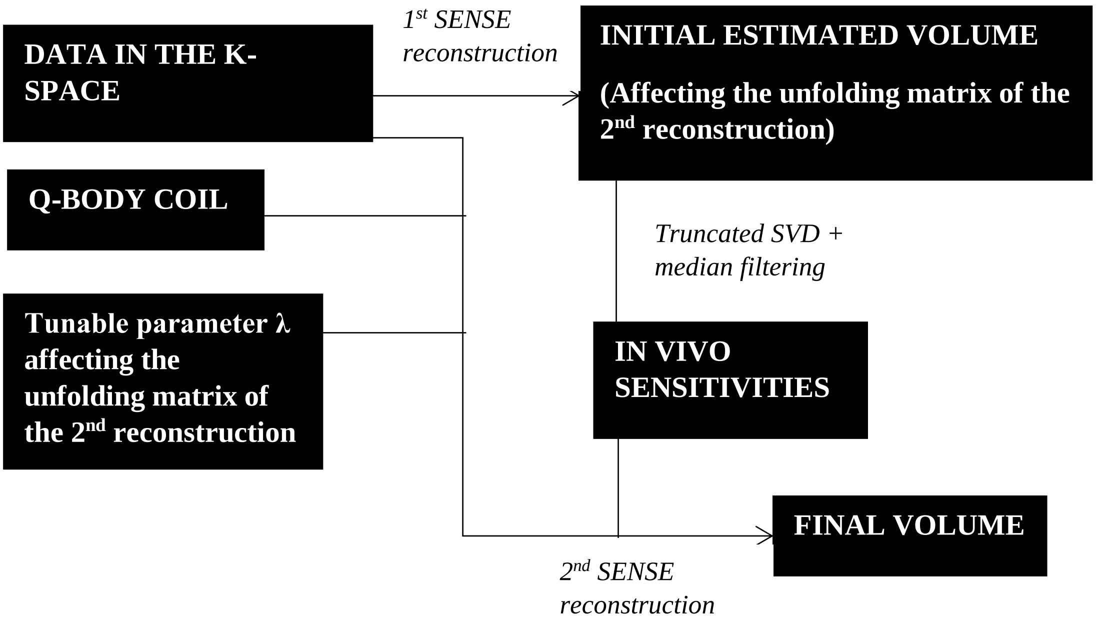
DATA IN THE K-SPACE
1st SENSE reconstruction
INITIAL ESTIMATED VOLUME
(Affecting the unfolding matrix of the 2nd reconstruction)
Q-BODY COIL
Truncated SVD + median filtering
Tunable parameter λ affecting the unfolding matrix of the 2nd reconstruction
IN VIVO SENSITIVITIES
FINAL VOLUME
2nd SENSE reconstruction

Fig 17. Simple scheme describing feedback regularization

1.3.4 Alternative regularization methods

The previous regularization methods were later on tested in a numerical phantom and with the real data from a volunteer (see Materials & Methods section). However, other regularization methods for SENSE reconstruction denoising were reviewed as well in the bibliography as an alternative to the previous ones.

Some of these alternative methods provided reconstruction results with a lower level of noise than the regularization methods that were finally implemented in the thesis, but they were quite complex and they did not have an exact equation to apply regularization, as happens in equation 1.3.1.1 for feed forward regularization, in equation 1.3.2.1 for Tikhonov regularization and in equation 1.3.3.3 for feedback regularization, having to be applied iteratively and consuming too much computational time.

Consequently, as they were so complex and consumed so much time, they were discarded to be used in the algorithm that was later on implemented (see point 1 of Materials & Methods section). Furthermore, some of the reviewed methods computed an automatic regularization factor, while the thesis wanted to test different levels of regularization, discarding also some algorithms because of this fact. As long as the same regularization methods for SENSE reconstruction were applied in all the reconstructions that were implemented, it was enough for the algorithm proposed, so the regularization method had to be effective for denoising, but not too complex, preferring to use one of the previous three algorithms than any other alternative. The alternatives that were reviewed were:

- Automatic regularization [52]: it is an advanced version of Tikhonov regularization which automatically computes after some iterations the best λ for denoising while avoiding artifact appearance. With the help of an optimizer, a certain λ is proposed in each iteration and the difference of the image of each iteration is computed with respect to the original SENSE reconstruction and with respect to images regularized too much that contain artifacts. The λ providing the highest differences with respect to both images is automatically assigned as the λ that has to be used to regularize.

- g-factor based Tikhonov regularization [49]: this method computes in the unfolding process of SENSE reconstruction the g-factor (see equation 1.3.13) for each voxel to unfold and assigns it as Tikhonov regularization factor (λ).

- Total Variation (TV) regularization [53]: it is used as an alternative for Tikhonov regularization that regularizes more or less depending on the gradient of the image, in order to preserve edges, as it has been observed that Tikhonov regularization may blur some edges. The TV is defined as the largest sum of all the changes in intensity of the image in a certain neighborhood [54] , so that edge regions yield high TVs, avoiding to be too much regularized. The regularization algorithm has a similar way of reducing noise than Tikhonov regularization, but is applied locally: low λs hardly reduce any noise, as there is almost no regularization with respect to the standard SENSE algorithm, while high λs may induce the appearance of folding artifacts since the method starts to deviate more and more from the standard SENSE reconstruction. It can be applied iteratively or not. Its performance is quite good in highly homogenous images with few edges, but in less homogenous images with more edges as are medical images, not so much denoising is performed and there is not a very large change with respect to Tikhonov regularization.

- Bregman regularization [55]: it is based on TV regularization, but it goes beyond its objective of avoiding the possible loss of edges that could happen in Tikhonov regularization, using the Bregman distance between iterations as regularization factor. The Bregman distance between the points P_1 and P_2 of a curve is defined as the distance from P_2 to the tangent line to that curve in P_1 [56]. In this case the curve would contain values for the TV of the image. The method is able to use high λs that remove noise efficiently without the appearance of any artifact, what is an important breakthrough with respect to all the previous methods that have been described. Unlike TV regularization, it is quite effective in non-homogenous medical images. However, it is applied iteratively, consuming many time, and in addition it has to be applied an optimal number of iterations, as if more iterations than the optimal number are applied, noise could reappear.

- Wavelet regularization [57]: unlike the rest of the methods that have been presented, it does not work in the image domain, but applies a Wavelet Transform (WT) (for more information on WT, go to [58]) to estimate the approximation and detail wavelet coefficients of the folded voxels to predict how the image is going to unfold without noise according to the Probability Distribution Function (PDF) of a Generalized Gauss-Laplace (GGL) distribution of the WT coefficients (for more information on this, go to [59] and [60]). Some modern versions of the algorithm are able to first isolate the areas of the image where artifacts are likely to appear, being able not only to predict from the WT coefficients of the folded voxels the final reconstructed image, but also to avoid the appearance of artifacts while denoising. The methods work in three approximation and detail levels in an iterative mode, so it is much more time consuming than any other method, spending almost six seconds to reconstruct each slice.

2. MOTIVATION & OBJECTIVES

The existing regularization methods described in the Introduction are able to remove enough noise in SENSE-reconstructed images so to have a good image quality, providing acceptable values of noise, SNR and CNR for coronary MRA images.

However, the only prior information that some of these algorithms use to denoise the reconstruction process is just the one coming from the Q-body coil. Consequently, the thesis proposes a method that tries to denoise SENSE reconstruction in a deeper way than all the state-of-the-art algorithms previously described, in order to achieve a better image quality, using an alternative level of prior information from a SENSE pre-reconstructed image. The results of this new method will be compared to the state-of-the-art methods to see if it succeeds in performing a further denoising or not.

Therefore, the main objective of the thesis is to denoise SENSE reconstruction more than state-of-the-art methods.

As more specific objectives, it is desired to test the existing regularization methods to compare them and see which one is simpler and more effective for SENSE reconstruction denoising. Then, another objective is to test regularized SENSE reconstruction in data from a volunteer with the most effective and simplest method chosen in the first objective. With that regularized SENSE reconstruction, the next objective is to implement an algorithm with an alternative level of prior information. The last objective of the thesis is to compare the result of the proposed algorithm with the current methods applied to see if the new algorithm is able to denoise SENSE reconstruction more than these current methods in terms of noise, SNR and CNR.

If all the previous objectives were fulfilled, a final objective would be to analyze by a visual criterion if the algorithm really enhanced diagnosis of abnormalities in the coronary trunk.

3. MATERIALS & METHODS

3.1 Proposed algorithm

To check whether the introduction of alternative *a priori* information in SENSE reconstruction did increase the quality of the image or not in coronary MRA cases with respect to already existing regularization methods, the following algorithm was designed:

1) SENSE reconstruction with Tikhonov regularization and truncated SVD was performed on the data of a coronary MRA, using also the help of the Q-body coil conventional prior information. The Tikhonov regularization factor applied was λ_1. The reconstructed image obtained was called from then on ***first reconstruction***.

2) The first reconstruction was in one case median filtered and in other case mean filtered [61] . The result from this step was assigned as prior information for a second reconstruction that was carried out in step 3. The level of prior information obtained in this step was the alternative level of prior information to be used with respect to current algorithms that the algorithm proposed for extra denoising.

3) A second SENSE reconstruction was performed, again with Tikhonov regularization, but with a different regularization factor with respect to step 1, being named as λ_2. It received as *a priori* information the image with the alternative prior information from step 2. The result of this step was named as ***second reconstruction with median filter***, if the reconstruction was performed with a first reconstructed image that was median filtered as prior information, or it was named as ***second reconstruction with mean filter***, if the reconstruction was performed with a first reconstructed image that was mean filtered as prior information. The algorithm ended in here, so the next steps dealt with its evaluation.

4) Mean and standard deviation measurements were performed in specific Regions of Interest (from now on, ROIs) in blood, myocardial muscle and skeletal muscle in the images to determine the level of noise, SNR and CNR. These measurements were carried out for a reconstruction without prior information, for the first reconstruction from step 1 and for both types of second reconstruction from step 3. The modalities were obtained with different combinations of λ_1 and λ_2 to see how measurements change with Tikhonov regularization.

5) Measurements for the different modalities in step 4 were compared between them in graphs and tables for a mathematical analysis and with the images of the reconstructed volumes for a visual analysis. Both analysis determined whether SENSE reconstruction with an alternative level of prior information actually reduced noise more than current methods with conventional levels of prior information, telling if image quality was enhanced or not.

6) If the algorithm succeeds in reducing noise amplification, more cases will be studied, and if in these cases, the algorithm keeps succeeding, a visual comparison in the MR workstation will be carried out between the already existing methods and the proposed method to really determine whether the introduction of alternative *a priori* information does enhance the anatomical details from the coronary trunk.

The workflow that was followed is displayed below.

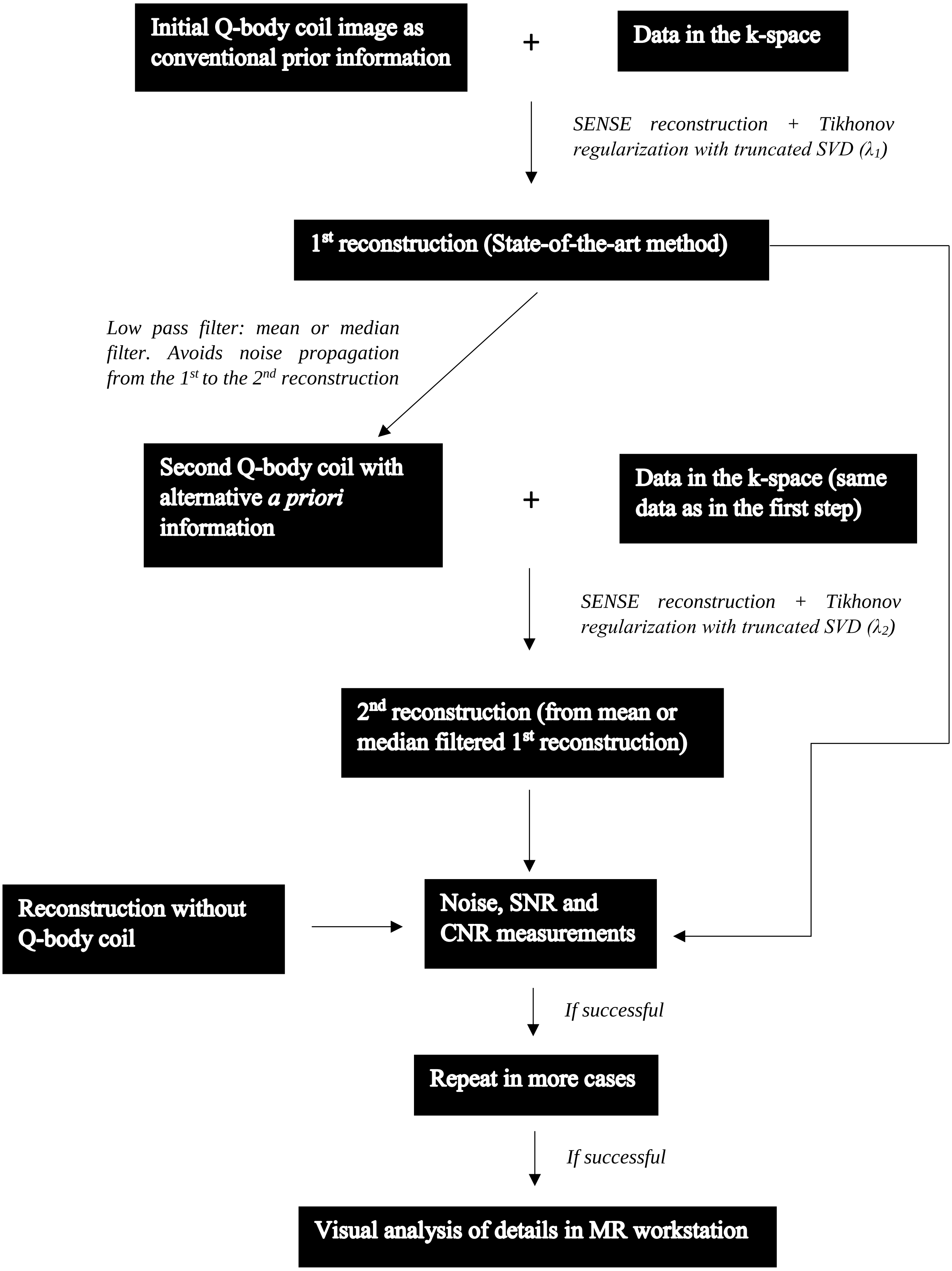
Initial Q-body coil image as conventional prior information
+
Data in the k-space
SENSE reconstruction + Tikhonov regularization with truncated SVD (λ_1)
1st reconstruction (State-of-the-art method)
Low pass filter: mean or median filter. Avoids noise propagation from the 1st to the 2nd reconstruction
Second Q-body coil with alternative a priori information
+
Data in the k-space (same data as in the first step)
SENSE reconstruction + Tikhonov regularization with truncated SVD (λ_2)
2nd reconstruction (from mean or median filtered 1st reconstruction)
Reconstruction without Q-body coil
Noise, SNR and CNR measurements
If successful
Repeat in more cases
If successful
Visual analysis of details in MR workstation

Fig 18. Schematic workflow followed in the thesis

3.2 Raw data acquisition

Raw data that was later on reconstructed and regularized with Tikhonov were obtained from a volunteer by performing a coronary MRA with a SSFP sequence, as described at the end of point 1.1.4 of the Introduction section. The acquisition was performed as follows:

The imaging volume covered the whole thorax in a coronal volume (350x500x300 mm^3 in FH (Foot Head) -LR (Left Right)-AP (Anterior Posterior) direction) with an isotropic acquisition resolution (same in all directions) of $1.5x1.5x1.5mm^3$. The sequence was based on 3D TFE- balance sequence [62] (a general sequence where SSFP [25] is a punctual case) with an echo train length of 45 profiles (how many echoes are acquired per TR) acquired in linear k-space filling order. To improve blood to myocardium contrast, flip angles of 1800 pulses were used with a half-alfa transient to the steady state (spin-echo approach [22]), resulting in a TR/TE of 3.26/1.63ms. To improve coronary vessels visualization, fat signal was suppressed using a spectral suppression technique (SPAIR, Spectral Attenuated Inversion Recovery [63]) with an inversion pulse [28] of 260ms (inversion pulses initially invert magnetization [11] , generally to suppress tissues like fluids or fat[27]).

To minimize movement/blurring artifacts cardiac trigger and respiratory pencil-beam [64] navigator were used (the acquisition was synchronized with the cardiac cycle and with breathing through the use of different mechanisms). The acquisition was accelerated using parallel acquisition [39] under-sampling with a SENSE factor [38] of 3x2 in LR and AP direction respectively, resulting in a total scan time of 218s assuming 100% respiratory navigator efficiency.

3.3 Phantom simulation

Before testing the algorithm in real data, the state-of-the-art regularization methods (the ones described in the points 1.3.1 to 1.3.3 of the Introduction section) were tested on a numerical phantom for their simulation and also for learning how to code these methods in the programming language to be used in the thesis, IDL™.

The numerical phantom image consisted in an axial slice of the patient together with some internal organs. The internal organs of the patient appeared in different tones of gray.

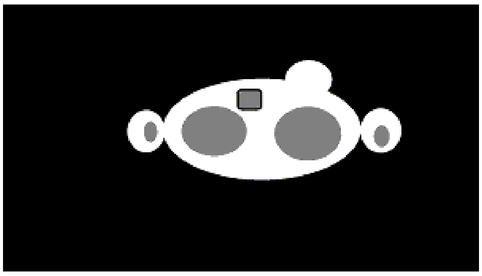

Fig 19. Numerical phantom used for SENSE reconstruction simulation

For initializing SENSE reconstruction, the following steps were performed in IDL™:

- The IDL™ function *dist* obtained with different spatial shifts provided a distance matrix that was used for obtaining the different sensitivity maps.
- The Fast Fourier Transform (FFT) of the numerical phantom was used as raw data. Some Gaussian noise was introduced to make the simulation closer to reality.
- A binary mask with zeros outside the phantom and ones inside was used as prior information to represent the Q-body coil image, being later used to multiply the sensitivity maps and the final reconstructed phantom, as stated by equations 1.3.2 and 1.3.12.

With all the input elements presented in the previous steps, the different stages for SENSE reconstruction[38] without any regularization nor prior information (see point 1.3) were coded in IDL™ programming language.

Once SENSE reconstruction without any regularization nor prior information had been carried out, the different regularization methods were coded in IDL™. The first method to be coded was feed forward regularization [44] , with the following steps:

- Introduction in the equation of the unfolding matrix (equation 1.3.9) the regularization matrix R, which relied on the square values from the Q-body coil image multiplied to different λs, as described in equations 1.3.1.1 and 1.3.1.2 of the Introduction section.
- Performance of a truncated SVD [45], [46] for the inverse problem with a truncating parameter of $\lambda=10^{-5}$ introduced manually, according to equations 1.3.1.3 to 1.3.1.5 of the Introduction section.

The other regularization approach which was coded with the phantom was Tikhonov regularization [47]–[49] with truncated SVD, as described in equations 1.3.2.1 to 1.3.2.6 in the Introduction. The different steps performed were:

- Introduction of different Tikhonov regularization parameters λ in the equation of the unfolding matrix.
- Performance of a truncated SVD for the inverse problem with a truncation factor equal to λ.

Feedback regularization [50] was not tested on the phantom because the algorithm proposed in the thesis has many similarities with this regularization method. Therefore, it was preferred to directly test the new algorithm in the images from the real case rather than doing many tests in a phantom that was just a simulation for the real case.

3.4 Algorithm implementation in IDL™

The programming language chosen to code the new algorithm was IDL™, with the Version 6.3, Microsoft Windows (Win32 x86 m32). (c) 2006, Research Systems, Inc.

Once all the data from the volunteer had been acquired from the MRI scanner, the next step was to reconstruct all the data in IDL™ following the algorithm described in point 3.1. But before starting to code the algorithm, the raw data had to be accessed and introduced in IDL™.

The code received as inputs two .list files containing header information to read the .data files, which were actually the files containing the raw data. Two pairs of .list and .data files had to be imported: one pair for obtaining the information for the surface coils and the Q-body coil to later on generate the sensitivity maps, and another pair for obtaining the raw data acquired from the patient. Furthermore, two text files were also introduced as inputs, containing information on the acquisition (voxel size, Field of View (FOV), if the acquisition was decentralized or taken with a certain angle and many other aspects). These two text files were known as *protocols* and there were two types: the scanning protocol and the reference protocol.

The .list and .data files for the coils and the raw data were read at the same time. To describe how the reading process was carried out, the structure of the .list files has to be described briefly:

- Initially, the .list file contained some acquisition values also present in the protocols. Some of these values were read, as they were later on important for the reconstruction.
- Next, the .list file indicated the structure of the lines of the header (what information each value of each line was transmitting). These lines made reference to the actual data in the .data file. They should not be confused with the data present in the .data file.
- At last, it contained the lines where the information on how to access the .data files was located.

The .list file for the coils kept some information from the beginning of the files, as could be for instance the resolution of the images of the coils and the number of surface coils used in the acquisition in parallel. Then, from the data lines, it kept the following:

- An index that differentiated between the Q-body coil and the surface coils.
- In case the information was for a surface coil, an index which told what surface coil the line was talking about.
- Two indexes indicating the position of the coil data in the k-space.
- A last index telling in which position of the .data file the value for that position in the k-space was located. Consequently, what the reader did was to access the .data file in that position and introduce it in a matrix in the position specified by the indexes of the previous point.

The dimensions of the coils in the .list files were sorted as FH x LR x AP, so their order had to be changed into LR x AP x FH, in order to produce matrices with axial slices. In addition, the .list files did not identify coil number 0 as the first coil of the acquisition, so the minimum coil number was identified and substracted to all the coil numbers to make the first coil be the zeroth coil. Finally, the reader function for the coils' information yielded a Q-body coil matrix with dimensions: LR resolution x AP resolution x FH resolution; and a surface coil matrix with those same dimensions together with an extra dimension telling the number of coil, from 0 to a maximum (in this case, 15).

Next, the protocols were read. In this case, the reader function initialized a structure (*struct*) with the different fields present in the protocol that were of interest for the reconstruction. The fields for the structure were filled as the reader was finding the information from those fields inside the text file. In the end, the function produced a structure with information for the FOV, the voxel size, the SENSE factors[38], the deviation from the center of the scan, the angulation… and many other fields.

Then, the raw data in the k-space were extracted from the .list and .data files for the raw data, in a similar way to the coils' data. From the beginning of the .list file, more information was gathered in comparison to the coils' case, as could be for example the range of coordinates in the three directions of the k-space, the oversampling factor for each direction of the k-space (which indicates how many times the initial dimensions of the k-space can be increased to avoid aliasing artifacts) and other fields. From the header lines of the file, the following values were saved:

- The number of the surface coil which acquired the data represented in each line.
- The position in the k-space from where the data was acquired.
- The position in the .data file where the data value for the coil and position in the k-space that have been read is located.

Before creating the matrix with the raw data in the k-space, some adjustments had to be performed:

- As in the coils' case, the minimum number for the coils was not 0, so the minimum number had to be obtained to substract all the coil numbers to it.
- The k-space coordinates had to be multiplied by the SENSE factors, as the raw k-space was reduced by these factors.
- The reference frame established in the .list files for the k-space coordinates set as zero the center of the k-space, having negative coordinates, so all the coordinates were shifted so they could go from 0 to a maximum. In other words, the reference frame for the k-space was shifted from the center to one of the corners.

Finally, the position of the .data file from each row of the .list file was accessed to obtain the raw data values, being also Gaussian filtered[65] to favor low frequencies, as Gaussian filters enhance the center of the k-space, where low frequencies are located. These values were assigned to a matrix with the correct dimensions for the number of coils and for the k-space coordinates, yielding a raw data matrix of dimensions: LR resolution x AP resolution x FH resolution x Number of coils. The raw data matrix was later on masked and filtered again with a Gaussian low pass filter that only acted inside non-zero data values and only in low frequencies.

Schemes with the obtention of the different kinds of data is displayed below:

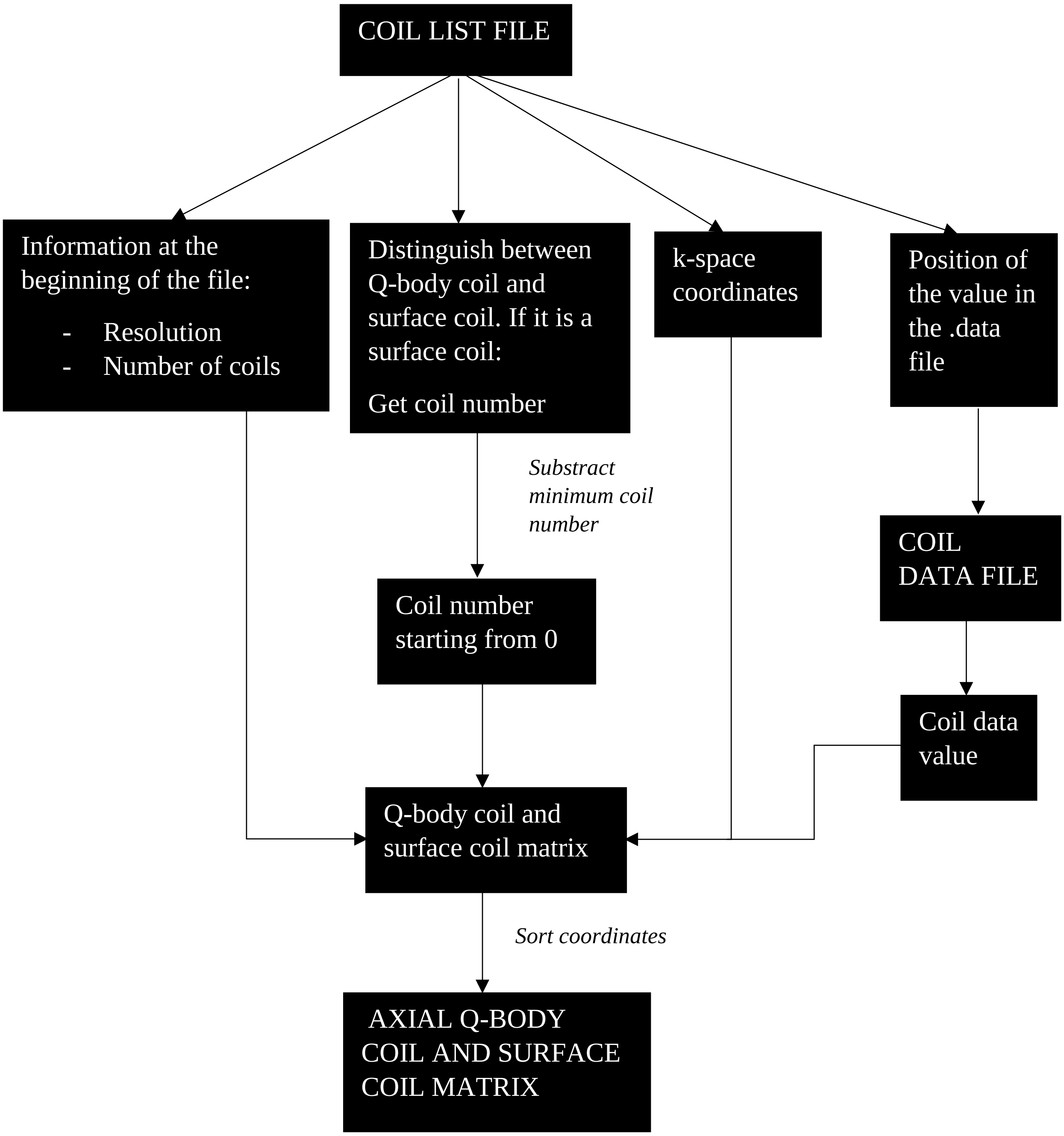
COIL LIST FILE
Information at the beginning of the file:
- Resolution
- Number of coils
Distinguish between Q-body coil and surface coil. If it is a surface coil:
Get coil number
k-space coordinates
Position of the value in the .data file
Substract minimum coil number
Coil number starting from 0
COIL DATA FILE
Coil data value
Q-body coil and surface coil matrix
Sort coordinates
AXIAL Q-BODY COIL AND SURFACE COIL MATRIX

Fig 20. Scheme for the obtention of the coils' data

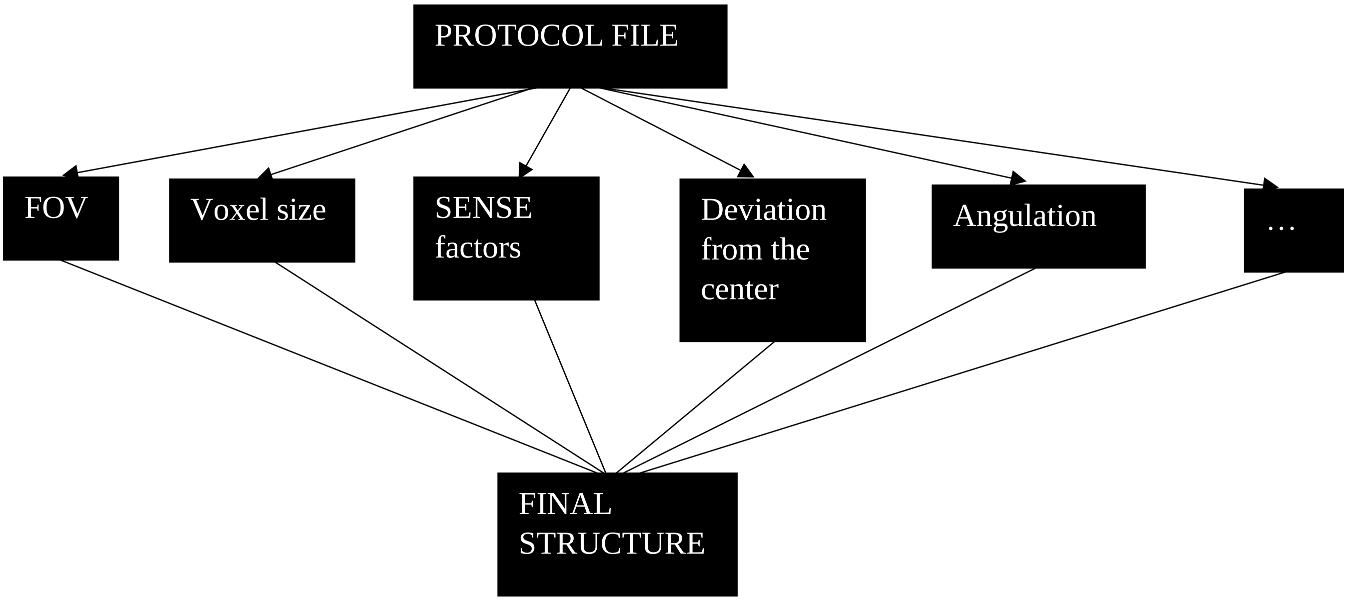
PROTOCOL FILE
FOV
Voxel size
SENSE factors
Deviation from the center
Angulation
…
FINAL STRUCTURE

Fig 21. Scheme for the obtention of the protocol data

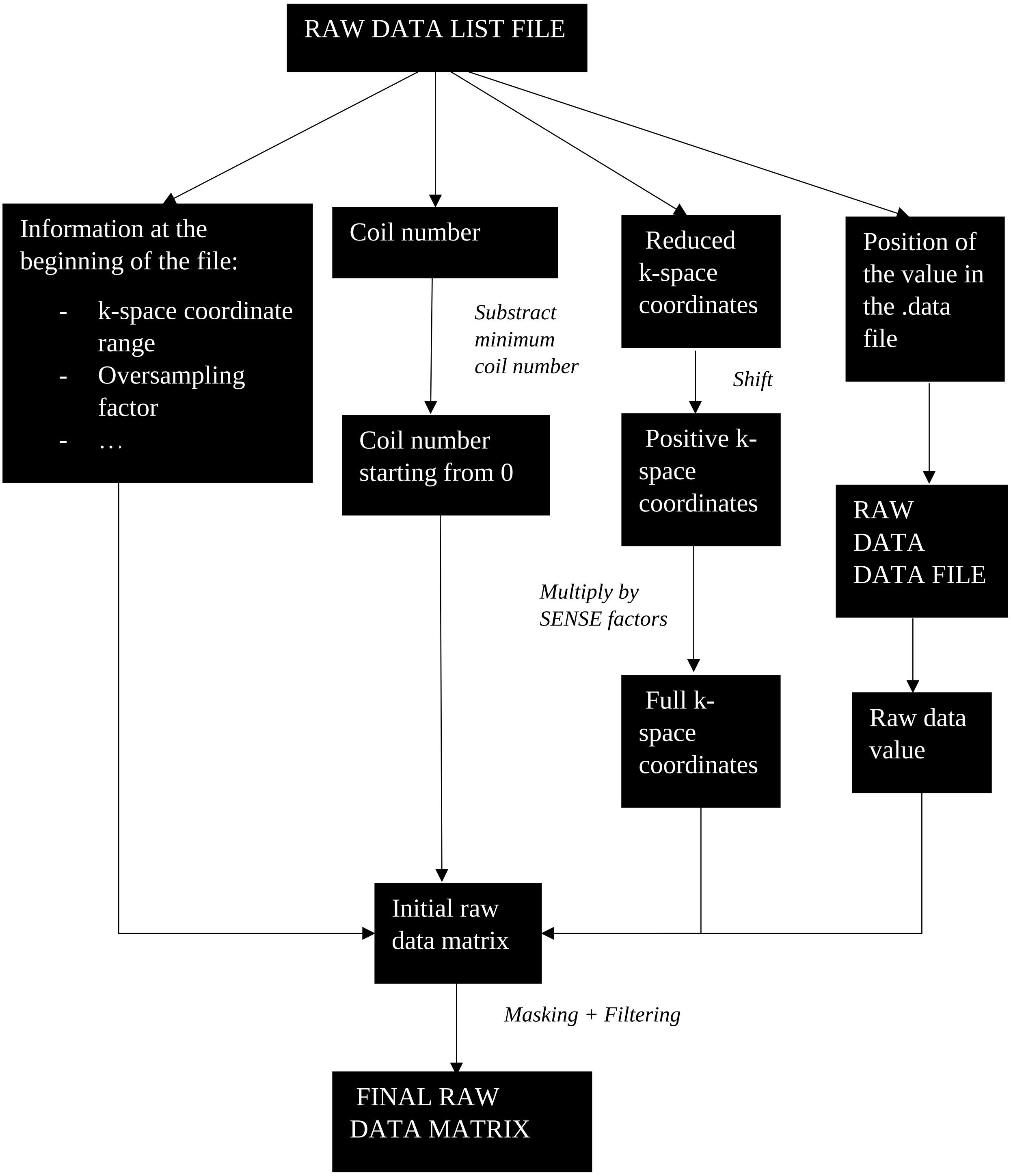
RAW DATA LIST FILE
Information at the beginning of the file:
- k-space coordinate range
- Oversampling factor
- …
Coil number
Substract minimum coil number
Coil number starting from 0
Reduced k-space coordinates
Shift
Positive k-space coordinates
Multiply by SENSE factors
Full k-space coordinates
Position of the value in the .data file
RAW DATA DATA FILE
Raw data value
Initial raw data matrix
Masking + Filtering
FINAL RAW DATA MATRIX

Fig 22. Scheme for the obtention of the raw data

When all the raw data were read and introduced in a format that could be easily handled by IDL™, the next step was to obtain the sensitivity maps with the surface coil matrices and the Q-body coil matrix. Initially, the coils' information was in the k-space, so for obtaining it in the image domain, their Inverse Fast Fourier Transform (IFFT) was calculated. According to equation 1.3.1 in the Introduction, to obtain the sensitivity map for each surface coil, the information for the surface coil had to be divided by the image yielded by the Q-body coil [13] .

Consequently, both images had to be aligned so that each voxel of the surface coil image could be normalized by the same voxel in space of the Q-body coil image, so the receiver coil images resolution was adjusted to the Q-body coil image resolution, taking into account the deviation from the center of the coordinates of the surface coil images. Once the resolution and the deviations from the center were adjusted, the images were centered in the FOV of the reference protocol. Next, both surface coil and Q-body coil images were masked and Gaussian filtered [65] to avoid noise propagation. Finally, the adjusted images were divided by the Q-body coil image, yielding a matrix with the sensitivity maps of dimensions: LR resolution x AP resolution x FH resolution x Coil Number (the dimensions correspond to the full FOV, not to the reduced one).

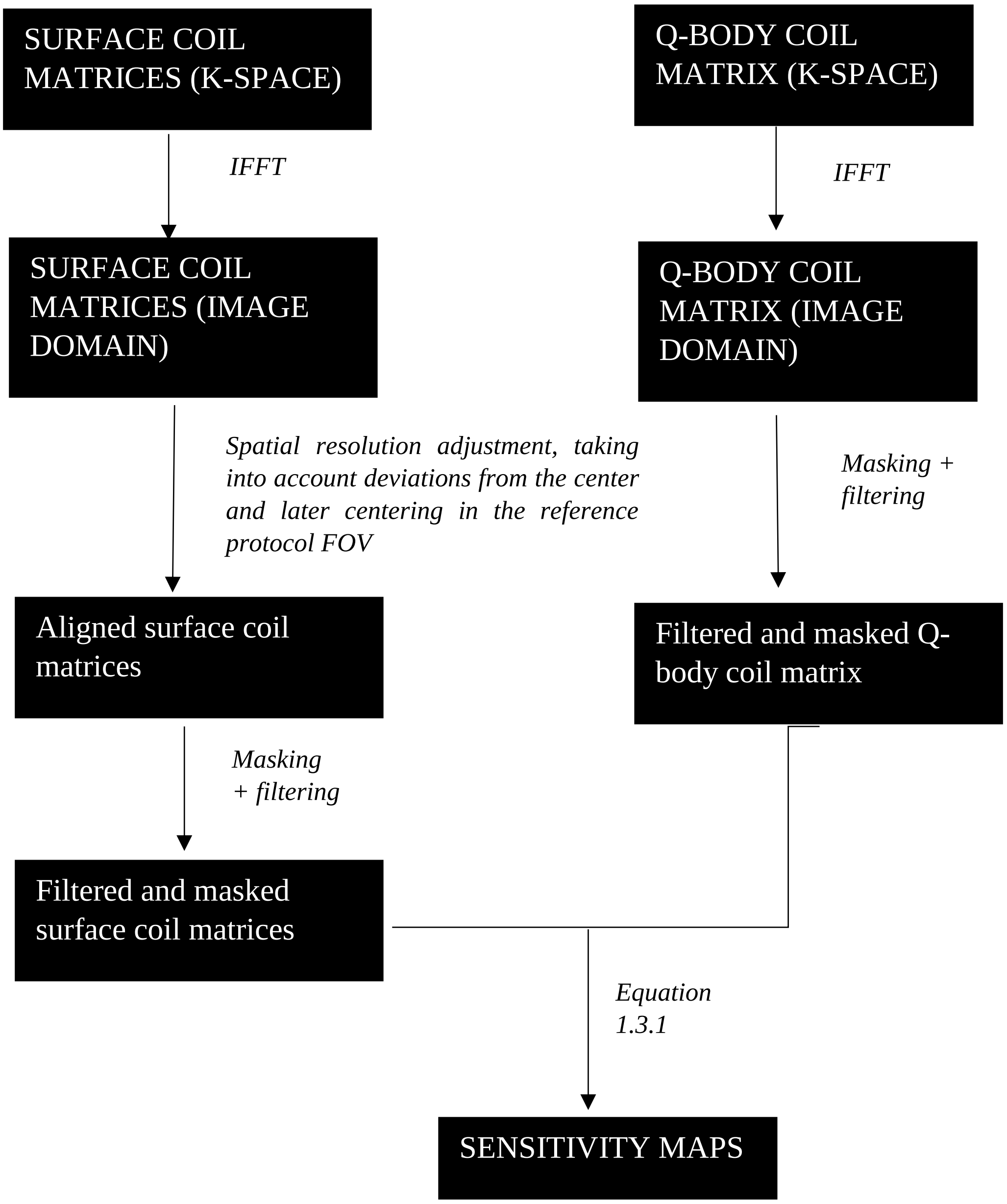
SURFACE COIL MATRICES (K-SPACE)
Q-BODY COIL MATRIX (K-SPACE)
IFFT
IFFT
SURFACE COIL MATRICES (IMAGE DOMAIN)
Q-BODY COIL MATRIX (IMAGE DOMAIN)
Spatial resolution adjustment, taking into account deviations from the center and later centering in the reference protocol FOV
Masking + filtering
Aligned surface coil matrices
Filtered and masked Q-body coil matrix
Masking + filtering
Filtered and masked surface coil matrices
Equation 1.3.1
SENSITIVITY MAPS

Fig 23. Scheme for the obtention of the sensitivity maps

With the sensitivity maps obtained, it was time to perform SENSE reconstruction [38]. For that purpose, data were sampled according to the SENSE factors' values both in the phase and frequency encoding direction (rows and columns), taking one sample in each direction out of a certain number of lines indicated by the SENSE factors. The number of samples taken in a certain direction was the closest and highest integer to the division of the number of elements in that direction in the full FOV over the SENSE factor in that direction. This had to be specified because it could happen that the number of elements in a certain direction was not divisible by the SENSE factor. In the end, reduced k-space data are obtained.

Then, equations 1.3.1 to 1.3.12 were coded in IDL™ together with equations 1.3.2.1 to 1.3.2.6, which corresponded to SENSE reconstruction regularized by Tikhonov [47]–[49] with truncated SVD [45], [46] , using a certain λ known as λ_1, obtaining a first pre-reconstructed volume with the help of the Q-body coil image as prior information.

This volume was low-pass filtered either with a median [51] or with a mean filter [61] to avoid noise propagation [41] . These filters performed a convolution of the volume with a kernel (in this thesis, of size 5x5x5), in such a way that this kernel went through all the voxels of the volume computing either the mean value of the neighborhood of each voxel or the median. These low-pass filtered volumes were assigned as prior information images for the second and definitive SENSE reconstruction with Tikhonov regularization with truncated SVD, using a λ known as λ_2 to produce the final reconstructed volume, which was expected to be less noisy than the volumes obtained with the state-of-the-art methods.

The code was not only used for obtaining the regularized images with an alternative level of prior information as described in point 3.1, but some parts of the code were also used to reconstruct images with different levels of prior information that were later on compared to the results of the algorithm proposed.

The code was also used to obtain a set of reconstructed images without prior information from the Q-body coil, so for that purpose the Q-body coil information was used only for generating the sensitivity maps for the reconstruction. The parts of the code which used the Q-body coil information for other purposes was deactivated.

Furthermore, the first reconstructed volume with prior information from the Q-body coil and regularized with a Tikhonov factor λ_1 with truncated SVD was also extracted from this code. The only difference that the code presented for obtaining this volume with respect to obtaining the volume resulting for the algorithm was the code execution was stopped once the first reconstructed volume had been calculated.

The whole code will be summarized schematically below. In red appear those parts of the code which were deactivated for obtaining either reconstruction without prior information from the Q-body coil or for just obtaining the first reconstructed volume.

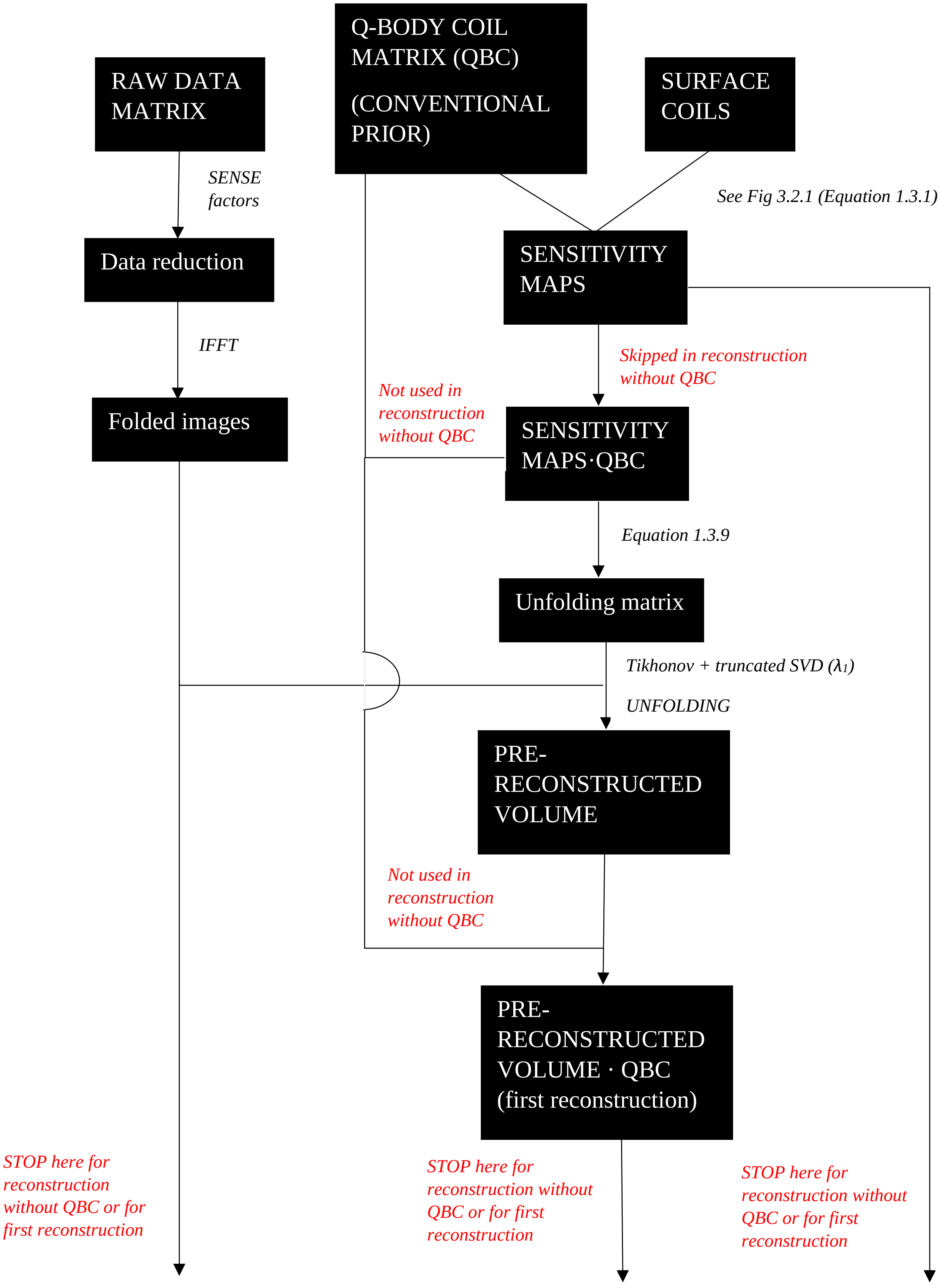
RAW DATA MATRIX
Q-BODY COIL MATRIX (QBC)
(CONVENTIONAL PRIOR)
SURFACE COILS
SENSE factors
See Fig 3.2.1 (Equation 1.3.1)
Data reduction
SENSITIVITY MAPS
IFFT
Skipped in reconstruction without QBC
Not used in reconstruction without QBC
Folded images
SENSITIVITY MAPS·QBC
Equation 1.3.9
Unfolding matrix
Tikhonov + truncated SVD (λ1)
UNFOLDING
PRE-RECONSTRUCTED VOLUME
Not used in reconstruction without QBC
PRE-RECONSTRUCTED VOLUME · QBC (first reconstruction)
STOP here for reconstruction without QBC or for first reconstruction
STOP here for reconstruction without QBC or for first reconstruction
STOP here for reconstruction without QBC or for first reconstruction

CONTINUES IN NEXT PAGE

(Only for second reconstruction)

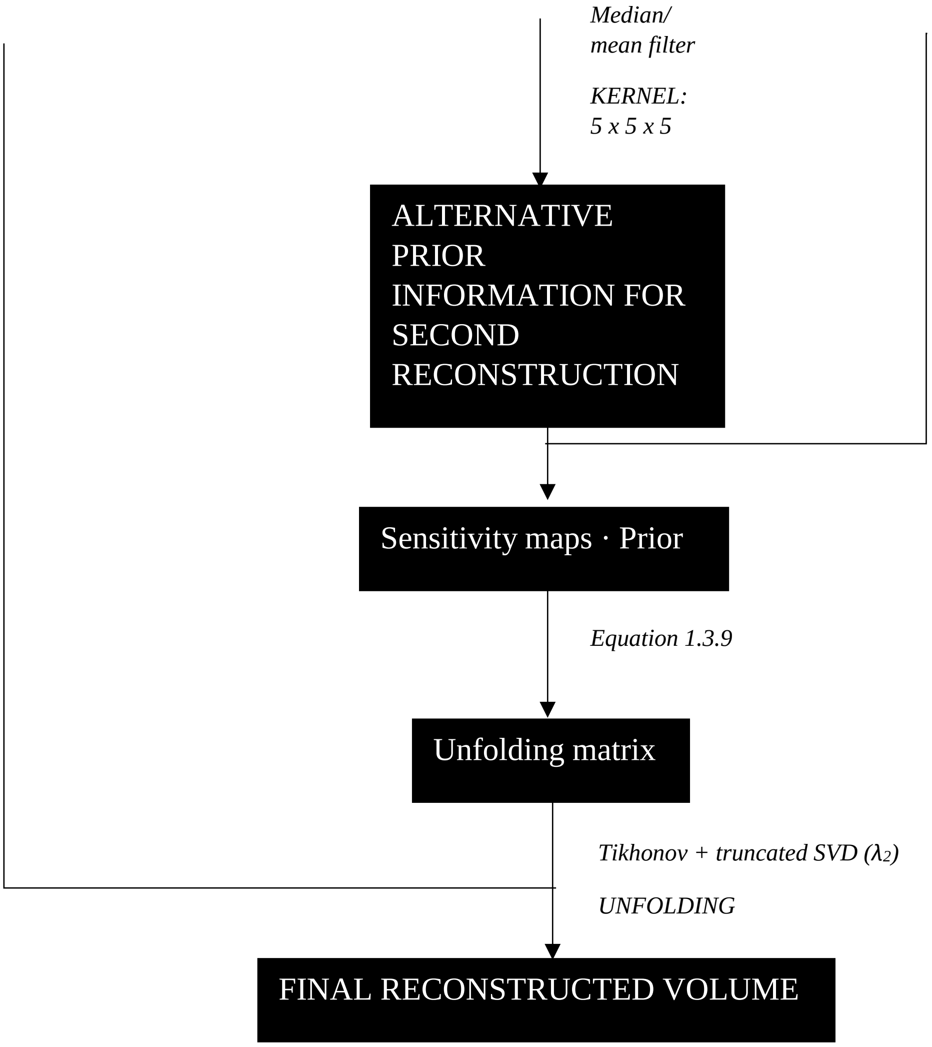
Median/
mean filter
KERNEL:
5 x 5 x 5
ALTERNATIVE PRIOR INFORMATION FOR SECOND RECONSTRUCTION
Sensitivity maps · Prior
Equation 1.3.9
Unfolding matrix
Tikhonov + truncated SVD (λ_2)
UNFOLDING
FINAL RECONSTRUCTED VOLUME

Fig 24. Schematics of the overall code designed in IDL™

3.5 Phantom evaluation

The evaluation of the numerical phantom results was just performed by eye, as it was just a simulation for getting familiar with the different regularization methods that could be applied for denoising SENSE reconstruction. The mathematical results that could have been extracted would not have been significant for the real case. It was preferred to dedicate all the time and efforts into coding the algorithm and evaluating it in the real case, as it would really be the analysis that informed us whether the results of the algorithm were going to be acceptable or not.

3.6 Algorithm evaluation

In the real case with the volunteer's data, to establish comparisons between the new algorithm and the state-of-the-art methods, four modalities of reconstruction were performed with the IDL™ code: reconstruction without Q-body coil or without prior information (from now on called ***reconstruction without Q-body coil***, as all the prior information in the state-of-the-art methods came from the Q-body coil information), reconstruction with Q-body coil or ***first reconstruction*** (as it was the first reconstruction that had to be performed to later on obtain the second and definitive reconstruction), ***second reconstruction obtained with a median filtered*** first reconstructed volume and ***second reconstruction obtained with a mean filtered*** [61] first reconstructed volume. To obtain each modality, different parts of the code were activated or deactivated, as can be seen in the parts in red in figure 24. The Tikhonov regularization parameters that in theory reduced noise the most in the images without introducing folding artifacts were introduced. For that purpose, the values of λ_1 and λ_2 that were introduced in the code were between 10^{-3} and 10^{-1} for λ_1 and between 10^{-3} and 1 for λ_2, as they were the maximum ones that did not introduce folding artifacts.

The volumes for the different reconstruction modalities were saved as .dat files in IDL™ and introduced in the image processing software ImageJ™, where some Regions of Interest (ROIs) were selected with the oval tool provided by this software. With these ROIs, the following procedure was carried out:

- Selection of apparently homogenous regions normally distributed in different tissues of the patient in different slices. The tissues selected were the most representative in a coronary MRA: blood, myocardial muscle and skeletal muscle (pectoral muscle), while the slices selected corresponded to slices in which the heart occupied a large section in the image. The slices taken were slices -7, -2, +3 and +7 according to the coordinate system provided by the input files in the IDL™ code, where the first slice was slice -100, representing the neck, and the last slice was slice +100, representing the hip. Therefore, the MRI was performed in the whole trunk of the patient.

- The ROIs for different tissues and slices were saved as .roi files in order that the noise, SNR and CNR measurements were always applied in the same voxels for different reconstruction methods. Here it can be seen some of the ROIs selected for the different tissues:

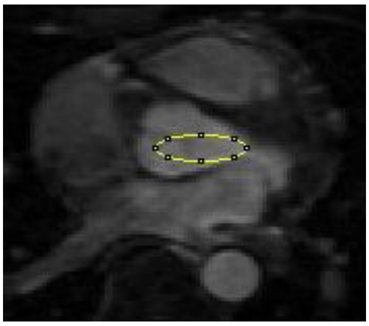

Fig 25. ROI (highlighted with a yellow oval with ImageJ™) in blood in slice +3

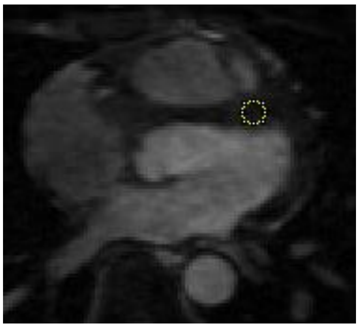

Fig 26. ROI (highlighted with a yellow oval with ImageJ™) in myocardial muscle in slice +7

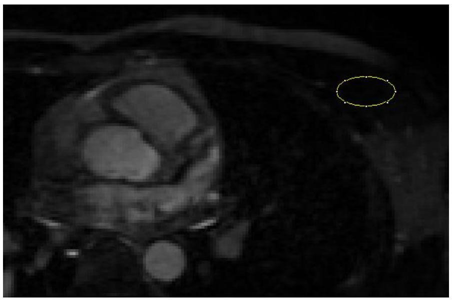

Fig 27. ROI (highlighted with a yellow oval with ImageJ™) in pectoral skeletal muscle in slice -7

- By performing the ImageJ™ commands Analyze → Measure or the shortcut Ctrl+M when the oval region with the ROI was selected, some features of the ROIs were measured in ImageJ™. From all of them, the most important for the thesis were the standard deviation and the mean.

- With the mean and the standard deviation values of each ROI, noise, SNR and CNR measurements could be performed in the following way:

$$Noise = \frac{\sigma(ROI)}{\mu(ROI)} = CV(ROI) \qquad (3.6.1)$$

$$SNR = \frac{\mu(ROI)}{\sigma(ROI)} \qquad (3.6.2)$$

$$CNR = \frac{\mu(blood\ ROI) - \mu(myocardial\ or\ skeletal\ muscle\ ROI)}{\sigma(blood\ ROI)} \qquad (3.6.3)$$

- The noise [41] could have been assumed to be just the standard deviation of the ROI, but to highlight its significance in each of the tissues where it was measured, it was divided over the mean value of the ROI, being assumed to be the Coefficient of Variation (CV) of that ROI. For instance, it is not the same to have a noise (expressed just like a standard deviation) of 5 if the average value of the ROI is 10, than if the mean value of the ROI is 100.

- The SNR was defined as the expected value of each ROI over its standard deviation [43] , as the signal was assumed to be the mean value of the ROI and the noise was assumed to be the standard deviation. In that way, if the noise is high, the SNR is reduced, as the importance of the main signal over the noise is low. The opposite happens if the noise is low, so if noise has a low value, the standard deviation is low, the image is more homogeneous and the SNR will be high, as the importance of the main signal with respect to noise is higher.

- The CNR was computed with respect to the mean and standard deviation values in blood [31] , as blood was the reference tissue in coronary MRA [26] , being the CNR defined as the difference between the expected intensities in blood with respect to myocardial or skeletal muscle over the standard deviation in blood.

- For the same slice and tissue, four measurements were taken to obtain noise, SNR and CNR measurements as more reliable as possible and with a certain uncertainty. The measurement finally taken was the average value of the four measurements while the uncertainty was represented by their standard deviation.

When all the measurements of noise, SNR and CNR were completed for all the tissues and slices, they were transferred to a Microsoft Excel™ spreadsheet, where they were saved column by column and used for representing all the information from the different reconstruction modalities in graphs. As the amount of information was quite high, it was decided to place the same measurements from the same tissue and slice in the same graph. This also helped to see and compare the results visually. Four measurements of noise, SNR and CNR in the same slice, tissue and combination of regularization factors (λ_1 and λ_2) were performed, so the graphs later on displayed the average values of those measurements, while their uncertainties were displayed in tables. Many graphs were produced in Microsoft Excel™, so only the most representative ones were depicted in the Results section.

The Tikhonov regularization parameters chosen to regularize the images where the measurements were carried out were the factors denoising the most SENSE-reconstructed images while not introducing folding artifacts, going **from 10^{-3} to 10^{-1} in λ_1 and from 10^{-3} to 1 in λ_2** [47]–[49] , so the graphs and the tables in the Results section will show measurements in function of those regularization factors.

Together with the graphs and the tables, some images of the real case were displayed in the Results section. To obtain them, the whole 3D volume for each reconstruction method was obtained running the code in IDL™ in sets of fourteen slices, as there was a memory shortage in IDL™ that made impossible to reconstruct the whole volume at once. Once all the volumes of fourteen slices contained in the main volume were obtained, they were saved as .dat files, opened again and joined into just a whole volume of all the slices with a program designed in IDL™. Then the joined volumes were opened as raw files in ImageJ™ and with the operation Ctrl+Shift+H; axial, coronal and sagittal views of those volumes could be visualized. The fact that image volumes were reconstructed in sets of fourteen slices and later on joined in a whole volume may have introduced small artifacts in the coronal and sagittal views, but in theory they should be unappreciable. Axial, coronal and sagittal views of these volumes were later on displayed in the Results section.

As happened with the information from the graphs and the tables, too many images corresponding to many combinations of λ_1 and λ_2 were produced, so in the Results section only the images corresponding to one combination of λ_1 and λ_2 were later on displayed.

The combination chosen for displaying the images in the Results section was the one that, theoretically, decreased noise more while did not produce folding artifacts, staying practically in the limit before folding artifacts started to appear in the image. Consequently, the combination chosen was that one that visually was expected to offer a higher difference between the different reconstruction modalities. This combination was **$\lambda_1=10^{-1}$ and $\lambda_2=10^{-2}$**. λ_1 is larger than λ_2 for, theoretically, denoising the image as most as possible without the appearance of artifacts and to avoid the noise expansion from the first to the second reconstruction

Eventually, all the derivations extracted from the graphs, the tables and the images displayed in the Results section will be analyzed in the Discussion section and it will be explained whether the new algorithm worked better than the state-of-the-art methods by introducing alternative prior information.

4. RESULTS

4.1 Phantom simulation

The first results obtained correspond to the phantom that was designed for simulating SENSE reconstruction and the different regularization methods. Below are displayed the folded image for the aliased version of the phantom (to see the original phantom, go to figure 19 in the Materials & Methods section), the phantom image used as conventional Q-body coil prior information image and the final reconstructed image without the help of the Q-body coil image prior information nor the use of regularization methods (figures 28 to 30) [44][47]–[50]:

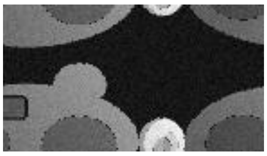

Fig 28. Folded image obtained by IFT after reducing the samples to be acquired in the k-space. The size of the image is represented at scale with respect to those images in figures 29 and 30.

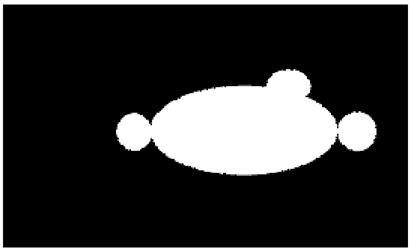

Fig 29. Image used as Q-body coil for the simulation

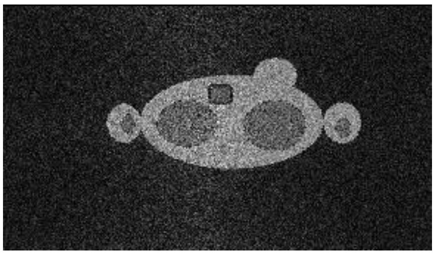

Fig 30. Final unfolded and reconstructed image without regularization and without the help of the Q-body coil, with some level of Gaussian noise introduced

In figure 28 it can be seen how the SENSE factors of two in the PE direction and two in the FE direction[29], [30], which were the ones chosen in the simulation, produce an image four times smaller than the original phantom image.

A phantom for the Q-body coil image was also designed (figure 29). This phantom multiplied the final reconstructed image in order to remove the noise from the outside of the body of the patient, avoiding that this noise affected the quality of the image inside the body of the patient.

Figure 30 represented the final reconstructed image without prior information nor regularization. SENSE reconstruction was an efficient method in unfolding the image from figure 28 but at the same time amplified the initial quantity of Gaussian noise introduced in the reconstruction and thus reducing SNR as stated in equation 1.3.13. Consequently, the reconstruction without prior information nor regularization was much noisier than the original phantom from figure 19, considered to be the gold-standard with which all reconstructions were compared.

Below, the resulting images of feed forward regularization (figures 31 to 33) applied to the phantom in an increasing order from left to right can be found. In addition, the Q-body coil phantom conventional prior information was also used in the reconstruction. In excessive regularization cases, folding artifacts were highlighted in red in a separate figure (figure 34).

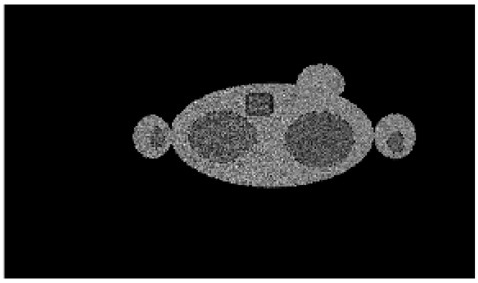

Fig 31. Final image reconstructed with $\lambda=0$ with feed forward regularization. For this case, no regularization was applied.

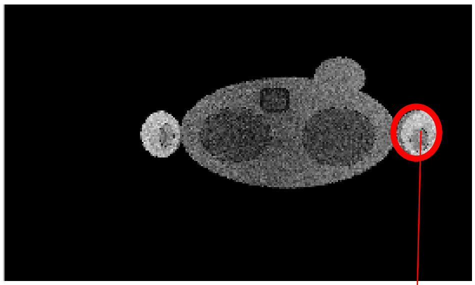

Fig 32. Final image reconstructed with $\lambda=10$ with feed forward regularization

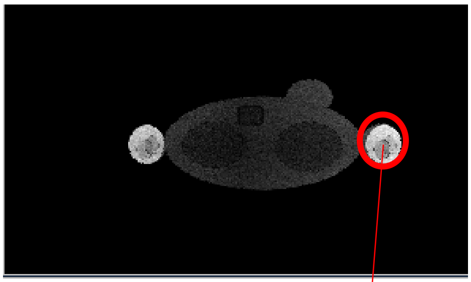

Fig 33. Final image reconstructed with $\lambda=100$ with feed forward regularization

Fig 34. Highlight of folding artifacts in images regularized with feed forward regularization

The visual inspection of the feed forward regularized images shows that more intense regularization factors seem to reduce noise in the phantom, being more homogenous, and the use of the Q-body coil phantom set to zero all the values falling outside the body. However, as the regularization was more intense, more folding artifacts started to appear, as shown in figure 34.

Next, the images for the regularized phantom with Tikhonov regularization in increasing order from left to right were displayed (figures 35 to 37). Again, in excessive regularization cases, a separate figure shows the folding artifacts present in there (figure 38). Furthermore, the reconstruction was carried out with the help of the Q-body coil phantom conventional prior information, too.

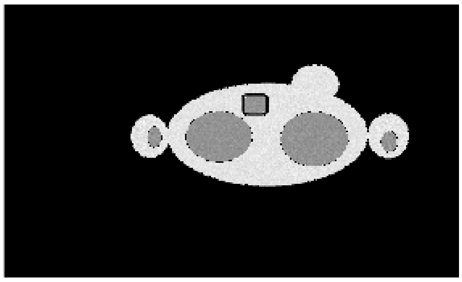

Fig 35. Image reconstructed with Tikhonov regularization with $\lambda=10^{-8}$

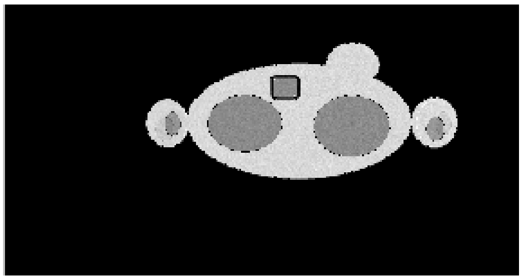

Fig 36. Image reconstructed with Tikhonov regularization with $\lambda=10^{-3}$

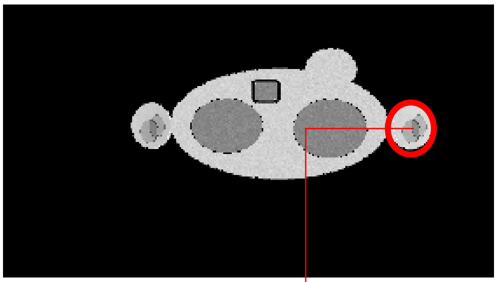

Fig 37. Image reconstructed with Tikhonov regularization with $\lambda=1$

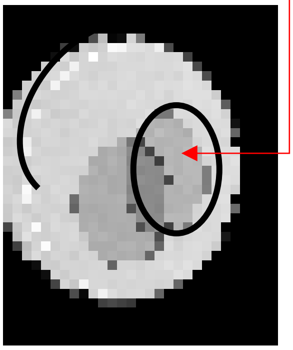

Fig 38. Highlight of folding artifacts in images regularized with Tikhonov regularization

The visual inspection for images regularized with Tikhonov regularization showed that it provided much more homogenous and denoised images inside the body of the phantom than feed forward regularization, but also as regularization was more intense, more folding artifacts started to appear as well, being highlighted in figure 38. Again, no noise was observed outside the body of the phantom thanks to the use of the body coil phantom conventional prior information image from figure 29.

4.2 Graphs & tables for the evaluation of the algorithm with real data

The graphs contained the information for the different measurements taken for the real case of the volunteer's data, being organized by tissue, slice, variable measured (noise, SNR or CNR) and by the λ_1 that was used in the first reconstruction. In total, three graphs were obtained for the same tissue, slice and variable measured: for $\lambda_1= 10^{-3}$, $\lambda_1=10^{-2}$ and $\lambda_1=10^{-1}$.

In those graphs, the horizontal axis contained the regularization factor for the second reconstruction (λ_2) and the vertical axis contained the different variables measured. In blue appear the measurements for the reconstruction without the help of the prior information from the Q-body coil, in orange the measurements for the reconstruction with the conventional prior information from the Q-body coil or first reconstruction, in gray the measurements for the second reconstruction that used a median filtered version of the first reconstruction as alternative prior information and in yellow the measurements for the second reconstruction that used a mean filtered version of the first reconstruction as alternative prior information.

As four noise, SNR and CNR measurements were taken for the same tissue in the same slice and the same regularization factors, the values displayed in the graphs correspond to the average values of those four measurements, while the uncertainties were represented in a separate table. They were not represented in vertical error bars because the values for λ_2 in the horizontal axis were the same for all the reconstruction modalities in the same graph, so the vertical error bars for the different modalities could overlap between them, making difficult to differentiate the error bars for different modalities. The table that has the uncertainty information for each graph is attached to the right of the graph.

Figures 39 to 44 and tables 1 to 6 represent blood, figures 45 to 53 and tables 7 to 15 account for myocardium and figures 54 to 62 and tables 16 to 24 represent skeletal muscle. In each tissue, the graphs and tables from the first page represent noise, the graphs and tables in the second page information account for SNR and in the case of myocardial and skeletal muscle the third page graphs and tables represent the CNR of these tissues with respect to blood. λ_1s are organized in rows: the first row comes with the graph for $\lambda_1=10^{-3}$, the second row accounts for the graph with $\lambda_1=10^{-2}$ and the last row represents the graph for $\lambda_1=10^{-1}$. The comments of every set of graphs for the same measurement and tissue for all the different regularization factors where included in the page after those graphs were displayed.

4.2.1 Blood in cut +7

Noise

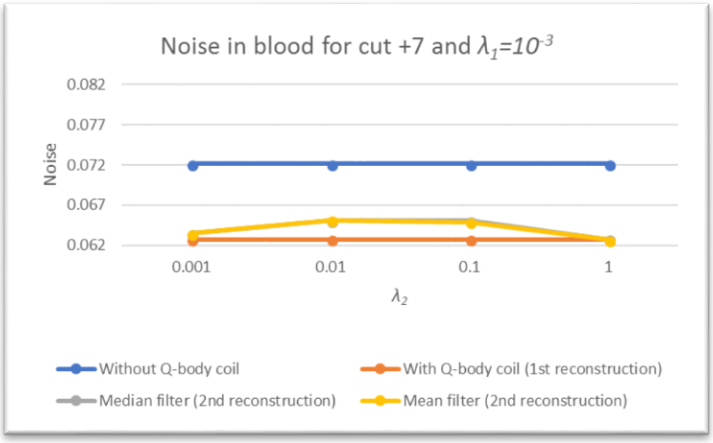

Fig 39. Noise in blood for cut +7 and $\lambda_1=10^{-3}$

Table 1. Standard deviations for noise measurements in blood for cut +7 and $\lambda_1=10^{-3}$

λ_2	Without Q-body coil	With Q-body coil (1st reconstruction)	Median filter (2nd reconstruction)	Mean filter (2nd reconstruction)
10^{-3}	0.013618868	0.017291762	0.017959784	0.017996242
10^{-2}	0.013618868	0.017291762	0.018872869	0.01917767
10^{-1}	0.013618868	0.017291762	0.01728041	0.017084758
1	0.013618868	0.017291762	0.01407791	0.014014894

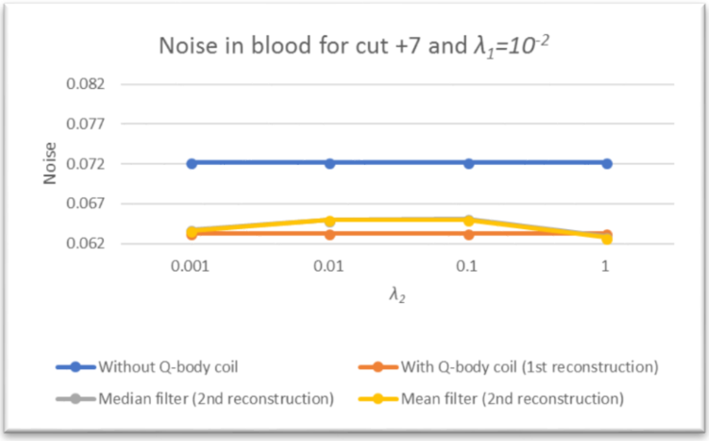

Fig 40. Noise in blood for cut +7 and $\lambda_1=10^{-2}$

Table 2. Standard deviations for noise measurements in blood for cut +7 and $\lambda_1=10^{-2}$

λ_2	Without Q-body coil	With Q-body coil (1st reconstruction)	Median filter (2nd reconstruction)	Mean filter (2nd reconstruction)
10^{-3}	0.011253598	0.018049772	0.018207319	0.018140894
10^{-2}	0.011253598	0.018049772	0.01877843	0.019019999
10^{-1}	0.011253598	0.018049772	0.017321036	0.017255341
1	0.011253598	0.018049772	0.014302479	0.014191505

Table 3. Standard deviations for noise measurements in blood for cut +7 and $\lambda_1=10^{-1}$

λ_2	Without Q-body coil	With Q-body coil (1st reconstruction)	Median filter (2nd reconstruction)	Mean filter (2nd reconstruction)
10^{-3}	0.023427403	0.021189687	0.018174238	0.01813622
10^{-2}	0.023427403	0.021189687	0.017805107	0.017941484
10^{-1}	0.023427403	0.021189687	0.01785026	0.017752018
1	0.023427403	0.021189687	0.016428471	0.015768304

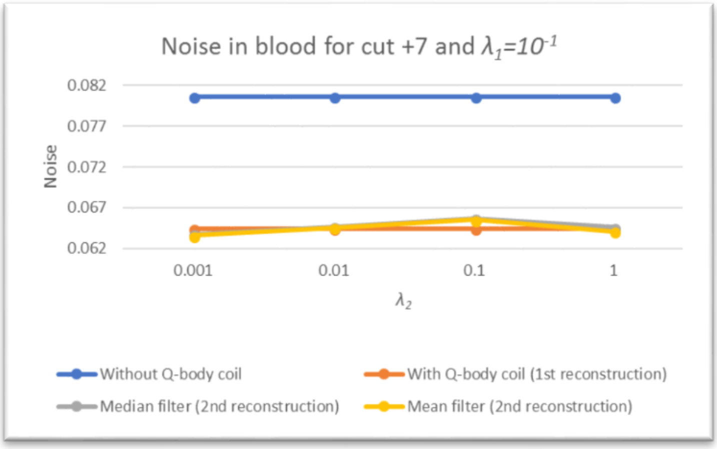

Fig 41. Noise in blood for cut +7 and $\lambda_1=10^{-1}$

Noise in blood took values around 0.07, with an uncertainty lower than 0.02. In this case, noise values used to be quite stable with respect to different regularization factors λ_1 and λ_2, except in the reconstruction without Q-body coil, where the noise was slightly increased with high λ_1s.

Average noise values for the first reconstruction were lower than for the reconstruction without Q-body coil, while second reconstruction noise values used to be quite similar to the first reconstruction noise values, although second reconstruction was a little bit noisier for $\lambda_1=10^{-3}$ and $\lambda_1=10^{-2}$. Second reconstruction noise values for the median and mean filtered cases were almost the same.

With respect to uncertainty values, the uncertainty in the reconstruction without Q-body coil was lower than for the first reconstruction, except when $\lambda_1=10^{-1}$, while the uncertainty for the second reconstruction was also lower than for the first reconstruction, but not so low as the uncertainties for the reconstruction without Q-body coil. As λ_1 was increased, the uncertainties were higher, while as λ_2 was increased, the uncertainties were lower for the second reconstruction. The uncertainty values for both types of second reconstruction were quite similar between each other.

SNR

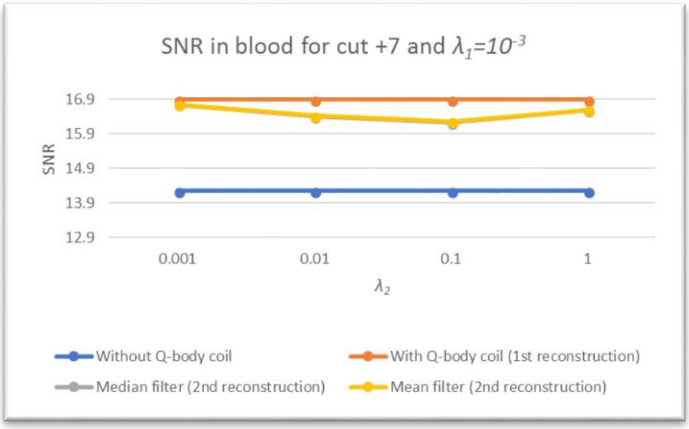

Fig 42. SNR in blood for cut +7 and $\lambda_1=10^{-3}$

Table 4. Standard deviations for SNR measurements in blood for cut +7 and $\lambda_1=10^{-3}$

λ_2	**Without Q-body coil**	**With Q-body coil (1st reconstruction)**	**Median filter (2nd reconstruction)**	**Mean filter (2nd reconstruction)**
10^{-3}	2.695366455	4.595629735	4.691211027	4.701951248
10^{-2}	2.695366455	4.595629735	4.717992407	4.812716784
10^{-1}	2.695366455	4.595629735	4.302899422	4.289275311
1	2.695366455	4.595629735	3.727909191	3.715298609

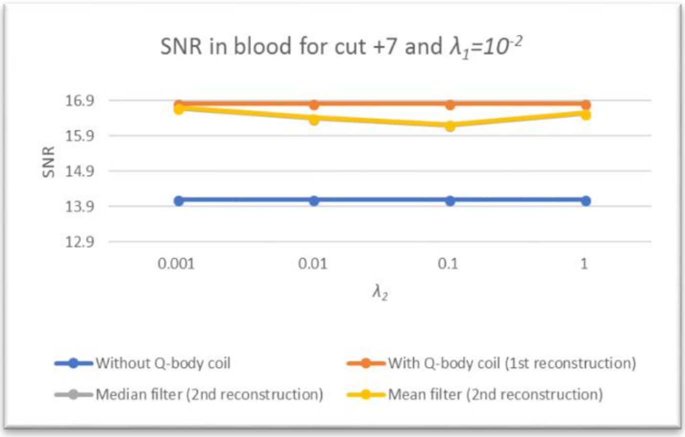

Fig 43. SNR in blood for cut +7 and $\lambda_1=10^{-2}$

Table 5. Standard deviations for SNR measurements in blood for cut +7 and $\lambda_1=10^{-2}$

λ_2	**Without Q-body coil**	**With Q-body coil (1st reconstruction)**	**Median filter (2nd reconstruction)**	**Mean filter (2nd reconstruction)**
10^{-3}	2.206019079	4.795658824	4.744863396	4.74178078
10^{-2}	2.206019079	4.795658824	4.713154566	4.797298511
10^{-1}	2.206019079	4.795658824	4.30788791	4.312567846
1	2.206019079	4.795658824	3.771166098	3.750408656

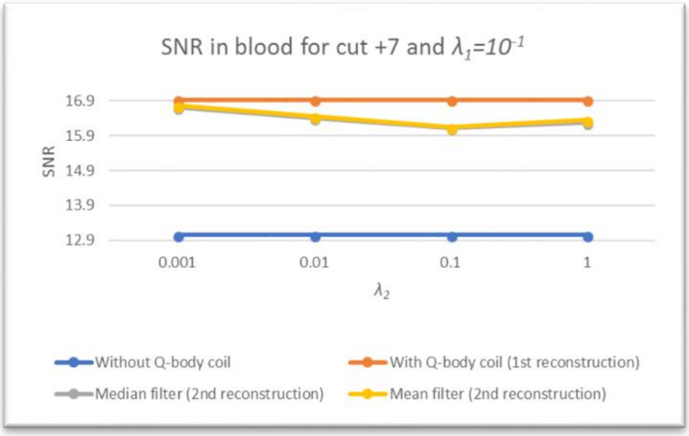

Fig 44. SNR in blood for cut +7 and $\lambda_1=10^{-1}$

Table 6. Standard deviations for SNR measurements in blood for cut +7 and $\lambda_1=10^{-1}$

λ_2	**Without Q-body coil**	**With Q-body coil (1st reconstruction)**	**Median filter (2nd reconstruction)**	**Mean filter (2nd reconstruction)**
10^{-3}	3.005007066	5.716239058	4.765214754	4.796961871
10^{-2}	3.005007066	5.716239058	4.524926675	4.600610281
10^{-1}	3.005007066	5.716239058	4.364523082	4.363824975
1	3.005007066	5.716239058	4.117542685	4.020522623

According to equations 3.6.1 and 3.6.2, SNR was defined as the inverse of noise when noise was normalized by the mean value of the ROI. Consequently, the SNR lines represented in the graphs appeared inverted if compared to the same lines but for noise measurements.

SNR in blood was about 15 while the uncertainties were about 4.5. As happened with noise measurements in blood, SNR measurements were quite stable with respect to λ_1 and λ_2, except for measurements of the reconstruction without Q-body coil, which were worse as λ_1 was increased.

The first reconstruction provided with better values of SNR than the reconstruction without Q-body coil, while the second reconstruction provided a little bit lower SNR values with respect to the first reconstruction. Second reconstruction cases with mean and median filter supplied with identical SNR measurements.

Again, the uncertainty measurements for the reconstruction without Q-body coil were lower than for the first reconstruction, while the uncertainty values for the second reconstruction were quite similar to the measurements from the first reconstruction. In general, the uncertainty values increased as λ_1 was increased while they decreased as λ_2 was increased. The second reconstruction uncertainty values for both types of second reconstruction were similar.

4.2.2 Myocardial muscle in cut -2

Noise

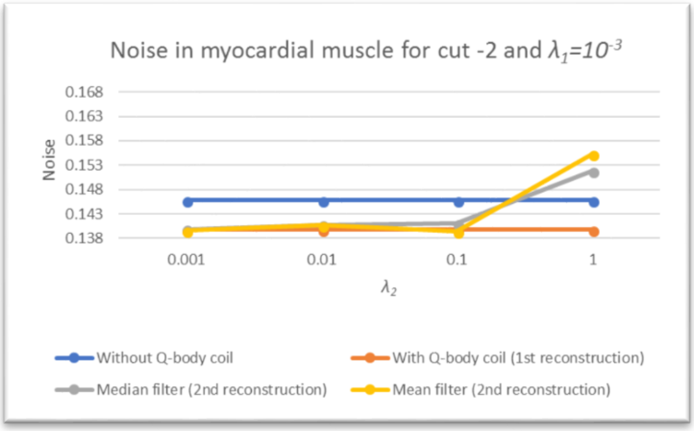

Fig 45. Noise in myocardial muscle for cut -2 and $\lambda_1=10^{-3}$

Table 7. Standard deviations for noise measurements in myocardial muscle for cut -2 and $\lambda_1=10^{-3}$

λ_2	Without Q-body coil	With Q-body coil (1st reconstruction)	Median filter (2nd reconstruction)	Mean filter (2nd reconstruction)
10^{-3}	0.02584885	0.016791168	0.017025102	0.017556755
10^{-2}	0.02584885	0.016791168	0.017083723	0.017582755
10^{-1}	0.02584885	0.016791168	0.018404934	0.021220825
1	0.02584885	0.016791168	0.016374994	0.016308013

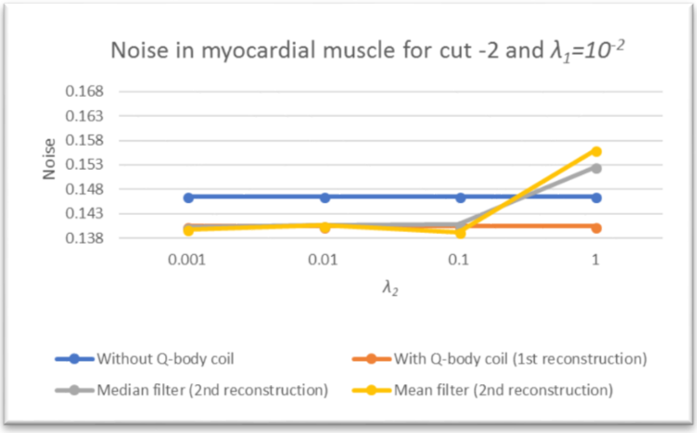

Fig 46. Noise in myocardial muscle for cut -2 and $\lambda_1=10^{-2}$

Table 8. Standard deviations for noise measurements in myocardial muscle for cut -2 and $\lambda_1=10^{-2}$

λ_2	Without Q-body coil	With Q-body coil (1st reconstruction)	Median filter (2nd reconstruction)	Mean filter (2nd reconstruction)
10^{-3}	0.021766324	0.018364224	0.01669302	0.017399464
10^{-2}	0.021766324	0.018364224	0.016908804	0.0173908
10^{-1}	0.021766324	0.018364224	0.018519716	0.021478167
1	0.021766324	0.018364224	0.017229817	0.017154281

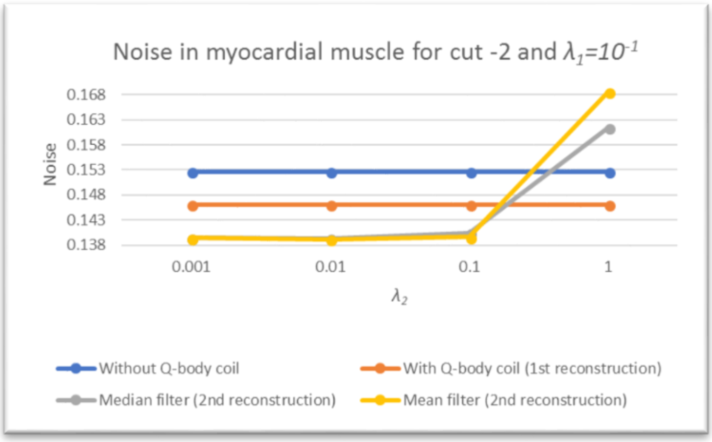

Fig 47. Noise in myocardial muscle for cut -2 and $\lambda_1=10^{-1}$

Table 9. Standard deviations for noise measurements in myocardial muscle for cut -2 and $\lambda_1=10^{-1}$

λ_2	Without Q-body coil	With Q-body coil (1st reconstruction)	Median filter (2nd reconstruction)	Mean filter (2nd reconstruction)
10^{-3}	0.037886215	0.027463585	0.01679831	0.016644709
10^{-2}	0.037886215	0.027463585	0.016726105	0.017375031
10^{-1}	0.037886215	0.027463585	0.021637619	0.025390568
1	0.037886215	0.027463585	0.038383512	0.033561128

Noise in myocardial muscle was around 0.15, being twice noisier than blood, with uncertainty values lower than 0.03, being the uncertainties higher than for blood but not so high if the uncertainties of both tissues were compared to the average values.

The first reconstruction was less noisy than the reconstruction without the prior information from the Q-body coil, while the second reconstruction provided similar values to the ones of the first reconstruction except when λ_1 was high and λ_2 was low, where the second reconstruction was less noisy than the first one and when λ_2 was high, as in this case, noise suddenly increased with the appearance of folding artifacts in this second reconstruction. Noise values for both mean and median filters for the second reconstruction were almost identical, although the second reconstruction with median filter was a little bit less noisy when λ_2 was high. Noise values in both the first reconstruction and the reconstruction without Q-body coil were increased with λ_1.

Uncertainty values for the first reconstruction were lower than for the reconstruction without prior information for the body coil (unlike what happened in blood), while uncertainty values for the second reconstruction were a little bit higher or a little bit lower than the ones of the first reconstruction, but always being similar to the values provided by first reconstruction. In general, uncertainty values increased as λ_1 and λ_2 were increased (unlike what happened in blood, where uncertainties decreased when λ_2 was increased). The uncertainty values for both types of second reconstruction were similar between each other.

SNR

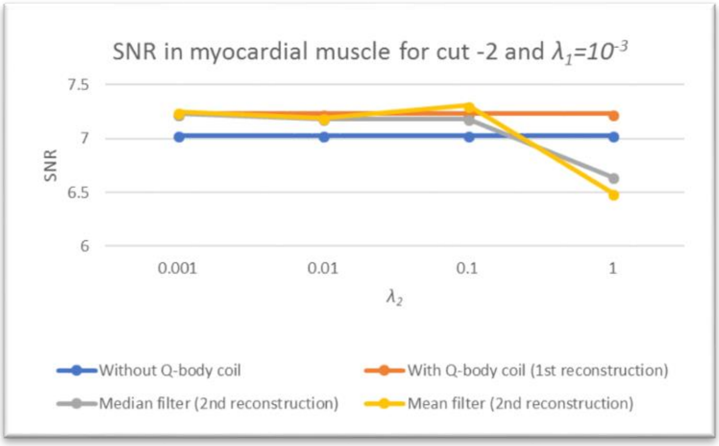

Fig 48. SNR in myocardial muscle for cut -2 and $\lambda_1=10^{-3}$

Table 10. Standard deviations for SNR measurements in myocardial muscle for cut -2 and $\lambda_1=10^{-3}$

λ_2	Without Q-body coil	With Q-body coil (1st reconstruction)	Median filter (2nd reconstruction)	Mean filter (2nd reconstruction)
10^{-3}	1.287959118	0.851003559	0.872535153	0.903923009
10^{-2}	1.287959118	0.851003559	0.880833623	0.917332606
10^{-1}	1.287959118	0.851003559	0.955118371	1.169230101
1	1.287959118	0.851003559	0.704016953	0.683148682

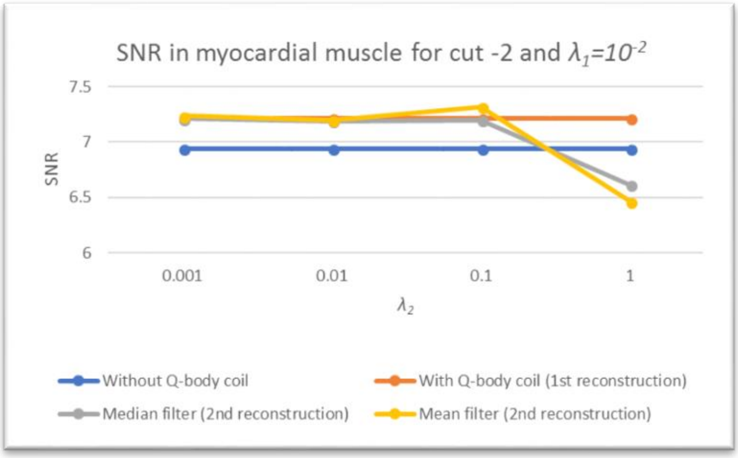

Fig 49. SNR in myocardial muscle for cut -2 and $\lambda_1=10^{-2}$

Table 11. Standard deviations for SNR measurements in myocardial muscle for cut -2 and $\lambda_1=10^{-2}$

λ_2	Without Q-body coil	With Q-body coil (1st reconstruction)	Median filter (2nd reconstruction)	Mean filter (2nd reconstruction)
10^{-3}	1.022403769	0.936663463	0.857824106	0.893918135
10^{-2}	1.022403769	0.936663463	0.872295	0.908403589
10^{-1}	1.022403769	0.936663463	0.96620522	1.188127843
1	1.022403769	0.936663463	0.727597734	0.709203373

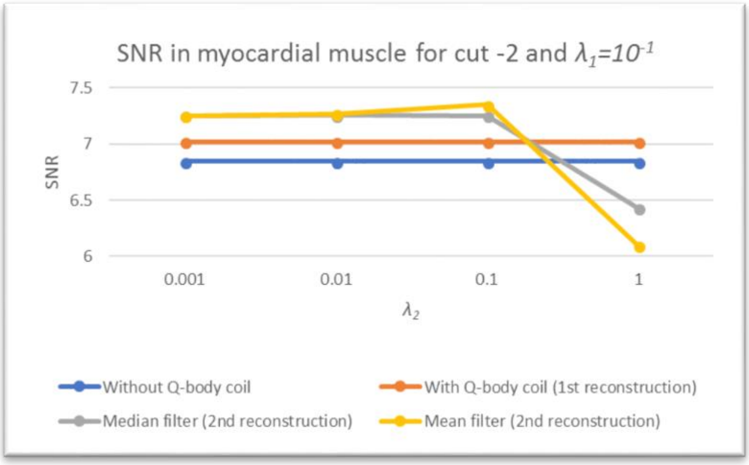

Fig 50. SNR in myocardial muscle for cut -2 and $\lambda_1=10^{-1}$

Table 12. Standard deviations for SNR measurements in myocardial muscle for cut -2 and $\lambda_1=10^{-1}$

λ_2	Without Q-body coil	With Q-body coil (1st reconstruction)	Median filter (2nd reconstruction)	Mean filter (2nd reconstruction)
10^{-3}	1.610666844	1.250114792	0.864454709	0.856626401
10^{-2}	1.610666844	1.250114792	0.870755535	0.908171886
10^{-1}	1.610666844	1.250114792	1.151061423	1.399888224
1	1.610666844	1.250114792	1.328160987	1.110520236

As happened in blood, SNR measurements were the inverse measurements to noise, yielding inverse lines in the graphs.

In myocardial muscle, SNR was about 7, being about a half of the SNR of blood, as myocardium was a darker tissue with a weaker signal. As the average value of the SNR in myocardial muscle was lower than the mean value in blood, uncertainties were also lower, taking values lower than 1.5, yielding similar variations if both the uncertainties for blood and for myocardium were divided by their average value.

SNR in the first reconstruction was higher than in the reconstruction without Q-body coil, while SNR in the second reconstruction was similar to the values provided by the first reconstruction, except when $\lambda_1=10^{-1}$, where the second reconstruction provided higher SNR values, and when $\lambda_2=10^{-1}$, where the second reconstruction provided lower SNR values than first reconstruction and that even the reconstruction without Q-body coil. The second reconstruction SNR values for the mean filter and for the median filter were quite similar, although the median filter values were a little bit better for high λ_2s.

Uncertainty values for the first reconstruction were lower than for the reconstruction without the *a priori* information from the Q-body coil. For low λ_1s the uncertainties for the second reconstruction were higher than for the first reconstruction, while for high λ_1s, the uncertainty values for the second reconstruction were lower than for the first reconstruction. Uncertainties used to increase as λ_1 was increased while they used to decrease as λ_2 was decreased in the second reconstruction. The uncertainty values for both types of second reconstruction were almost identical between each other.

CNR between blood and myocardial muscle for cut -2

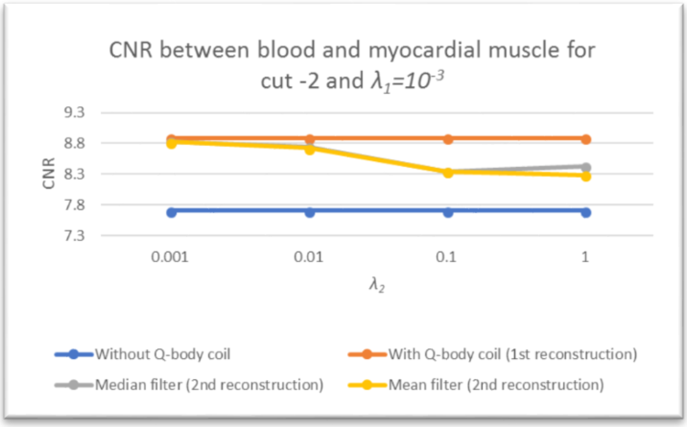

Fig 51. CNR between blood and myocardial muscle for cut -2 and $\lambda_1=10^{-3}$

Table 13. Standard deviations for CNR measurements between blood and myocardial muscle for cut -2 and $\lambda_1=10^{-3}$

λ_2	**Without Q-body coil**	**With Q-body coil (1st reconstruction)**	**Median filter (2nd reconstruction)**	**Mean filter (2nd reconstruction)**
10^{-3}	2.236585647	1.946165016	1.969292108	1.884604685
10^{-2}	2.236585647	1.946165016	2.016119499	1.943050285
10^{-1}	2.236585647	1.946165016	1.916759503	1.877114928
1	2.236585647	1.946165016	2.639752084	2.519913011

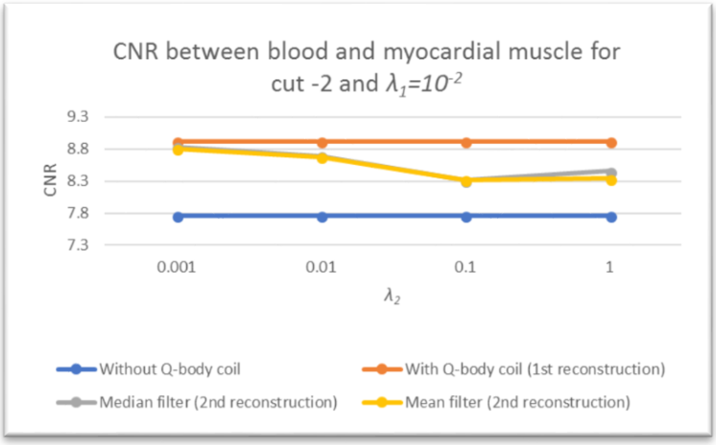

Fig 52. CNR between blood and myocardial muscle for cut -2 and $\lambda_1=10^{-2}$

Table 14. Standard deviations for CNR measurements between blood and myocardial muscle for cut -2 and $\lambda_1=10^{-2}$

λ_2	**Without Q-body coil**	**With Q-body coil (1st reconstruction)**	**Median filter (2nd reconstruction)**	**Mean filter (2nd reconstruction)**
10^{-3}	2.06214302	1.9631127	1.962892015	1.854297251
10^{-2}	2.06214302	1.9631127	1.986555878	1.918172496
10^{-1}	2.06214302	1.9631127	1.915259809	1.879393025
1	2.06214302	1.9631127	2.505850993	2.526702456

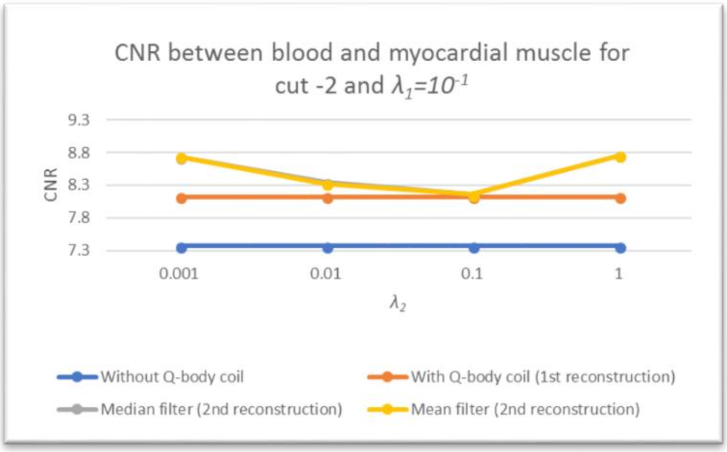

Fig 53. CNR between blood and myocardial muscle for cut -2 and $\lambda_1=10^{-1}$

Table 15. Standard deviations for CNR measurements between blood and myocardial muscle for cut -2 and $\lambda_1=10^{-1}$

λ_2	**Without Q-body coil**	**With Q-body coil (1st reconstruction)**	**Median filter (2nd reconstruction)**	**Mean filter (2nd reconstruction)**
10^{-3}	0.759408173	1.731640335	1.878011726	1.817443192
10^{-2}	0.759408173	1.731640335	1.92090798	1.878558793
10^{-1}	0.759408173	1.731640335	1.921627126	1.878981335
1	0.759408173	1.731640335	2.71046234	2.589880176

Unlike noise and SNR measurements, which were performed on one tissue, CNR measurements had to be performed between two tissues. As blood was the reference tissue, CNR was only measured in myocardial muscle and skeletal muscle with respect to blood.

CNR between blood and myocardial muscle was about 8.5, while its uncertainty values were around 2.

The CNR values were higher in first reconstruction than in the reconstruction without the Q-body coil information. For the second reconstruction, they were slightly lower than in the first reconstruction when λ_1 was low, but they were higher than in the first reconstruction for $\lambda_2=10^{-1}$. Both types of second reconstruction with median and mean filter supplied with almost identical CNR values. In first reconstruction and reconstruction without Q-body coil, CNR values decreased as λ_1 was increased.

The uncertainty values were lower in the first reconstruction than in the reconstruction without Q-body coil, while in the second reconstruction the uncertainty values were similar to the first reconstruction, being sometimes a little bit lower and other times a little bit higher. The uncertainty values for both types of second reconstruction were quite similar between each other. Uncertainties decreased with λ_1 and increased with λ_2, unlike what happened in all the previous measurements.

4.2.3 Skeletal muscle (pectoralis) in cut +3 for noise and SNR and in cut +7 for CNR

Noise for cut +3

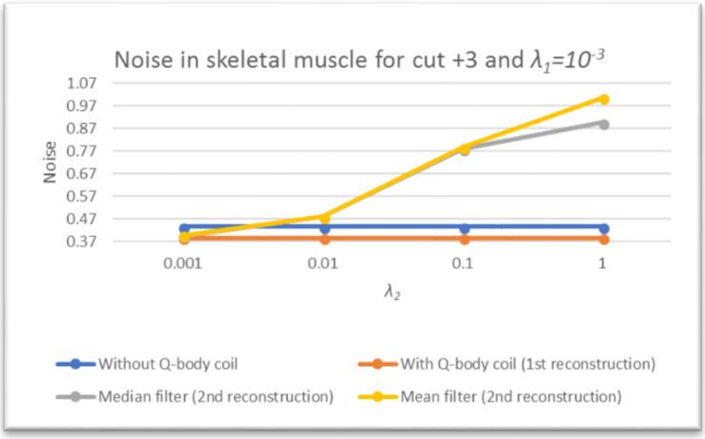

Fig 54. Noise in skeletal muscle for cut +3 and $\lambda_1=10^{-3}$

Table 16. Standard deviations for noise measurements in skeletal muscle for cut -2 and $\lambda_1=10^{-3}$

λ₂	**Without Q-body coil**	**With Q-body coil (1st reconstruction)**	**Median filter (2nd reconstruction)**	**Mean filter (2nd reconstruction)**
10^{-3}	0.12402438	0.078687603	0.085142832	0.079621998
10^{-2}	0.12402438	0.078687603	0.150984999	0.111016063
10^{-1}	0.12402438	0.078687603	0.340211753	0.234160279
1	0.12402438	0.078687603	0.440678563	0.439579109

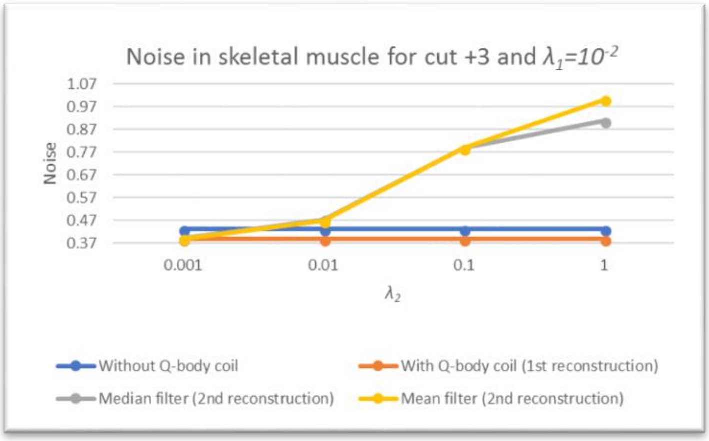

Fig 55. Noise in skeletal muscle for cut +3 and $\lambda_1=10^{-2}$

Table 17. Standard deviations for noise measurements in skeletal muscle for cut +3 and $\lambda_1=10^{-2}$

λ₂	**Without Q-body coil**	**With Q-body coil (1st reconstruction)**	**Median filter (2nd reconstruction)**	**Mean filter (2nd reconstruction)**
10^{-3}	0.127207812	0.094492671	0.086186796	0.075308883
10^{-2}	0.127207812	0.094492671	0.156480151	0.116421494
10^{-1}	0.127207812	0.094492671	0.370970198	0.295830956
1	0.127207812	0.094492671	0.474362802	0.511950444

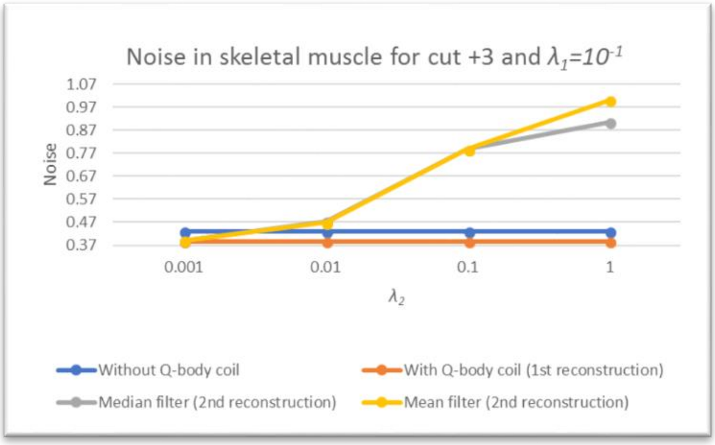

Fig 56. Noise in skeletal muscle for cut +3 and $\lambda_1=10^{-1}$

Table 18. Standard deviations for noise measurements in skeletal muscle for cut +3 and $\lambda_1=10^{-1}$

λ₂	**Without Q-body coil**	**With Q-body coil (1st reconstruction)**	**Median filter (2nd reconstruction)**	**Mean filter (2nd reconstruction)**
10^{-3}	0.123295302	0.127676541	0.090079663	0.088462797
10^{-2}	0.123295302	0.127676541	0.155498316	0.157037918
10^{-1}	0.123295302	0.127676541	0.448603048	0.519911036
1	0.123295302	0.127676541	0.529330381	0.730083835

Noise values for skeletal muscle were very variable, between 0.35 and more than 1, being by far the noisiest tissue of the three, with many distortions, specially when the regularization factors were high enough and introduced folding artifacts in the images. Noise values larger than 1 indicated that the standard deviation of the ROI was higher than the mean, so the skeletal muscle provided very chaotic signals under extreme regularization, especially in the second reconstruction.

Noise was lower in the first reconstruction than in the reconstruction without Q-body coil prior information, while the second reconstruction was much noisier than the first reconstruction and even than the reconstruction without Q-body coil, especially when λ_2 was high. First reconstruction and reconstruction without Q-body coil values were stable with λ_1. Noise values for both types of second reconstruction were similar, except under high λ_2s, where noise values for the median filter were slightly better than for the mean filter.

Uncertainties were lower in the first reconstruction than in the reconstruction without Q-body coil, while uncertainties for the second reconstruction were much higher than for the first reconstruction, in general. Uncertainty values used to increase with λ_1 and λ_2. Uncertainties were a little bit lower for the second reconstruction with median filter than with mean filter, especially when λ_2 was high.

SNR for cut +3

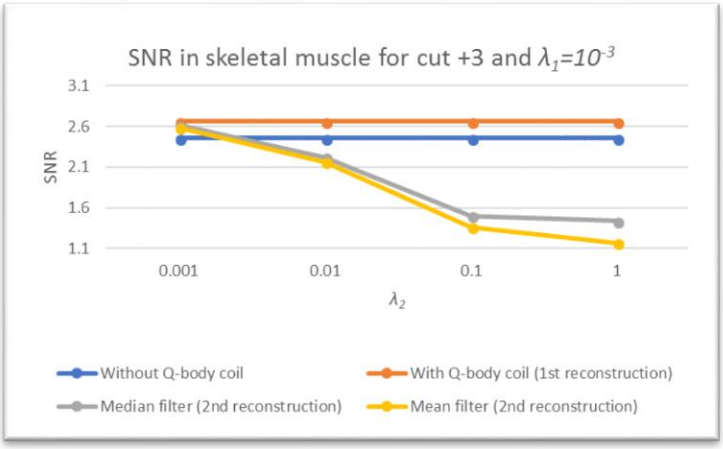

Fig 57. SNR in skeletal muscle for cut +7 and $\lambda_1=10^{-3}$

Table 19. Standard deviations for SNR measurements in skeletal muscle for cut +3 and $\lambda_1=10^{-3}$

λ_2	Without Q-body coil	With Q-body coil (1st reconstruction)	Median filter (2nd reconstruction)	Mean filter (2nd reconstruction)
10^{-3}	0.761026717	0.490535834	0.513941858	0.490197746
10^{-2}	0.761026717	0.490535834	0.585534017	0.470132825
10^{-1}	0.761026717	0.490535834	0.680687563	0.427310314
1	0.761026717	0.490535834	0.935010106	0.564271412

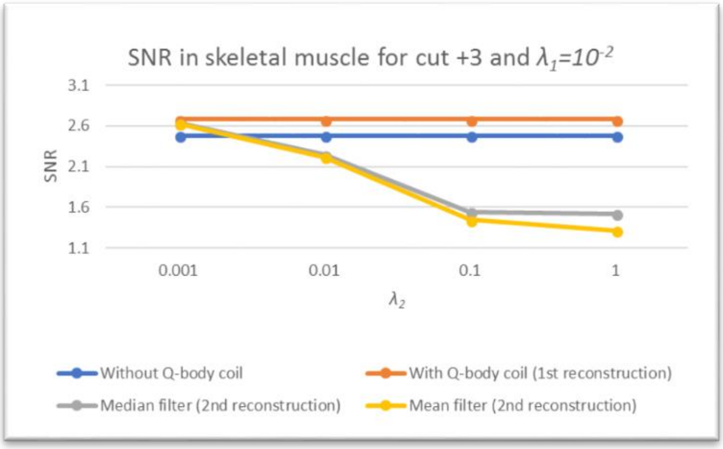

Fig 58. SNR in skeletal muscle for cut +7 and $\lambda_1=10^{-2}$

Table 20. Standard deviations for SNR measurements in skeletal muscle for cut +3 and $\lambda_1=10^{-2}$

λ_2	Without Q-body coil	With Q-body coil (1st reconstruction)	Median filter (2nd reconstruction)	Mean filter (2nd reconstruction)
10^{-3}	0.753348347	0.541388825	0.514492399	0.466344552
10^{-2}	0.753348347	0.541388825	0.579774297	0.452180584
10^{-1}	0.753348347	0.541388825	0.800702069	0.651618678
1	0.753348347	0.541388825	1.148740593	0.905358438

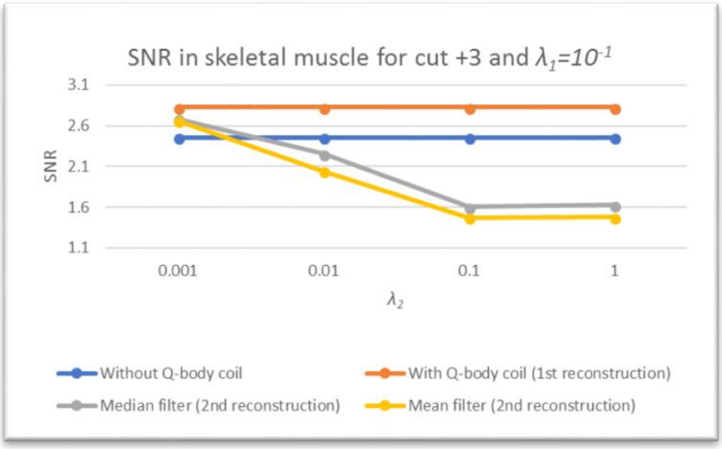

Fig 59. SNR in skeletal muscle for cut +7 and $\lambda_1=10^{-1}$

Table 21. Standard deviations for SNR measurements in skeletal muscle for cut +3 and $\lambda_1=10^{-1}$

λ_2	Without Q-body coil	With Q-body coil (1st reconstruction)	Median filter (2nd reconstruction)	Mean filter (2nd reconstruction)
10^{-3}	0.795452094	1.227872427	0.538964219	0.51868966
10^{-2}	0.795452094	1.227872427	0.606677471	0.642353818
10^{-1}	0.795452094	1.227872427	1.0538124	1.078785932
1	0.795452094	1.227872427	1.466340635	1.443021129

As happened in blood and myocardial muscle, SNR values were the inverse ones to the noise values, yielding inverse lines in the graphs.

SNR values in skeletal muscle were very variable, ranging from 2.5 to less than 1 in second reconstruction with extreme regularization, where values were highly chaotic. Therefore, it was a weaker signal tissue than blood and myocardial muscle, being highly dominated by noise.

SNR values in the first reconstruction were better than in the reconstruction without Q-body coil, while in the second reconstruction they were much lower than in the first reconstruction, as λ_2 was higher. The second reconstruction with median filter provided slightly better values than the reconstruction with mean filter, especially at high λ_2s. First reconstruction and reconstruction without Q-body coil were quite stable with respect to λ_1.

Uncertainty values of the first reconstruction were lower than for the reconstruction without Q-body coil images, except for $\lambda_1=10^{-1}$, where they were higher. Second reconstruction uncertainty values were higher than in the first reconstruction. In general, the uncertainties for both types of second reconstruction were quite similar between them. Uncertainties increased with the λ_1 and λ_2 applied.

CNR between blood and skeletal muscle for cut +7

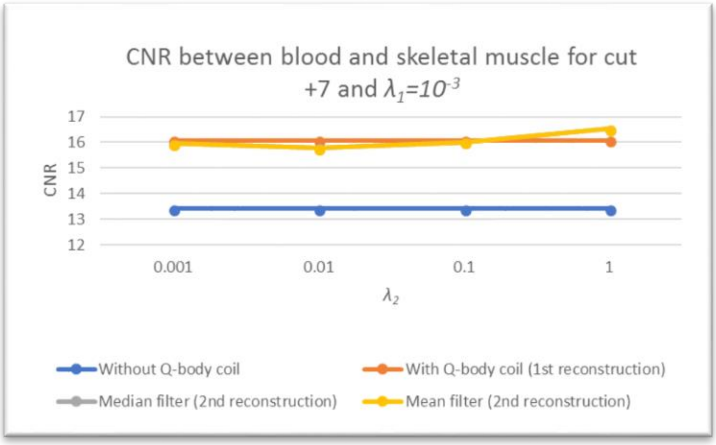

Fig 60. CNR between blood and skeletal muscle for cut +7 and $\lambda_1=10^{-3}$

Table 22. Standard deviations for CNR measurements between blood and skeletal muscle for cut +7 and $\lambda_1=10^{-3}$

λ_2	Without Q-body coil	With Q-body coil (1st reconstruction)	Median filter (2nd reconstruction)	Mean filter (2nd reconstruction)
10^{-3}	2.689994831	4.512871306	4.600814143	4.605349885
10^{-2}	2.689994831	4.512871306	4.651874503	4.714984251
10^{-1}	2.689994831	4.512871306	4.315829682	4.27525806
1	2.689994831	4.512871306	3.74489435	3.726021994

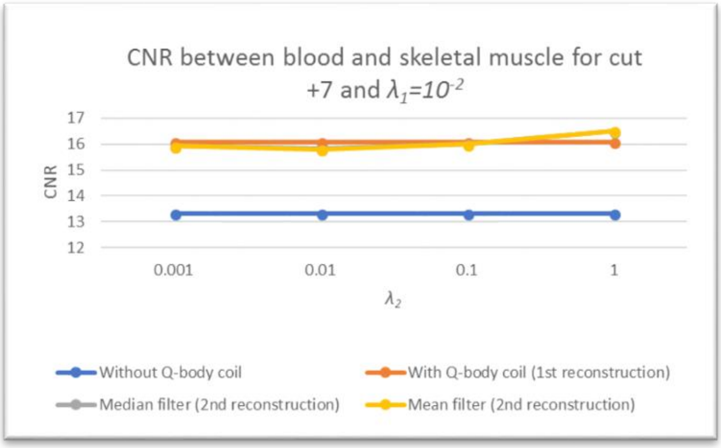

Fig 61. CNR between blood and skeletal muscle for cut +7 and $\lambda_1=10^{-2}$

Table 23. Standard deviations for CNR measurements between blood and skeletal muscle for cut +7 and $\lambda_1=10^{-2}$

λ_2	Without Q-body coil	With Q-body coil (1st reconstruction)	Median filter (2nd reconstruction)	Mean filter (2nd reconstruction)
10^{-3}	2.240920281	4.727446985	4.651131049	4.641628329
10^{-2}	2.240920281	4.727446985	4.651517682	4.701422185
10^{-1}	2.240920281	4.727446985	4.323226227	4.299133278
1	2.240920281	4.727446985	3.787687303	3.760291512

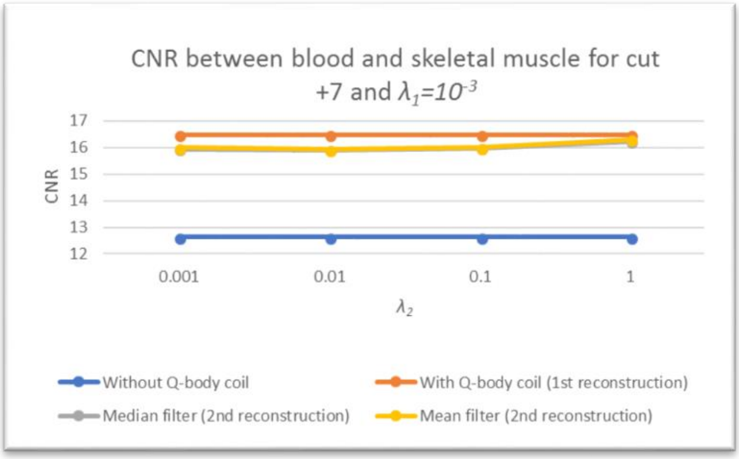

Fig 62. CNR between blood and skeletal muscle for cut +7 and $\lambda_1=10^{-1}$

Table 24. Standard deviations for CNR measurements between blood and skeletal muscle for cut +7 and $\lambda_1=10^{-1}$

λ_2	Without Q-body coil	With Q-body coil (1st reconstruction)	Median filter (2nd reconstruction)	Mean filter (2nd reconstruction)
10^{-3}	3.116189596	5.755329909	4.678587422	4.695416732
10^{-2}	3.116189596	5.755329909	4.499652816	4.527941685
10^{-1}	3.116189596	5.755329909	4.384635237	4.358413771
1	3.116189596	5.755329909	4.130636643	4.026448746

The CNR values between blood and skeletal muscle were around 15, since blood was the most powerful tissue with the highest SNR and skeletal muscle was the weakest tissue with the lowest SNR, being the CNR between blood and skeletal muscle almost twice than between blood and myocardium.

The CNR values were higher in the first reconstruction than in the reconstruction without Q-body coil while in the second reconstruction, the values were quite similar to the first reconstruction, being slightly lower when $\lambda_1=10^{-1}$. In general, all the values for all the reconstruction were stable with respect to the λs applied.

Uncertainty values for the first reconstruction were higher than for the reconstruction without Q-body coil, unlike what happens in the CNR values between blood and myocardial muscle, while in the second reconstruction they were similar to the uncertainty values in the first reconstruction. Uncertainty values used to increase with λ_1 while they used to decrease with λ_2, in general. Uncertainties for both types of second reconstruction were quite similar.

4.3 Visualization of real case images for the evaluation of the algorithm

Some of the reconstructed images were displayed to study also the algorithm from a visual point of view. All the images correspond to the intermediate axial (first column), coronal (second column) or sagittal (third column in the next page) views of the four reconstruction modalities that were tested. The columns represent the different perpendicular views, while the rows represent the reconstruction modality: the first row accounts for the reconstruction [38] without Q-body coil, the second row represents the reconstruction with Q-body coil or first reconstruction, the third row deals with the second reconstruction with median filter and the last row accounts for the second reconstruction with mean filter.

Even if a visual criterion is not enough in the field of Image Processing, as it may be subjective, it is very important to be tested, because the final purpose of an image is to be visually assessed by a clinician. It can happen that mathematically an image has better values of SNR and CNR, but visually these changes may be difficult to be appreciated, so a visual inspection had to be carried out in the thesis.

Figures 63 to 74 represent the different reconstructed volumes, while figures 75 to 83 account for the different images that have been used as priors: the conventional Q-body coil image and the median[51] and mean[61] filtered versions of the first reconstruction that were used as alternative prior information images in the proposed algorithm.

Axial views

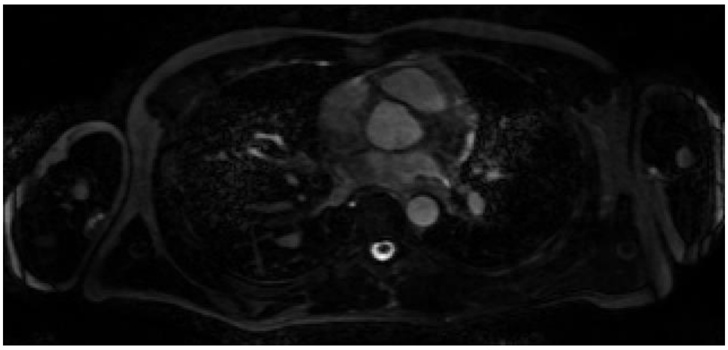

Fig 63. Middle axial slice reconstructed without the help of the Q-body coil images for $\lambda_1=10^{-1}$

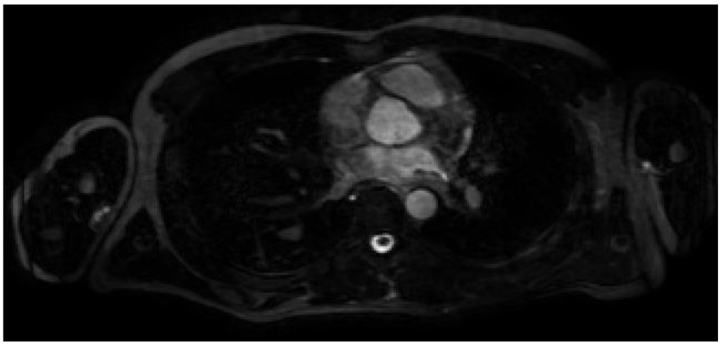

Fig 64. Middle axial slice reconstructed with the help of the Q-body coil images (first reconstruction) for $\lambda_1=10^{-1}$

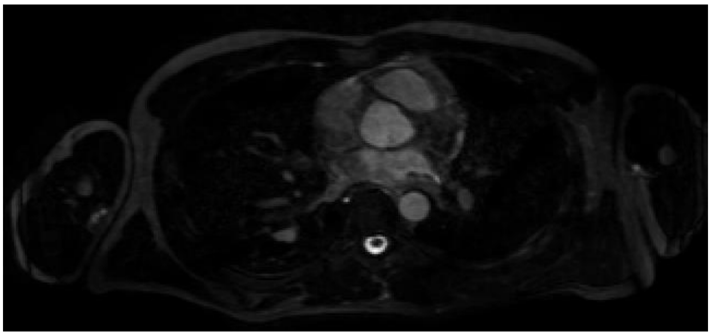

Fig 65. Middle axial slice reconstructed with the help of the median filtered first reconstruction (second reconstruction) for $\lambda_1=10^{-1}$ and $\lambda_2=10^{-2}$

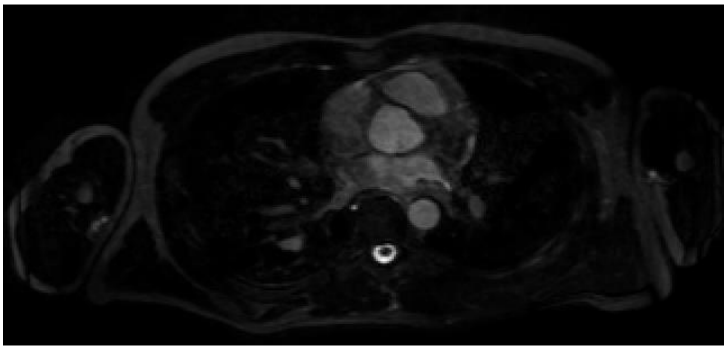

Fig 66. Middle axial slice reconstructed with the help of the mean filtered first reconstruction (second reconstruction) for $\lambda_1=10^{-1}$ and $\lambda_2=10^{-2}$

Coronal views

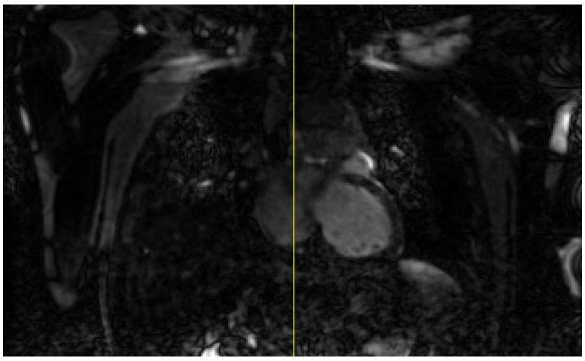

Fig 67. Middle coronal slice reconstructed without the help of the Q-body coil images for $\lambda_1=10^{-1}$

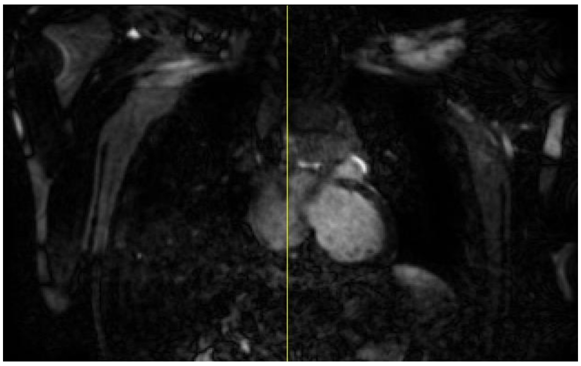

Fig 68. Middle coronal slice reconstructed with the help of the Q-body coil images (first reconstruction) for $\lambda_1=10^{-1}$

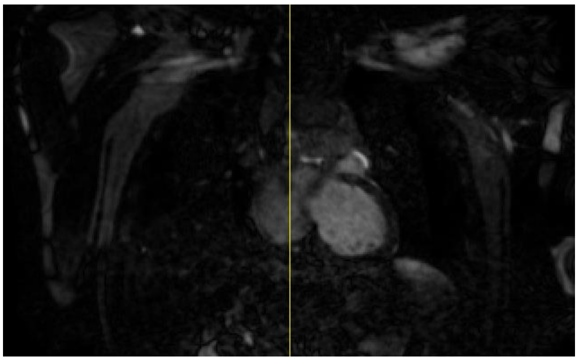

Fig 69. Middle coronal slice reconstructed with the help of the median filtered first reconstruction (second reconstruction) for $\lambda_1=10^{-1}$ and $\lambda_2=10^{-2}$

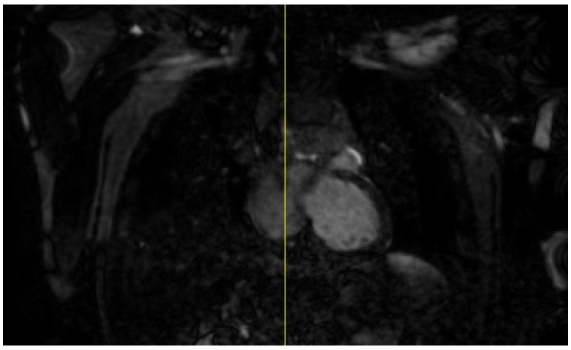

Fig 70. Middle coronal slice reconstructed with the help of the mean filtered first reconstruction (second reconstruction) for $\lambda_1=10^{-1}$ and $\lambda_2=10^{-2}$

Sagittal views

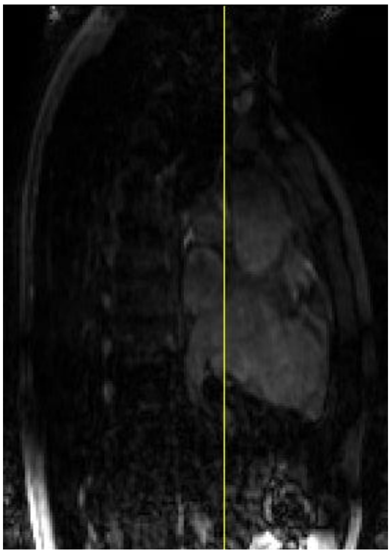

Fig 71. Middle sagittal slice reconstructed without the help of the Q-body coil images for $\lambda_1=10^{-1}$

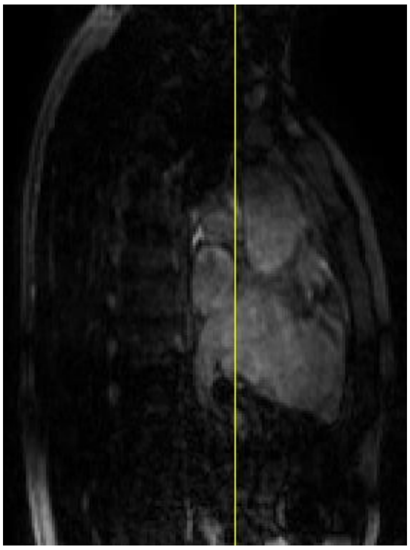

Fig 72. Middle sagittal slice reconstructed with the help of the Q-body coil images (first reconstruction) for $\lambda_1=10^{-1}$

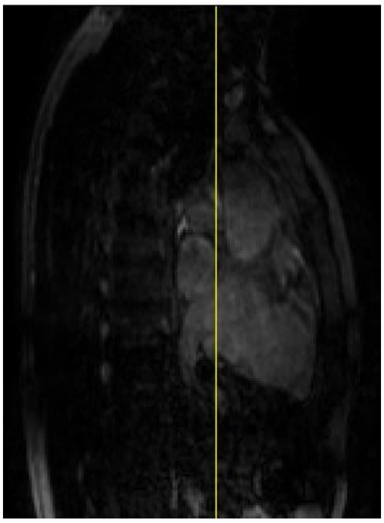

Fig 73. Middle sagittal slice reconstructed with the help of the median filtered first reconstruction (second reconstruction) for $\lambda_1=10^{-1}$ and $\lambda_2=10^{-2}$

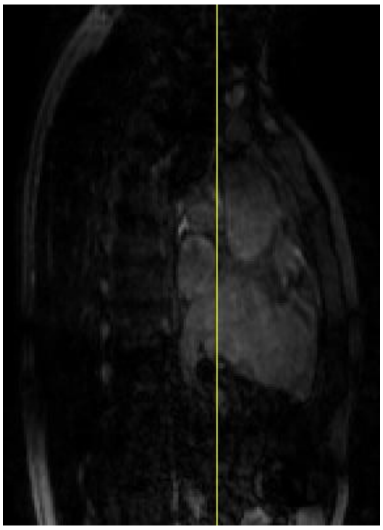

Fig 74. Middle sagittal slice reconstructed with the help of the mean filtered first reconstruction (second reconstruction) for $\lambda_1=10^{-1}$ and $\lambda_2=10^{-2}$

The **reconstruction without Q-body coil** (figures 63, 67 and 71) did a good job in unfolding the different aliased voxels, but in doing so, it also introduced many noise in the image. In the axial view was difficult to be observed, but in the coronal and sagittal views, the level of noise was so high below the heart that organs inferior to the heart were difficult to be observed (liver, stomach…), losing many information from those organs and tissues. The volume contained some folding artifacts[40], as some distortions in the form of repetitions could be observed in the different images if a very detailed observation was carried out.

Many advantages can be observed when **reconstructing with the Q-body coil** (figures 64, 68 and 72). Visually, the volume seemed to be less noisy[41] than in the reconstruction without Q-body coil, confirming the noise reduction stated by the graphs. Consequently, not so many information had been lost, allowing to appreciate a little bit better some abdominal organs (but not too much better). However, the image contained some folding artifacts and it was a little bit noisy, but not so much as in the reconstruction without Q-body coil images.

The **second reconstructions obtained by median filtering** (figures 65, 69 and 73) or **mean filtering** (figures 66, 70 and 74) were slightly less noisy and with better details than the first reconstruction especially in those areas where the first reconstruction contained folding artifacts while the second reconstruction did not contain artifacts. In zones where both reconstructions did not contain any artifact, their quality was very similar. Therefore, the details in the abdominal area could be visualized better than in the first reconstruction images, being slightly enhanced. Both types of second reconstruction images were quite similar between them, with very slight changes.

Visualization of prior information images

Axial views

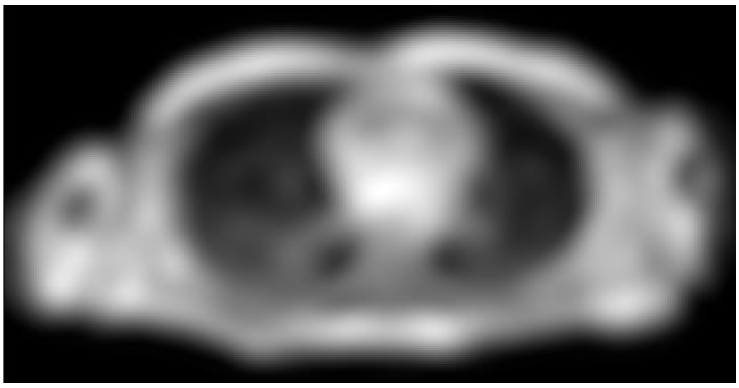

Fig 75. Middle axial slice of the Q-body coil images

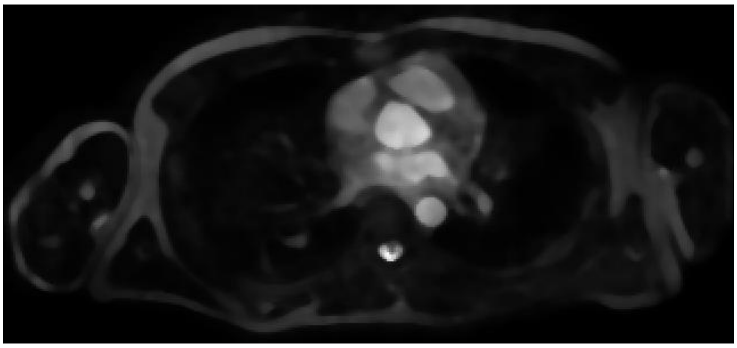

Fig 76. Middle axial slice of the median filtered first reconstruction for $\lambda_1=10^{-1}$

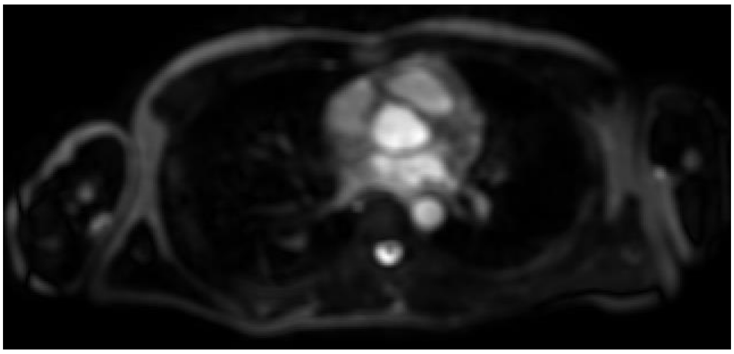

Fig 77. Middle axial slice of the mean filtered first reconstruction for $\lambda_1=10^{-1}$

Coronal views

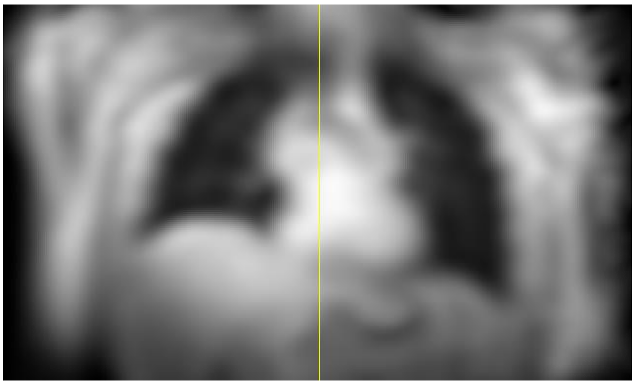

Fig 78. Middle coronal slice of the Q-body coil images

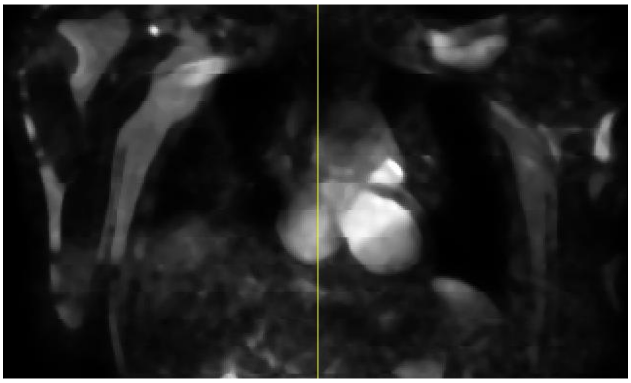

Fig 79. Middle coronal slice of the median filtered first reconstruction for $\lambda_1=10^{-1}$

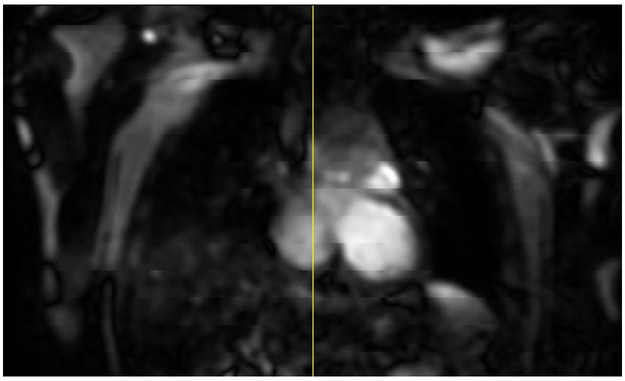

Fig 80. Middle coronal slice of the mean filtered first reconstruction for $\lambda_1=10^{-1}$

Sagittal views

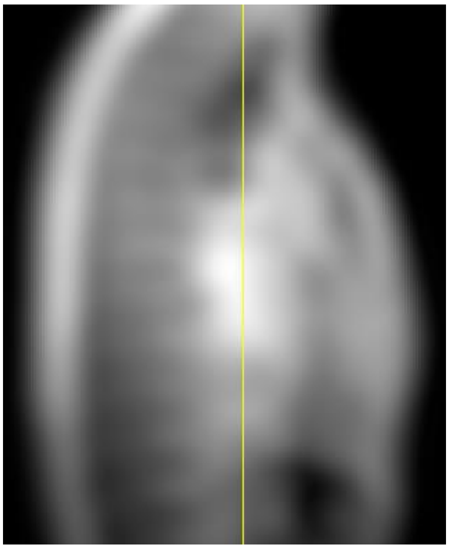

Fig 81. Middle sagittal slice of the Q-body coil images

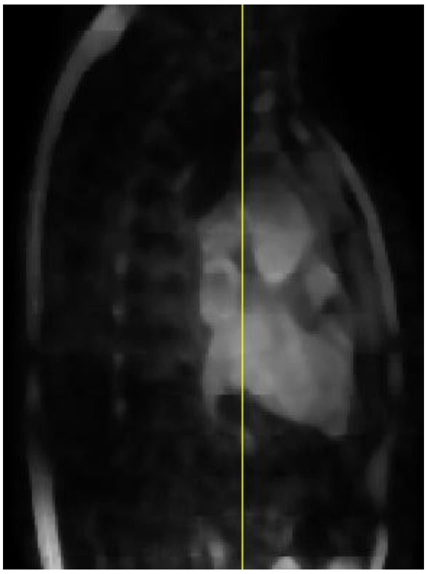

Fig 82. Middle sagittal slice of the median filtered first reconstruction for $\lambda_1=10^{-1}$

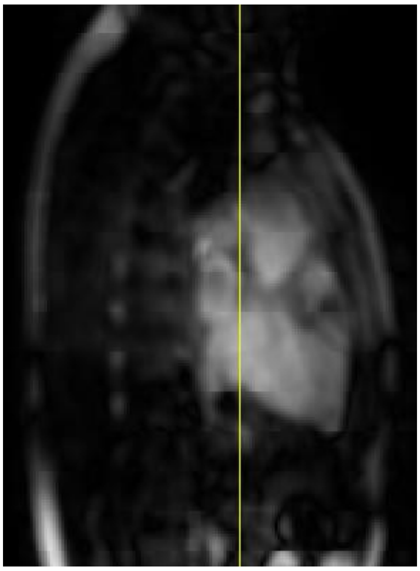

Fig 83. Middle sagittal slice of the median filtered first reconstruction for $\lambda_1=10^{-1}$

The conventional prior information **images of the original Q-body coil** in figures 75, 78 and 81 used in the first reconstruction confirmed the hypothesis stated in the Introduction section: they provided a very crude and homogeneous estimate of the patient. As it can be observed, the Q-body coil images had a very low spatial resolution, so fine details could not be detected and only very "evident" organs as for instance the heart and the lungs could be distinguished. Furthermore, the images had a very low contrast resolution with very few gray levels to be displayed in the image, in such a way that the Q-body coil images seemed to be made just of pure black and pure white intensities, with no intermediate intensities.

Unlike the original Q-body coil image, the alternative prior information images used for the second reconstruction, which were the **median** (figures 76, 79 and 82) **and mean** (figures 77, 80 and 83) **filtered versions of the first reconstruction**, contained an alternative amount of prior information for the second reconstruction, with a higher spatial resolution than the standard Q-body coil image, so that more organs apart from the lungs and the heart could be distinguished. Contrast resolution was also higher, as more intermediate gray levels between pure black and pure white could be distinguished. The mean filtered version was blurrier than the median filtered version, with more homogenous organs and tissues but less edges and punctual details, what could reduce the information transmitted by these images filtered with this mean filter.

5. DISCUSSION & FINAL CONCLUSIONS

5.1 Phantom results

The initial SENSE reconstruction implemented in IDL™ and tested in the phantom without any regularization nor prior information showed that the SENSE algorithm was effective for unfolding images which were down-sampled in the k-space and presented aliasing. However, it amplified noise, reducing SNR as stated by equation 1.3.13. Therefore, the level of Gaussian noise that was intentionally introduced in the phantom was multiplicated if a pure SENSE reconstruction without any regularization nor prior information was used, by assessing the reconstructed image with a visual criterion.

When the simulated body coil image for the phantom was applied, it set to zero the noise outside the body of the phantom, as it was a mask with zeros in the outside, avoiding that noise from the exterior propagated into the interior of the phantom. With respect to feed forward and Tikhonov regularization, Tikhonov seemed to be visually better for denoising, yielding much more homogenous images. This may have happened because Tikhonov regularization applied the same regularization criterion for all the voxels to unfold, as the regularization matrix applied is λI (see equation 1.3.2.1), while feed forward regularization matrix applied a different regularization factor for each voxel to unfold, being proportional to the square of the voxels of the body coil image in the coordinates of the voxels to unfold (see equation 1.3.1.1).

Tikhonov regularization was also more flexible than feed forward regularization, allowing a wider range of orders of magnitude for regularization to remove noise before the introducing artifacts (from 10^{-8} to almost 1, while in feed forward the range went from 1 to 100). This happened because the λ used in feed forward regularization had to multiply the square values of the Q-body coil image (see equation 1.3.1.1), producing more intense changes in the regularized image than the λ used in Tikhonov, which was just multiplied by the ones of the identity matrix (see equation 1.3.2.1), not producing so intense changes.

If the regularization factors were too high, some folding artifacts started to appear in both regularization methods, as consequence of a more intense deviation from the original SENSE reconstruction, reducing its unfolding effectivity. However, Tikhonov could be applied with more orders of magnitude before folding artifacts appeared while feed forward regularization introduced artifacts with many less orders of magnitude.

Consequently, as Tikhonov regularization was a more effective and flexible method in denoising that allowed a wider range of orders of magnitude for regularization and that was also simpler than the methods searched in the bibliography (see point 1.3.4), it was the regularization method implemented inside the two reconstructions of the proposed algorithm with the real case images.

5.2 Algorithm evaluation results

From the Results that have been provided in the previous section in the algorithm evaluation, many derivations can be carried out.

As blood was the main tissue of interest in the “bright-blood” SSFP sequence, it was the brightest tissue in the image, being also the less noisy one. It was also the one with the highest SNR and the one with the lowest uncertainties when compared to the average values measured. This happened because the final goal of coronary MRA was to keep a high difference in signal between blood and the rest of the tissues, so the SNR measured in blood had to be as high as possible. Noise, SNR and CNR values in blood had low uncertainties with respect to their average values, since the sequence used in the thesis was very focused in providing very stable values for blood, having a main region of interest in the image which was the heart.

In this region of interest, the sequence devoted more time and calculations to get a good quality image, while out of this region, the values were reconstructed much faster, so they became noisier, as they were not so important for the quality of the image. What was more, as tissues were further from the heart, contrast was also reduced, as the efficiency for fat suppression in zones far away from the heart was reduced as well.

Myocardial muscle offered lower image values than blood, as its signal was weaker. Consequently, it was a darker tissue in the image, with a higher dominance of noise that provided higher uncertainties with respect to the mean value of the tissue. However, as myocardium was located in the main region of interest for the image, the heart, its values were not very noisy nor disturbed in comparison to the tissues that were further from the heart. Due to the “bright blood” sequence, its CNR values with respect to blood were high while its SNR was much lower, so that a high quality image with a good contrast could be obtained.

Skeletal muscle was the tissue with more distortions and higher uncertainties in comparison to the average values it offered from the three tissues that were measured. It was also the noisiest tissue with the lowest SNR and the tissue with the highest CNR with respect to blood. All these things happened for two reasons. Firstly, because its signal was very weak, being weaker than the one of myocardial muscle and much weaker than the one of blood, in order to offer a good contrast in the image and having a minimum SNR and a maximum CNR with respect to blood. As the signal in skeletal muscle was so low, the dominance of noise in skeletal muscle was very evident, both in a mathematical and in a visual assessment. The second reason why the tissue measurements were distorted was because they were further from the region of interest, unlike myocardial muscle and blood. Therefore, as its appearance in the image was not so crucial, the sequence was not interested in spending too much time and other resources in getting the signal from this tissue, focusing more on the heart, and therefore not caring so much if more noise was introduced in skeletal muscle.

Unlike what was expected in theory, larger regularization factors increased noise instead of decreasing it. When using regularization factors lower than $\lambda=10^{-2}$, measurements were approximately stable, and noise, SNR and CNR average values and their uncertainties were almost fixed; but when regularization factors for both reconstructions were higher than 10^{-2}, noise started to increase while SNR and CNR started to decrease. All the reconstruction modalities were sensitive to these distortions, but the second reconstruction was more sensible than the others, as with high values of λ_2, it got destabilized very easily. All those distortions happened due to the appearance of folding artifacts [40] , as when more regularization was applied, the regularized images were reconstructed in a more and more deviated trend from the original SENSE reconstruction [38] , reducing the ability of the SENSE algorithm to unfold the aliased voxels.

The presence of artifacts in the image made that true image voxels overlapped with those folding artifacts, causing many variations in the different image tissues, especially in those ones that were not so important for the image and were further from the heart, as could be skeletal muscle, increasing noise, decreasing SNR and CNR and making some areas of the image brighter than they should be due to this overlapping of folding artifacts over true image values. That was why noise, SNR and CNR values were so much destabilized when too intense regularization factors where applied, in such a way that regularization factors higher than 1 were never used in the thesis.

The real case images displayed in the Results section were displayed with the highest regularization factors before too much folding artifacts started to appear, so for that reason the images could contain some more folding artifacts than usual but that still did not distort too much image quality. If the images had been displayed with less intense regularization factors, not so many folding artifacts would have been observed and the reconstructions for the different modalities would have been more similar between them.

The reconstruction without Q-body coil image was obtained without any prior information, being Tikhonov regularization with truncated SVD methods the only ways in which they were denoised. For that reason, those images were very noisy and with low values for SNR and CNR. As stated in the Results section, such a high quantity of noise made almost impossible to differentiate some details in the images, especially details far away from the main area of interest, as could be abdominal organs. At that moment, one does understand the importance of the Q-body coil images used as conventional prior information for SENSE reconstruction, because otherwise, many information is lost during the reconstruction process and among the information that is not lost, many of it cannot be retrieved as the image is too noisy. Due to the intense regularization that was applied in the displayed images, the volume contained some folding artifacts, as there were brighter areas of the image where the folding artifacts overlapped with the original values of the image.

Unlike the reconstruction without Q-body coil, the first reconstruction did make use of the conventional prior information of the Q-body coil images, allowing for noise reduction and SNR and CNR increase, so that areas far away from the heart could be distinguished better than in the reconstruction without Q-body coil. Again, as the regularization factor selected for denoising was quite high, some folding artifacts appeared in the image (they did not distort the image too much, but they were there), making also some zones of the image brighter than they should have been due to their overlapping with true image voxels.

The second reconstruction images were reconstructed with an alternative level of prior information than the first reconstruction, using as prior image the mean or median filtered versions of the first reconstruction. However, they did not offer more denoised results than the first reconstruction, so it seemed that for the algorithm it was the same to obtain the reconstruction with conventional prior information from the Q-body coil than from a more detailed first reconstruction. When the regularization factors were low they provided similar values to the first reconstruction, but when the regularization factors were high, the second reconstruction values used to destabilize very easily, much more easily than the values from the other modalities, being too sensitive to the appearance of folding artifacts.

This high sensibility to folding artifacts in the second reconstruction happened because the second reconstruction did depend on the first reconstruction, as it used it as alternative prior information. If too high λ_1s were used in the first reconstruction, the artifacts in these reconstruction could expand to the second reconstruction and if a λ_2 high enough was used, too, the artifacts that expanded from the first to the second reconstruction would add up to the extra artifacts that would appear in the second reconstruction, distorting noise, SNR and CNR more than in the first reconstruction. In the images displayed, the first regularization factor was intense but the regularization factor for the second reconstruction was a little bit lower (a λ_1 of 10^{-1} and a λ_2 of 10^{-2}), so the appearance of artifacts was attenuated in the second reconstruction with those regularization values, so that the image quality in the second reconstruction was a little bit enhanced in those areas that in the first reconstruction were having artifacts. If lower regularization factors had been used, not so many folding artifacts would have appeared and the images would have been more similar.

In both mathematical and visual terms, both types of second reconstruction offered quite similar results, although the reconstruction with median filter provided slightly better results than the one with mean filter under situations of extreme regularization. This happened due to the fact that median filtering avoided that outliers affected the reconstruction, not smoothing so much the image when filtering in the edges and allowing to keep alternative prior details for the second reconstruction that could attenuate the increase of noise and the decrease of SNR and CNR when many folding artifacts started to appear. The mean filtering was unable to keep so many edges, providing a more homogenous image with less detailed information. However, even if the median filter was slightly better than the mean filter for the second reconstruction, the values provided by this median filter were quite similar to those ones of the first reconstruction and under extreme regularization with λ_2 they were even worse than those ones of the first reconstruction.

Nevertheless, the difference with which the second reconstruction with median filter values were better than the second reconstruction with mean filter was not very significant. Therefore, it could be said that the use of the low pass filter did not affect the second reconstruction images and the mean and median filter could be used indistinctively to obtain the alternative prior information images for the second reconstruction.

The conventional prior information of the Q-body coil images was crude and homogenous, with very similar values among different tissues and with a low spatial resolution, so that very few organs and tissues could be recognized. Even though, the enhancement in the noise, SNR and CNR values if the first reconstruction results were compared to the reconstruction without Q-body coil results was notorious, so the changes caused going from no prior information to crude prior information was very important and enhanced a lot image quality.

The level of prior information details introduced by the mean and median filtered versions of the first reconstruction for the final reconstruction was higher than the one introduced by the Q-body coil images. As stated three paragraphs above, the median filter was able to keep more detailed information in the than the mean filter, as it did not blur the edges of the first reconstruction as much as the mean filter did, since the median filter was more resistant to outliers. Maybe some noise propagation could have happened from the first to the second reconstruction because the kernel size was not effective, although it was highly improbable to have happened.

The fact that in the filtered first reconstruction images all the tissues except for blood were attenuated was the main motivation of seeing whether a use of alternative prior information from the first reconstruction did enhance SENSE-reconstructed images. In that way, regularization in attenuated tissues would be reduced while regularization in blood would be enhanced, trying to denoise more than with the conventional level of prior information supplied by Q-body coil images. However, as it was stated some paragraphs above, even if an alternative level of prior information was introduced, the second reconstruction results were quite similar to the ones of the first reconstruction, and they could be even worse under too intense regularization conditions, so the algorithm did not really take advantage of this alternative prior information and for the algorithm it was almost the same if a conventional Q-body coil image was used as prior than if a filtered first reconstruction was used as prior.

The SSFP sequence used for obtaining the coronary MRA images was being carried out in an extreme, in such a way that the contrast obtained was the maximum one that this sequence could generate, making pointless to test the algorithm in other cases, since the proposed algorithm was independent from the patient’s geometry and only relied on the sequence conditions. So as the sequence was used in its extremes, measurements could only be the same or worse than in the case that was tested in this thesis. In no other case the measurements would be better, making pointless to try to test the algorithm in other patients or volunteers, as results would not be enhanced in any way. If the opposite case had happened and the results provided had been better than current methods, the algorithm would have been tested in other patients and volunteers to really make sure that it would work.

5.3 Final conclusions

The final conclusions that can be derived from all the work that has been carried out are:

- Tikhonov regularization with truncated SVD was a much simpler regularization method for SENSE reconstruction denoising than the ones reviewed in the bibliography and a much more effective and flexible method than other proposed methods that could have been implemented (as feed forward regularization).

- The MR sequence focused in keeping a main region of interest in the image: the heart, in order to study it in high detail. Inside the heart, tissues as blood and myocardial muscle were highly stable, with few noise, as they were acquired more slowly and in more detail. In the meanwhile, tissues out of the heart (*pectoralis* skeletal muscle) were more distorted and noisier, being acquired faster and with less detail and contrast, as the efficiency for fat suppression in those regions was lower.

- The sequence was a “bright-blood” coronary MRA, so blood was the most intense tissue and the most stabilized tissue of all, with a lower level of noise and a higher SNR than the rest of the tissues, establishing very high values of CNR[31] between it and the rest of the tissues (myocardium, skeletal muscle...).

- Too intense Tikhonov regularization with truncated SVD introduced many folding artifacts that overlapped with the actual image voxels, increasing the standard deviation of these regions. These artifacts left zones with no artifacts and zones affected by artifacts with much higher values due to this overlapping, causing the distortion of noise, SNR and CNR values. Noise suddenly increased while SNR and CNR dramatically decreased under those conditions.

- Even if the conventional prior information that the Q-body coil images supplied to the reconstruction with Q-body coil was crude and homogenous, the results for the reconstruction using its information as prior were much better than the results for the reconstruction that did not use the Q-body coil images as a source of prior information, setting an important breakthrough in SENSE reconstruction denoising.

- Although alternative prior information (attenuated tissues in coronary MRA) with more details than Q-body coil images was introduced in the second reconstruction, the algorithm was unable to take advantage of that alternative prior information. This happened because the noise, SNR and CNR results in this reconstruction were quite similar to the values for the first reconstruction. Furthermore, second reconstruction results were even worse than first reconstruction results in extreme regularization cases. Consequently, for the proposed algorithm it was the same if crude and homogenous information from the Q-body coil was provided than if more detailed alternative information from a low pass filtered pre-reconstructed image was provided, being unable to identify and work with this alternative quantity of *a priori* information.

- The second reconstruction with the alternative level of prior information was more sensible to the appearance of folding artifacts with high levels of λ_1 and λ_2, but especially with high regularization levels for λ_2, in such a way that the second reconstructed image presented artifacts that expanded from the first reconstruction due to a high λ_1, and artifacts from its own reconstruction, due to a high λ_2. Consequently, as so many artifacts were present, under extreme regularization; noise, SNR and CNR values got destabilized.

- The second reconstruction with median filter provided slightly better results under intense regularization than the same reconstruction with mean filter, as median filtering did not remove so much details from the first reconstruction edges and helped to provide more detailed alternative *a priori* information that attenuated distortions caused by too many folding artifacts. However, the values of the second reconstruction with median filter kept being similar to the first reconstruction values or even worse in conditions of too intense regularization, since the only prior information that the algorithms take advantage of is the conventional Q-body coil prior information.

- Consequently, it was pointless to follow with a method that needed two reconstructions to be performed and that consumed more time and computations than other methods if almost no denoising and no visual enhancement was performed with respect to state-of-the-art methods.

6. FUTURE WORK

Even if the algorithm failed to meet the objective of reducing noise and enhancing SNR and CNR by receiving an alternative level of *a* priori information, the thesis has not been useless at all, helping to find alternative ways to reduce this current level of noise by other methods that could be tested in the future.

Alternative future algorithms could be based in the methods for SENSE reconstruction denoising presented in point 1.3.4 (automatic or g-factor based Tikhonov, TV, Bregman or WT-based methods for regularization). Moreover, machine learning and deep learning are becoming fashionable options in equipment with high computational speed, so they could also be explored in the future for denoising images and performing other image processing techniques [66] . Post-processing adaptive filtering can also be tested, but the only drawback of this type of filters is that they have to be applied after all the data have been acquired, so this algorithm would have nothing to do with enhancing image acquisition quality [67] . Fast algorithms looking for image denoising based on MRI sparsity (MRI values tend to be concentrated and not very spread, with a low entropy [68]) can also be a good option, being this last option closely related to WT regularization [57] .

It could also happen that under other conditions the algorithm would work, so it could be tested in coronary MRA with different types of filters and with different kernel sizes [51], [61] for preparing the prior information from the first reconstruction. The algorithm can also be tested in other combinations of SENSE factors [38] to see if the algorithm could be more effective for more noisy and faster reconstructions acquired with higher SENSE factors, according to equation 1.3.13.

The algorithm could also be tested in other MRI applications in other areas of the body where other tissues are highly attenuated for different purposes, in order to see if in those cases the algorithm could take advantage of alternative prior information, too. Maybe it was just tested in the wrong place and under the wrong conditions.

7. SOCIOECONOMIC ANALYSIS

From the socioeconomic point of view, the new algorithm would only generate costs during its development, as the algorithm developer should be paid for getting the documentation on the state-of-the-art methods for SENSE reconstruction denoising, deciding which method could be the best for being the basis of the new algorithm, designing how the algorithm would work, implementing it and testing it on a real case while comparing its results to current methods to determine whether it reduces noise or not in comparison with existing algorithms with alternative prior information.

Together with the author, two engineers helping him and supervising the development process also need to be paid. Furthermore, some other resources need a previous investment, as can be the computer where to design the algorithm and the software used for implementing the algorithm and testing it and indirect costs as can be Internet connection, electricity or transport. All these costs will be presented later in a budget.

With respect to the techniques currently used to study the coronary trunk, where the algorithm is developed, the standard is not set by coronary MRA but by coronary Computer Tomography Angiography (from now on, CTA) [69] , although the facts presented in the following table may favor MRA to substitute CTA as the standard modality for angiography. [26], [69]

Table 25. CTA vs MRA

	ADVANTAGES	DISADVANTAGES
CTA	1. Cheaper 2. Good image quality 3. Fast 4. Simpler equipment	1. Ionizing radiation → legal restrictions[1] 2. Contrast media [70] → Expensive, contraindications... 3. May need invasive procedures (catheterization [71]) 4. Always produce images with the same trend of intensities → No adaptability
MRA	1. No ionizing radiation 2. Good image quality 3. No compulsory contrast media → many modern sequences for non-contrast MRA → reduce costs and the method is less invasive 4. Intensity trends change with the sequence applied → adaptability	1. Expensive 2. Complex equipment 3. Slow, however many methods for speeding acquisition. 4. If contrast media is used [32] → Expensive, contraindications

---

[1] Legislation annex: Real Decreto 783/2001 de 6 de julio (BOE núm. 178 de 26 de julio de 2001)

Consequently, the fact that MRA obtains very good quality adaptable images without ionizing radiation nor contrast media with less invasive means may help MRA to substitute CTA as the standard for angiography in the future. Some of the barriers still avoiding this are the MR scan cost and complexity as well as its long acquisition time, although right now more and more techniques are being developed to speed up acquisition and reduce MRI cost and complexity, so once these barriers have been overcome, MRA will be the future standard for angiography.

7.1 Costs of the project

The total work performed will be divided in stages in order to understand all the costs in an easier way and to know the time and the cost dedicated per stage.

1) Documentation:

1.1 Understanding the basics of MRI, the process of SENSE reconstruction together and the existing regularization methods and their alternatives. **40 HOURS**

1.2 Installing IDL™ in a virtual machine and learning to program in IDL™. **30 HOURS**

2) Development of the project:

2.1 Developing the code for SENSE reconstruction and the different regularization processes applied in the phantom. **40 HOURS**

2.2 Developing the code for the reconstruction and the regularization with the new algorithm in the real case. The time spent solving problems in the code and obtaining the real data is also included. **150 HOURS**

2.3 Taking measurements standard deviation and mean values of the ROIs in ImageJ™ and saving them in Microsoft Excel™. **30 HOURS**

2.4 Computing the noise[41], SNR[43] and CNR[31] values of the ROIs in Microsoft Excel™ and showing the results in graphs. **40 HOURS**

3) Writing the memory:

3.1 Writing the main core of the memory. **70 HOURS**

3.2 Performing corrections in the memory. **30 HOURS**

4) Periodic revisions with the tutors during the whole project. **30 HOURS**

Table 26. Hours dedicated to the project

TASK	HOURS
Documentation	70
Development of the project	260
Writing the memory	100
Revisions with the tutors	30
TOTAL	**460**

Material costs

Material costs can be divided into perishable and inventorial costs.

Perishable costs were those ones that are just consumed for the development of the thesis, as can be subscriptions to databases and websites for the documentation process and the licenses of that software that was not free: IDL™ and Microsoft Office™.

The total cost of the subscription of all universities from Madrid to databases and websites is of €20 million [72] . Taking into account that there are 300000 university students in Madrid [73], the cost of access for each of them is of €70.

An IDL™ license used for implementing the new algorithm costs €200, while a Microsoft Office™ university license for working in Excel™ with the measurements, working in Word™ writing the thesis and working in PowerPoint™ to prepare the presentation costs €80.

Table 27. Table of perishable costs

MATERIAL	PERISHABLE COST
Subscription to databases, websites...	€70 scaled for all the users of the subscription
IDL™ license	€90
Microsoft Office ™ official license	€80
TOTAL	**€240**

The rest of the costs were inventorial costs, which correspond to products or goods that are consumed for more issues apart from preparing the thesis. In this group would just be included the computer where the different steps of the thesis were carried out. for an amortization period of five years and an initial cost of €1100, the computer would cost €220 every year, but as the thesis has been developed in 460 hours, which are 28% of the total working hours of a year (1600 hours), the cost that the computer has been for the thesis is of 0.28·€220= €60.

Table 28. Table of inventorial costs

MATERIAL	INVENTORIAL COST IN AN AMORTIZATION PERIOD OF 5 YEARS	INVENTORIAL COST (SCALED FOR 450 HOURS, 28% OF THE TOTAL WORKING HOURS OF A YEAR)
Computer	€1100	€60
TOTAL	**€1100**	**€60**

The total material cost was depicted as the sum of both perishable and inventorial costs:

Table 29. Table of total material costs

MATERIAL COST TYPE	MATERIAL COST
Perishable costs	€240
Inventorial costs	€60
TOTAL	**€300**

Service costs

The MR scan performed on the volunteer to obtain the raw data was classified as a service cost. The cost of this MR scan was €200. [74]

Table 30. Service costs dedicated to the project

SERVICE	COST
MR scan	€200
TOTAL	**€200**

Personnel costs

Apart from the student that performed the project, the Philips™ clinical scientist working in CNIC and a professor from Universidad Carlos III de Madrid (UC3M) working in Hospital Gregorio Marañón (HGUGM) also reviewed the thesis. The total amount of hours spent by them was around 45 hours, 20 hours by the Philips™ clinical scientist and 5 hours by the professor from Universidad Carlos III de Madrid. Furthermore, the money that a volunteer can be paid for obtaining the raw data for the thesis has to be taken into account, too, being of €500. [75]

Table 31. Personnel costs dedicated to the project

OCCUPATION	HOURS	PRICE/HOUR	PRICE
Project Manager 1 (Philips™ clinical scientist in CNIC)	50	€50/hour	€2500
Project Manager 2 (Professor from Universidad Carlos III de Madrid and researcher in Hospital Gregorio Marañón)	5	€50/hour	€250
Student	450	€20/hour	€9000
Volunteer for the MR scan			€500
TOTAL	**475**		**€12250**

Direct costs

The sum of material, service and direct costs yields the direct costs.

Table 32. Direct costs dedicated to the project

COST TYPE	COST
Material costs	€300
Service costs	€200
Personnel costs	€12250
DIRECT COSTS	**€12750**

Total costs

The total cost will be computed as the sum of direct costs together with an extra 20% that comes from indirect costs (electricity, Internet connection...).

Table 33. Total costs dedicated to the project (without taxes)

COST TYPE	COST
Direct costs	€12750
Indirect costs	0.2·12750€ = €2550
TOTAL COSTS (without taxes)	**€15300**

All the costs have been estimated without taxes, so the table with the total costs will only contain the total cost without taxes. To those costs, a certain percentage higher than 20% should be added for the taxes, approximately.

8. REGULATORY FRAMEWORK

The study was performed in accordance with the Declaration of Helsinki (2000)[2]. All subjects involved in this study provided written informed consent with study approval from the Institutional Review Board.

The algorithm presented in the thesis, as well as the thesis itself, is protected by a Creative Commons license, allowing the free access of anybody to the thesis and its contents. The thesis can be freely downloaded from the Internet without having to pay anything, but the author of the thesis has to be cited and the thesis cannot be modified. [76]

The part of the thesis that presents more legal restrictions is the obtention of data from human volunteers, which is in Spain is regulated by law 14/2007 of 3rd July on Biomedical Research.[3] With respect to this thesis, the following restrictions according to this law had to be applied:

- Every person volunteering in a certain study has to be informed with all the procedures he or she is going to undertake. This information has to be the clearest possible for the volunteer, and if this volunteer is not autonomous by himself or herself, it will be a legal representative the one who will be informed.
- The consent given by a participant of the study could be cancelled whenever the volunteer wants.
- Research has to be of quality and with equality and equity of opportunities for the volunteers taking part in research.
- The fulfilment of these previous points will be watched out by an unbiased Bioethics Committee.
- If any of these points is not fulfilled, there could be a legal punishment, which, depending on how these points have been violated, could suppose in fines from €600 up to €1000000.

MRI does not work with ionizing radiation, but some regulatory and security rules have to be followed to prevent accidents. [77] There is a variety of norms from ASTM (American Society for Testing and Materials), like ASTM F2052 [78] or ASTM F2213 [79] , and from ISO (International Standard Organization), like ISO/TS 10974 [80] regulating all these security issues.

- It is forbidden to enter the room with the MR scanner wearing paramagnetic objects, not only because they could disturb the image that is going to be acquired [81] , but also because under the influence of a very intense magnetic field, they could behave as projectiles. Different standards have been established (as the ones in the paragraph above [78], [79], [80]) to decide whether a certain implanted device can be compatible with MR scanners or not, depending on the force, torque, heating and vibration this device experiences. [82]

---

[2] Legislation annex: Declaration of Helsinki, 52nd WMA General Assembly, Edinburgh, Scotland, October 2000

[3] Legislation annex: Ley 14/2007, de 3 de julio, de Investigación biomédica. (BOE núm 151, de 4 de julio de 2007)

- There is a line around the MR scanner indicating where the magnetic field starts to be higher than 5 Gauss (G) (1G=0.1 mT) [83] . Nothing that could be attracted by the magnet must trespass that line.
- Magnetic field shielding is compulsory, not only because the image could be affected by elements from the outside the room, but also to reduce the probability of accidents due to the facts exposed above, decreasing as much as possible the field outside the magnet.
- The RF energy absorbed by the patient, what is known as Specific Absorption Rate or SAR, has a maximum legal limit of 2 W/kg, so there are constraints in those sequences making use of many RF pulses [82] .
- The intensity of the gradients has also to be bounded, as if very intense magnetic fields coming from the gradient coils are activated and deactivated, by the Faraday-Lenz's law [12] some currents opposing to these changes called eddy currents [84] could be induced in the muscles or nerves of the patient, causing involuntary contractions. This could also cause a malfunction of implanted electrical devices. The maximum legal limit of gradient intensity is of 30 T/m.

Apart from security issues, there are also standards to set how MRI acquisition has to be performed, as NEMA MS (National Electrical Manufacturers Association). For more information, go to [85] .

Once the MR scan has been performed and all the data have been acquired, very restrictive laws are applied on the use of these data, as it was previously explained. The main law regulating this on Spain is the LOPD (*Ley Oficial de Protección de Datos*)[4], the Official Law on Data Protection, together with article 43 of the Spanish Constitution[5]. In research, the following points have always to be fulfilled:

- Every volunteer must be informed of his or her data and how these data are going to be treated. Nobody with different means from the ones for which the data have to be used can have access to these data.
- Volunteer's data will be confidential unless his or her life is placed at risk, so in that case, the data will be communicated to close relatives.
- Volunteer's data will only be used for the research conducted. They must not be used with other means.
- Data can be shared without the volunteer's consent only for the research or public interest purposes.
- Results arising from a study in which the data of a volunteer have been used can only be published if the volunteers agrees to.

---

[4] Legislation annex: Protección de datos de Carácter Personal, BOE, last updated on 24th May 2018

[5] Legislation annex: Spanish Constitution, article 43. (BOE núm.311, de 29 de diciembre de 1978)

9. GLOSSARY

ACR: American College of Radiology

AP: Anterior Posterior

ASTM: American Society for Testing of Materials

BOE: Boletín Oficial del Estado

CNIC: *Centro Nacional de Investigaciones Cardiovasculares*

CNR: Contrast-to-Noise Ratio

CT: Computer Tomography

CTA: Computer Tomography Angiography

CV: Coefficient of Variation

EM: ElectroMagnetic

FA: Flip Angle

FE: Frequency Encoding

FFT: Fast Fourier Transform

FH: Foot Head

FID: Free Induction Decay

FOV: Field Of View

FSE: Fast Spin Echo

FT: Fourier Transform

GGL: Generalized Gauss-Laplace

GRE: Gradient Echo

HGUGM: *Hospital General Universitario Gregorio Marañón*

IFT: Inverse Fourier Transform

IFFT: Inverse Fast Fourier Transform

IR: Inversion Recovery

ISO: International Standard Organization

LR: Left Right

MIT: Massachusetts Institute of Technology

MR: Magnetic Resonance

MRA: Magnetic Resonance Angiography

MRI: Magnetic Resonance Imaging

MSU: Michigan State University

NEMA: National Electrical Manufacturers Association

PDF: Probability Distribution Function

PD-w: Proton Density-weighted

PE: Phase Encoding

QBC: Quadrature Body Coil, Quad-body coil or Q-body coil

RAM: Random Access Memory

RF: Radio Frequency

ROI: Region Of Interest

SAR: Specific Absorption Rate

SE: Spin Echo

SENSE: SENSitivity Encoding

SNR: Signal-to-Noise Ratio

SPAIR: Spectral Attenuated Inversion Recovery

SSFP: Steady State Free Precession

SV: Singular Value

SVD: Singular Value Decomposition

SW: Susceptibility Weighted

TFE: Turbo Field Echo

TOF: Time-Of-Flight

TV: Total Variation

T_1-w: T_1-weighted

T_2^*: T_2 star

T_2-w: T_2-weighted

UCL: University College of London

UC3M: *Universidad Carlos III de Madrid*

WMA: World Medical Association

WT: Wavelet Transform

10. REFERENCES

[1] W. Reusch, “Magnetic Resonance Spectroscopy,” *MSU Chemistry*, 2013. [Online]. Available: https://www2.chemistry.msu.edu/faculty/reusch/virttxtjml/spectrpy/nmr/nmr1.htm.

[2] M. J. Sands and A. Levitin, “Basics of magnetic resonance imaging,” *Semin. Vasc. Surg.*, vol. 17, no. 2, pp. 66–82, 2004.

[3] D. Lee, H. Koo, I. Sun, J. Ryu, … K. K.-C. S., and undefined 2012, “Multifunctional nanoparticles for multimodal imaging and theragnosis,” *pubs.rsc.org*.

[4] R. Nave, “Nuclear Spin,” *HyperPhysics Concepts*, 2000. [Online]. Available: http://hyperphysics.phy-astr.gsu.edu/hbase/Nuclear/nspin.html.

[5] “Gyroscope Physics,” *The Physics of Rotation*, 2017. [Online]. Available: http://www.cleonis.nl/physics/phys256/gyroscope_physics.php.

[6] S. M. I. Group, “Isochromat,” *Magnetic Resonance-Technology Information Portal (MR-TIP)*, 2003. [Online]. Available: http://www.mr-tip.com/serv1.php?type=db1&dbs=Isochromat.

[7] H. . Schild, *MRI made easy*, First. Berlin: Schering, 1990.

[8] A. D. Elster, “Gyromagnetic Ratio,” *Questions & Anwers in MRI*, 2017. [Online]. Available: http://mriquestions.com/gyromagnetic-ratio-gamma.html.

[9] A. D. Elster, “Larmor Frequency,” *Questions & Anwers in MRI*, 2017. [Online]. Available: http://mriquestions.com/who-was-larmor.html.

[10] A. D. Elster, “Zeeman Splitting,” *Questions & Anwers in MRI*, 2017. [Online]. Available: http://mriquestions.com/energy-splitting.html.

[11] A. D. Elster, “Net Magnetization,” *Questions & Anwers in MRI*, 2017. [Online]. Available: http://mriquestions.com/net-magnetization-m.html.

[12] R. Nave, “Faraday’s Law and Lenz’s Law,” *HyperPhysics Concepts*, 2000. [Online]. Available: http://hyperphysics.phy-astr.gsu.edu/hbase/electric/farlaw.html.

[13] A. D. Elster, “Coil Overview,” *Questions & Anwers in MRI*, 2017. [Online]. Available: http://mriquestions.com/many-kinds-of-coils.html.

[14] U. C. of London, “Spin-lattice and Spin-spin Relaxation,” *NMR Spectroscopy*. [Online]. Available: https://www.ucl.ac.uk/nmr/NMR_lecture_notes/L5_3SH_web_shortened.pdf.

[15] R. Reddy, “Bloch figurefigs,” 2018. [Online]. Available: https://pdfs.semanticscholar.org/presentation/b816/f4d4233d94ba3bdb4067af4e223a4f279566.pdf.

[16] L. Antonio and M. Martín, “Desarrollo de una herramienta gráfica de análisis cuantitativo y semicuantitativo de imágenes por resonancia magnética con realce por contraste dinámico de,” Universidad Central, 2017.

[17] M. Tan, Z. L.- Theranostics, and U. 2011, “Integrin targeted MR imaging,” *Theranostics*, vol. 1, pp. 83–101, 2011.

[18] “Free Induction Decay,” *Wikiwand*. [Online]. Available: http://www.wikiwand.com/en/Free_induction_decay.

[19] A. D. Elster, “Free Induction Decay,” *Questions & Anwers in MRI*, 2017. [Online]. Available: http://mriquestions.com/free-induction-decay.html.

[20] A. D. Elster, “T2 vs T2*,” *Questions & Anwers in MRI*, 2017. [Online]. Available: http://mriquestions.com/t2-vs-t2.html.

[21] Masoud and F. Gaillard, “MRI Sequences (overview),” *Radiopaedia*, 2005. [Online]. Available: https://radiopaedia.org/articles/mri-sequences-overview.

[22] A. D. Elster, “Spin Echo (SE),” *Questions & Anwers in MRI*, 2017. [Online]. Available: http://mriquestions.com/spin-echo1.html.

[23] A. D. Elster, “Gradient Echo (GRE),” *Questions & Anwers in MRI*, 2017. [Online]. Available: http://mriquestions.com/gradient-echo.html.

[24] A. D. Elster, “Gradient Coils,” *Questions & Anwers in MRI*, 2017. [Online]. Available: http://mriquestions.com/gradient-coils.html.

[25] A. D. Elster, “Steady-State Free Precession,” *Questions & Anwers in MRI*. [Online]. Available: http://mriquestions.com/what-is-ssfp.html.

[26] A. D. Elster, “MRA Methods,” *Questions & Anwers in MRI*, 2017. [Online]. Available: http://mriquestions.com/mra-methods.html.

[27] A. D. Elster, “Fat Supression Methods,” *Questions & Anwers in MRI*, 2017. [Online]. Available: http://mriquestions.com/best-method.html.

[28] A. D. Elster, “IR: Introduction,” *Questions & Anwers in MRI*, 2017. [Online]. Available: http://mriquestions.com/what-is-ir.html.

[29] M. Hammer, “MRI Physics: Spatial Localization,” *X-RayPhysics-Interactive Radiology Physics*, 2013. [Online]. Available: http://xrayphysics.com/spatial.html.

[30] A. D. Elster, “Spatial Encoding,” *Questions & Anwers in MRI*, 2017. [Online]. Available: http://mriquestions.com/how-to-locate-signals.html.

[31] S. M. I. Group, “Contrast-to-Noise Ratio,” *Magnetic Resonance-Technology Information Portal (MR-TIP)*, 2003. [Online]. Available: http://www.mr-tip.com/serv1.php?type=db1&dbs=Contrast+to+Noise+Ratio.

[32] A. D. Elster, “Contrast-enhanced MRA,” *Questions & Anwers in MRI*, 2017. [Online]. Available: http://mriquestions.com/contrast-enhanced-mra.html.

[33] A. D. Elster, “Fast Spin-Echo.” [Online]. Available: http://mriquestions.com/what-is-fsetse.html.

[34] E. Haacke, S. Mittal, … Z. W.-A. J. of, and U. 2009, “Susceptibility-weighted imaging: technical aspects and clinical applications, part 1,” *Am Soc Neuroradiol.*, vol. 30, no. 1, pp. 19–30, 2009.

[35] U. Bashir, “Time of Flight Angiography,” *Radiopaedia*, 2005. .

[36] J. Keshavamurthy and J. R. Ballinger, “Phase Contrast Imaging,” *Radiopaedia*, 2005. [Online]. Available: https://radiopaedia.org/articles/phase-contrast-imaging.

[37] P. T. Norton, N. C. Nacey, D. B. Caoban, S. B. Gay, and C. M. Kramer, “Steady State Free Precession,” *Cardiac MRI*. [Online]. Available: https://www.med-ed.virginia.edu/courses/rad/cardiacmr/Techniques/SSFP.html.

[38] K. Pruessmann and … M. W., “SENSE: sensitivity encoding for fast MRI,” *Int. Soc. Magn. Reson. Med.*, vol. 42, no. 5, pp. 952–962, 1999.

[39] A. D. Elster, “Parallel Imaging,” *Questions & Anwers in MRI*, 2017. [Online]. Available: http://mriquestions.com/what-is-pi.html.

[40] A. D. Elster, “Aliasing,” *Questions & Anwers in MRI*, 2017. [Online]. Available: http://mriquestions.com/aliasing.html.

[41] P. Sprawls, “Image Noise,” in *Physical Principles of Medical Imaging*, Second., Madison, 1995.

[42] A. D. Elster, “SENSE/ASSET,” *Questions & Anwers in MRI*, 2017. [Online]. Available: http://mriquestions.com/senseasset.html.

[43] D. J. Bell and J. Yeung, “Signal-to-Noise Ratio,” *Radiopaedia*, 2005. [Online]. Available: https://radiopaedia.org/articles/signal-to-noise-ratio-1.

[44] M. Fuderer, … J. van den B.-I. S. of, and U. 2004, “SENSE reconstruction using feed forward regularization,” *Int. Soc. Magn. Reson. Med.*, vol. 11, p. 2130, 2004.

[45] M. I. of T. (MIT), “Singular Value Decomposition (SVD) Tutorial,” *MIT Website*. [Online]. Available: http://web.mit.edu/be.400/www/SVD/Singular_Value_Decomposition.htm.

[46] A. N. Langville, “Truncated SVD and its Applications,” *National Science Foundation Website*. [Online]. Available: http://langvillea.people.cofc.edu/DISSECTION-LAB/Emmie%27sLSI-SVDModule/p5module.html.

[47] H. Umar, “Regularization.” [Online]. Available: http://homepages.inf.ed.ac.uk/rbf/CVonline/LOCAL_COPIES/AV0405/UMAR/AVassign2.pdf.

[48] Stephanie, “Tikhonov Regularization: Simple Definition,” *Statistics How To*, 2017. [Online]. Available: http://www.statisticshowto.com/tikhonov-regularization/.

[49] H. Omer, M. Qureshi, and R. J. Dickinson, “Regularization-based SENSE reconstruction and choice of regularization parameter,” *Concepts Magn. Reson. Part A*, vol. 44, no. 2, pp. 67–73, 2015.

[50] J. Tsao, K. Pruessmann, and P. Boesiger, “Feedback regularization for SENSE reconstruction,” *Proc. 10th Annu. Meet. ISMRM*, vol. 10, p. 2002, 2002.

[51] R. Fisher, S. Perkins, A. Walker, and E. Wolfart, “Median Filter,” *HI Works*, 2003. [Online]. Available: https://homepages.inf.ed.ac.uk/rbf/HIPR2/median.htm.

[52] F.-H. Lin, K. K. Kwong, J. W. Belliveau, and L. L. Wald, “Parallel imaging reconstruction using automatic regularization,” *Magn. Reson. Med.*, vol. 51, no. 3, pp. 559–567, Mar. 2004.

[53] B. Liu, L. Ying, M. Steckner, … J. X.-… I. F. N. to, and U. 2007, “Regularized SENSE reconstruction using iteratively refined total variation method,” in *4th IEEE International Symposium on Biomedical Imaging: From Nano to Macro*, 2007.

[54] T. Rowland, “Total Variation,” *Wolfram MathWorld*, 2018. [Online]. Available: http://mathworld.wolfram.com/TotalVariation.html.

[55] B. Liu, K. King, M. Steckner, J. Xie, J. Sheng, and L. Ying, “Regularized sensitivity encoding (SENSE) reconstruction using bregman iterations,” *Magn. Reson. Med.*, vol. 61, no. 1, pp. 145–152, Jan. 2009.

[56] A. N. Iusem, “Bregman Distance,” *Encyclopedia of Mathematics*, 2011. [Online]. Available: https://www.encyclopediaofmath.org/index.php/Bregman_distance.

[57] L. Chaâri and … J. P., “A wavelet-based regularized reconstruction algorithm for SENSE parallel MRI with applications to neuroimaging,” *Med. Image Anal.*, 2011.

[58] D. Nečas and P. Klapetek, “Wavelet Transform,” in *Gwyddion*, 2018.

[59] E. W. Weisstein, “Probability Density Function,” *Wolfram MathWorld*, 2018. [Online]. Available: http://mathworld.wolfram.com/ProbabilityDensityFunction.html.

[60] T. Kozubowski and K. Podgórski, “Multivariate generalized Laplace distribution and related random fields,” *J. Multivar. Anal.*, vol. 113, pp. 59–72, 2013.

[61] R. Fisher, S. Perkins, A. Walker, and E. Wolfart, “Mean Filter,” *HI Works*, 2003. [Online]. Available: https://homepages.inf.ed.ac.uk/rbf/HIPR2/mean.htm.

[62] S. M. I. Group, “3D-TFE,” *Magnetic Resonance-Technology Information Portal (MR-TIP)*, 2003. [Online]. Available: http://www.mr-tip.com/serv1.php?type=db1&dbs=3D TFE.

[63] A. D. Elster, “Spectral Attenuated Inversion Recovery (SPAIR),” *Questions & Anwers in MRI*, 2017. [Online]. Available: http://mriquestions.com/spair-v-spir.html.

[64] A. D. Elster, “Navigator Echoes?,” *Questions & Anwers in MRI*, 2017. [Online]. Available: http://mriquestions.com/navigator-echoes.html.

[65] R. Fisher, S. Perkins, A. Walker, and E. Wolfart., “Gaussian Smoothing,” *HI Works*, 2003. [Online]. Available: https://homepages.inf.ed.ac.uk/rbf/HIPR2/gsmooth.htm.

[66] L. HuiMing, “Deep learning for image denoising,” *Int. J. Signal Process.*, vol. 7, no. 3, pp. 171–180, 2014.

[67] A. A. Sarnsono, R. T. Whitakerzs, and R. Chris, “Noise-Adaptive Nonlinear Filtering Technique for SENSE - Reconstructed Images,” vol. 962, no. 1999, p. 68566, 2002.

[68] M. Lustig, D. Donoho, and J. M. Pauly, “Sparse MRI: The application of compressed sensing for rapid MR imaging,” *Magn. Reson. Med.*, vol. 58, no. 6, pp. 1182–1195, Dec. 2007.

[69] A. C. of R. (ACR), “CT Angiography (CTA),” *RadiologyInfo.org for patients*, 2017. [Online]. Available: https://www.radiologyinfo.org/en/info.cfm?pg=angioct.

[70] A. C. of R. (ACR), “Contrast Materials,” *RadiologyInfo.org for patients*, 2017. [Online]. Available: https://www.radiologyinfo.org/en/info.cfm?pg=safety-contrast.

[71] A. H. A. (AHA), “Cardiac Catheterization,” *American Heart Association Website*. [Online]. Available: http://www.heart.org/HEARTORG/Conditions/HeartAttack/DiagnosingaHeartAttack/Cardiac-Catheterization_UCM_451486_Article.jsp#.WxVSWO6FOUk.

[72] A. Villarreal, “Esto es lo que cuestan las revistas científicas: España se ha pulido 213 millones desde 2012,” *El Confidencial*, 2018. [Online]. Available: https://www.elconfidencial.com/tecnologia/ciencia/2018-02-16/revistas-cientificas-suscripciones-millonada_1522586/.

[73] “Estudiar en Madrid,” *Espacio Madrileño de Enseñanza Superior*, 2018. [Online]. Available: http://www.emes.es/Sistemauniversitario/tabid/212/Default.aspx.

[74] C. Point, “Resonancia Magnética,” *Clinic Point Website*, 2018. [Online]. Available: https://www.clinicpoint.com/madrid/radiologia/resonancia-magnetica.

[75] C. F. Esteban, “6 formas con las que ganar dinero con tu cuerpo gracias a la ciencia,” *Business Insider España*, 2018. [Online]. Available: https://www.businessinsider.es/6-formas-que-ganar-dinero-tu-cuerpo-gracias-ciencia-199952.

[76] C. Commons, “Sobre las licencias,” *Creative Commons website*, 2017. [Online]. Available: https://creativecommons.org/licenses/.

[77] J. G. Delfino and T. O. Woods, “New Developments in Standards for MRI Safety Testing of Medical Devices,” *Curr. Radiol. Rep.*, vol. 4, no. 6, p. 28, Jun. 2016.

[78] A. International, *Standard Test Method for Measurement of Magnetically Induced Displacement Force on Medical Devices in the Magnetic Resonance Environment*. USA, 2015.

[79] A. International, *Standard Test Method for Measurement of Magnetically Induced Torque on Medical Devices in the Magnetic Resonance Environment*. USA, 2017.

[80] I. S. O. (ISO), *Assessment of the safety of magnetic resonance imaging for patients with an active implantable medical device*. 2018.

[81] A. D. Elster, “Susceptibility Artifacts,” *Questions & Anwers in MRI*, 2017. [Online]. Available: http://mriquestions.com/susceptibility-artifact.html.

[82] G. Schaefers and A. Melzer, “Testing methods for MR safety and compatibility of medical devices,” *Minim. Invasive Ther. Allied Technol.*, vol. 15, no. 2, pp.

71–75, Jan. 2006.

[83] “Gauss, Unit of Measurement,” *Encyclopaedia Britannica*. 1998.

[84] J. Henry, “Eddy Current,” *Princeton University Website*. [Online]. Available: https://www.princeton.edu/ssp/joseph-henry-project/eddy-currents/eddy_wiki.pdf.

[85] N. E. M. A. (NEMA), *Magnetic Resonance*. 2016.